

MASTER

On Modeling and Identification of Bellows Suction Cup Dynamics for Robotic Tossing

Peeters, G.J.H.

Award date:
2021

[Link to publication](#)

Disclaimer

This document contains a student thesis (bachelor's or master's), as authored by a student at Eindhoven University of Technology. Student theses are made available in the TU/e repository upon obtaining the required degree. The grade received is not published on the document as presented in the repository. The required complexity or quality of research of student theses may vary by program, and the required minimum study period may vary in duration.

General rights

Copyright and moral rights for the publications made accessible in the public portal are retained by the authors and/or other copyright owners and it is a condition of accessing publications that users recognise and abide by the legal requirements associated with these rights.

- Users may download and print one copy of any publication from the public portal for the purpose of private study or research.
- You may not further distribute the material or use it for any profit-making activity or commercial gain



Department of Mechanical Engineering
Dynamics & Control Section

On Modeling and Identification of Bellows Suction Cup Dynamics for Robotic Tossing

MSc. graduation project
DC 2021.078

G.J.H. Peeters BSc.
0952732

Project Coaching:

dr. ir. Alessandro Saccon
ir. Maarten Jogeneel

Project Supervisor:

prof. dr. ir. Nathan van de Wouw

Project Support:

ir. Stijn de Looijer
ir. Sjouke de Zwart

Vanderlande
Smart Robotics

Eindhoven, September 7, 2021

Abstract

The rapid growth of the e-commerce market causes increasing demands on automated pick and place technology. A possible solution to meet these demands is through the introduction of robotic tossing of packages onto conveyor belts. Besides the increase in handling speed, the tossing of packages gives the additional benefit that packages can be tossed outside the reach of the robot arm.

A widely used gripper, for the robotic picking and placing of packages, is the bellows suction cup. Due to its compliance, the bellows suction cup enables the robot arm to pick up a large variety of packages. When making a tossing motion with the robot arm, the bellows suction cup will deform due to this compliance. To predict the deformation of the bellows suction cup, the currently unknown bellows suction cup dynamics need to be identified and modeled. Being able to predict the bellows suction cup dynamics, when holding a package, is the first step to predicting the release pose of the package and thus also the first step to predicting the final rest-pose of the package on the conveyor.

In this report, the compressed bellows suction cup (when holding a package, the bellows suction cup is compressed) is considered as a massless elastic element. Hereto, the stiffness is modeled as a 6-dimensional spring. Based on literature, a spring potential energy function is built, from which a spring wrench is derived. To capture the damping of the bellows suction cup, also a 6-dimensional damper is modeled. Using OptiTrack motion capture measurement data, the stiffness and damping parameters are identified experimentally. For this parameter identification, i.e., the estimation of the stiffness and damping matrices, we used inverse dynamics in combination with a weighted linear least-squares approach. Using the estimated stiffness and damping matrices, the forward dynamics are simulated for a known tool-arm trajectory. To validate the outcome, the simulation results are compared to the actual measured pose data.

To identify the stiffness and damping by using inverse dynamics, there is a clear need to estimate the linear and angular velocity and acceleration from the measured pose data. Since that the usage of finite different methods leads to inaccurate estimates of the linear and angular velocity and acceleration, due to the measurement noise, a new method is proposed to estimate the linear and angular velocity and acceleration in 3-dimensional space. This new method is the usage of a Savitzky-Golay filter, which is a moving averaging window, on $SO(3) \times \mathbb{R}^3$ data.

The validation shows some first promising results. However, the mismatch between simulation outcome and measurement data is still too large and shows that there is still a lot of space for improvement. For the continuation of research, several recommendations are presented on the improvement of the modeling as well as the identification aspects of the current research. Herein, the most important recommendation would be changing the identification procedure to an approach in which a prediction-error method is used.

Acknowledgments

First of all, I would like to thank Alessandro Saccon for coaching me during this project. Besides extending my knowledge about multi-body dynamics and introducing me to Lie group theory, something which I never heard of before, I think the most valuable lesson learned from Alessandro is how to handle a large and challenging project such as this MSc. graduation project. I did not have experience with doing such large projects and was sometimes a bit overwhelmed by it. At these moments it was nice that Alessandro freed up some time and took me by the hand by helping me to come up with an approach on how to handle the problems. Alessandro did this coaching together with Maarten Jongeneel, who definitely also deserves a big thank you. Altogether, I learned a lot from Maarten and Alessandro and will look back on a pleasant collaboration.

Next, I would like to thank Nathan van de Wouw for supervising my graduation project, for providing helpful feedback and discussions during the progress meetings, and for reviewing my thesis.

Furthermore, I would like to thank Luuk Poort, Jari van Steen, Sjouke de Zwart (Smart Robotics), and Stijn de Looijer (Vanderlande) for joining the monthly progress meetings; where they helped me by shining their light on this project or by providing me the information I needed. A special thanks to Stijn, who made it often possible for me to work with the measurement setup in the Vanderlande Innovation Lab. In times where working from home was the motto, I really enjoyed the days working in the lab.

Furthermore, I want to thank my friends. Although they did not contribute to this report, it was really nice to meet them during the weekends and do some sports or have a drink together, something which lifted my spirits. Especially during the weekends in the lockdowns where having a good laugh did break the rut of the week.

Finally and above all, I want to thank my parents for always believing in me and providing me the support I needed.

Giel Peeters
Slek-Echt, August 2021

Nomenclature

Acronyms

PA	Package
RA	Robot arm
SC	Suction Cup
TA	Tooling arm

Groups, algebras, and sets

e	Identity element of a Lie group
g_1	Element of Lie group \mathcal{G}
\mathfrak{g}	Point on tangent space of a Lie group
\mathcal{G}	General Lie group
h_1	Element of Lie group \mathcal{H}
\mathcal{H}	General Lie group
\mathbb{R}	Set of real numbers
$\mathfrak{se}(3)$	The Lie algebra of SE(3)
SE(3)	The Special Euclidean group in 3 dimensions
$\mathfrak{so}(3)$	The Lie algebra of SO(3)
SO(3)	The Special Orthogonal group in 3 dimensions
$T_{g_1}\mathcal{G}$	Tangent space of a Lie group \mathcal{G} considered at $g_1 \in \mathcal{G}$
\circ	Lie group operator on \mathcal{G}
\bullet	Lie group operator on \mathcal{H}

Greek symbols

β	Set of estimated forces and torques
${}^A\delta\mathbf{H}_B$	The infinitesimal perturbation of the pose
${}^B\Delta_{A,B}$	The trivialized infinitesimal perturbation, a twist
$\boldsymbol{\eta}$	Column of parameters to describe polynomial $\boldsymbol{\xi}$
θ	Angle of rotation in rad
μ	The average estimated force and torque in every direction
$\boldsymbol{\xi}$	A polynomial
${}^B\boldsymbol{\tau}_{SC \rightarrow Pa}$	The torque in Nm from the suction cup to the parcel at frame B
$\boldsymbol{\omega}$	Angular velocity in rad/s

Roman symbols

A	World coordinate frame
\mathbf{A}	Matrix containing coefficients of linear system
$[A]$	Orientation frame associated to A
$A[B]$	Frame with origin o_A and orientation of A
\mathbf{b}	Column vector with forces and torques

B	Body-fixed frame located at center of mass of the package
\mathbf{D}	6×6 damping matrix
\mathbf{e}	Error
E	Frame associated to the tip of the tooling arm as defined in this report
E_M	Frame associated to the tip of the tooling arm as defined in Motive
E_g	Gravitational energy of the package
E_{kin}	Kinetic energy of the package
${}^B\mathbf{f}_{SC \rightarrow Pa}$	The wrench acting from the suction cup on the parcel at frame B
${}^B\mathbf{f}_{SC \rightarrow Pa}$	The force acting from the suction cup on the parcel at frame B in N
\mathbf{f}_g	Gravity acting on the package in N
F	Frame fixed to center of mass of object (plastic plate or cylindrical weight)
g	Gravitational acceleration of 9.81 m/s
${}^A\mathbf{H}_B$	Homogeneous transformation from B to A
\mathbf{I}_3	3×3 identity matrix
${}^B\mathbb{I}_B$	3×3 inertia tensor w.r.t. frame B
\mathbf{K}	6×6 stiffness matrix
l_0	Nominal length of bellows suction cup during holding phase in m
l_1	Link length between frames S_1 and S in m
l_2	Link length between frames S_2 and E in m
L_1	Part of the bellows suction cup between S_1 and S
L_2	Part of the bellows suction cup between E and S_2
m	Mass of the package in kg
M	Motive calibration frame
${}^B\mathbb{M}_B$	Inertia tensor with respect to frame B
n	Order of polynomial used for Savitzky-Golay filtering
n_w	Number of data points on each side of the center point of the window
N	Number of discrete time data points
\mathbf{o}_B	Origin of frame B
${}^A\mathbf{o}_B$	Position of frame B w.r.t. A in m
\mathbf{p}	An arbitrary point
\mathbf{P}	Parametrization of the damping matrix
P_0	Potential energy of the spring
P_g	Gravitational potential energy
\mathbf{Q}	Covariance matrix
${}^A\mathbf{R}_B$	Rotation matrix from B to A
S	Frame fixed to the center of the suction cup lip as defined in this report
S_M	Frame fixed to the center of the suction cup lip as defined in Motive
S_1	Lower frame placed at the center of stiffness
S_2	Upper frame placed at the center of stiffness
t	Time in s
t_k	Time in s at index k
\mathbf{v}	Linear velocity
${}^A\mathbf{v}_{A,B}$	Right trivialized velocity of B w.r.t. A written in A
${}^B\mathbf{v}_{A,B}$	Left trivialized velocity of B w.r.t. A written in B
w	Window defined for the Savitzky-Golay filtering
\mathbf{W}	Weighting matrix for weighted least-squares method
\mathbf{x}	Column vector of unknown stiffness and damping matrix entries
${}^B\mathbf{X}^A$	Coordinate transformation from A to B
${}^A\mathbf{X}_B$	Linear transformation from B to A
\mathbf{Z}	$6N \times 6N$ matrix with weighting matrix \mathbf{W} blocks on the diagonal

Subscripts, superscripts, and operations

$(\cdot)^\vee$	'Vee' operator: matrix to vector representation of algebra element
$(\cdot)^\wedge$	'Hat' operator: vector to matrix representation of algebra element
$\ (\cdot)\ $	The Euclidean norm of a vector
$(\cdot)^{-1}$	The inverse of a square matrix
$(\cdot)^T$	The transpose of a matrix
$\widehat{(\cdot)}$	Estimated by using a Savitsky-Golay filter
$\dot{(\cdot)}$	Estimated via finite difference
$\ddot{(\cdot)}$	First time derivative
$\overset{\cdot}{(\cdot)}$	Second time derivative
$(\cdot)_{SC \rightarrow PA}$	Working from SC on PA
$(\cdot)_\times$	Cross product on \mathbb{R}^3
$(\cdot)_{\times^*}$	6×6 matrix representation of the dual cross product
$(\cdot)_z$	Indicating the z component
$d \exp$	The right trivialized tangent of the exponential mapping
$\mathfrak{d}^{2(+)} \exp$	The right trivialized geometric Hessian of the exponential mapping with respect to the (+) Cartan-Schouten connection
\exp	The matrix exponential
\log	The matrix logarithm
tr	The trace of a square matrix, sum of its diagonal elements
var	The variance

Contents

1	Introduction	1
1.1	Context and motivation	1
1.2	Literature review	4
1.2.1	Automation and robotic tossing	4
1.2.2	Bellows suction cup dynamics	5
1.3	Problem definition and research goal	6
1.4	Structure of the report	7
2	Mathematical Preliminaries	9
2.1	Lie groups theory	9
2.1.1	Preliminaries on Lie groups	9
2.1.2	The Special Orthogonal group $SO(3)$	10
2.1.3	The Special Euclidean group $SE(3)$	11
2.2	Multibody notation for rigid body dynamics	12
2.2.1	Notation of coordinate frames and points	12
2.2.2	Notation of rotational velocity	12
2.2.3	Notation of rigid body velocity	13
2.2.4	Wrench notation	14
2.2.5	Notation of derivatives	14
3	Modeling the Bellows Suction Cup Dynamics	17
3.1	Frame definitions and equations of motion	17
3.2	Nominal configuration bellows suction cup	20
3.3	Modeling of stiffness	22
3.3.1	Frames for relative displacement	22
3.3.2	Derivation spring wrench	23
3.3.3	Wrenches resulting from small displacements	25
3.4	Modeling of damping	25
3.5	Numerical implementation and validation	26
4	Experimental data collection and parameter identification	31
4.1	Measurement procedure and data pre-processing	31
4.1.1	Measurement procedure	32
4.1.2	Rotational and lateral offset compensation	34
4.2	Nominal bellows suction cup length identification	38
4.3	Stiffness and damping identification	40
4.3.1	Estimation of linear and angular velocity and acceleration from $SO(3) \times \mathbb{R}^3$ data	41
4.3.2	Estimating of stiffness and damping matrices	50

5	Conclusion and Recommendations	57
5.1	Conclusion	57
5.2	Recommendations	57
	Appendices	65
A	Generalized inertia tensor	65
B	Approximations	66
C	Derivation of the spring wrench acting on frame S	67
D	Coupled translational-angular damping on $SE(3)$	69
	D.1 Passivity of the damping wrench	70
E	Velocity transformation	70
F	Central difference method	71
G	Definition exponential mapping on $SO(3)$ and its derivatives	72
H	Exclusion of outliers in motion capture data	73
I	Weighting matrices for least-squares parameter identification	75
J	Rewriting package body-fixed velocity and acceleration	76

Chapter 1

Introduction

1.1 Context and motivation

Over the years, e-commerce and global parcel traffic have shown significant growth [1, 2]. With the expectations that these will keep increasing, the demand for logistic labor continues growing [3]. However, a shortage in the working population prevents uniform expansion [4]. To keep up with the increasing logistic demand, there is a clear need to increase the workforce productivity, i.e., the number of processed items per labor hour needs to increase. A solution to the shortage of labor would be the usage of automation systems. Examples of automation systems that already have been implemented in logistic warehouses to increase the workforce productivity are transport systems, picking systems, and sorting systems. However, the problem is that these automation systems often cannot handle a wide variety of packages or are either too slow, have a too large footprint, and/or are too expensive.

The overall goal of the current research, as a part of the I.A.M. project [5], is increasing the working speed of picking systems. These picking systems are robot arms that pick up packages and place them on running conveyor belts, see Figure 1.1. Up to the present, this placing is carried out by moving the robot arm along the running conveyor to reach a similar speed before placing the package on the belt. To increase the working speed, a solution could be to start tossing the packages instead of placing them. According to Saccon [6], the expectation for this more dynam-

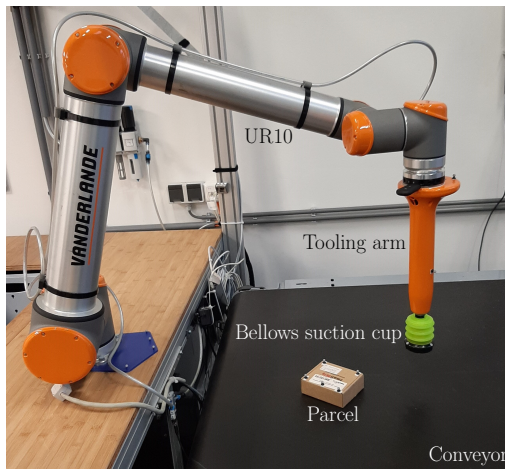


Figure 1.1: A picture showing the UR10 robot arm, the tooling arm, the conveyor, a parcel, and the bellows suction cup, which is also called the gripper.

ical way of handling packages is a 10% increase in working speed of the robot arm. This increase in working speed leads to higher workforce productivity, i.e., more processed packages per labor hour, and thus a higher capacity. This higher capacity could result in lower costs per package. Besides these benefits, the tossing of packages gives the option to toss the packages outside the robot arm its reachable area. For example, this could be an advantage when sorting packages and putting them in different bins. More bins could be reached and with that fewer robots would be needed. One of the goals of the I.A.M. project is to predict the end-state, position and orientation (in the remainder of this report called the pose), of tossed parcels, with a maximum mass of 4kg. When being able to predict the end-state of a tossed parcels, the control input of the robot arm can be designed such that the desired parcel end-state can be obtained. For this reason, there is a clear need to develop a numerical model which can describe the dynamics of the tossing of parcels.

The robotic tossing of packages can be divided roughly into three main phases, see Figure 1.2. The first phase would be when the package is in contact with the suction cup. When the package loses contact with the suction cup, the second phase starts, which is the free flight of the package. The third and last main phase of robotic tossing starts at the moment the package touches the conveyor belt until it reaches its final end-state and does not move anymore with respect to the running conveyor belt. As part of the I.A.M. project, a study on this last main phase, the impact of boxes on a running conveyor belt, is performed by Poort [7]. When zooming in on the first main phase of the robotic tossing of packages, the time that the package is in contact with the suction cup, this phase can be divided into two sub-phases, namely the *holding phase* and the *release phase*. The *holding phase* is the time that the ejector creates an underpressure within the bellows suction cup, such that the parcel sticks to the bellows suction cup. During the holding phase, the bellows suction cup is compressed due to the partial vacuum created by the ejector, see Figures 1.3a and 1.3b. The second sub-phase, the *release phase*, starts when the signal is given to release the parcel until the contact between the package and suction cup is broken.

This report focuses on the first sub-phase of the contact phase, the holding phase. When a package is held by a bellows suction cup and the robot does move, the bellows suction cup will deform. This deformation of the compressed bellows suction cup depends on several aspects, such as: the package (mass, inertia, and shape), the gripping position of the suction cup on the package, the pressure within the suction cup, the movements of the gripper by the robot arm, and of course the type of suction cup used to hold the packages. To predict the deformation of the compressed bellows suction cup, and with that the state of a package, there is a clear need to identify and model the currently unknown bellows suction cup dynamics. This includes the identifying and modeling of the stiffness and damping of the compressed bellows suction cup.

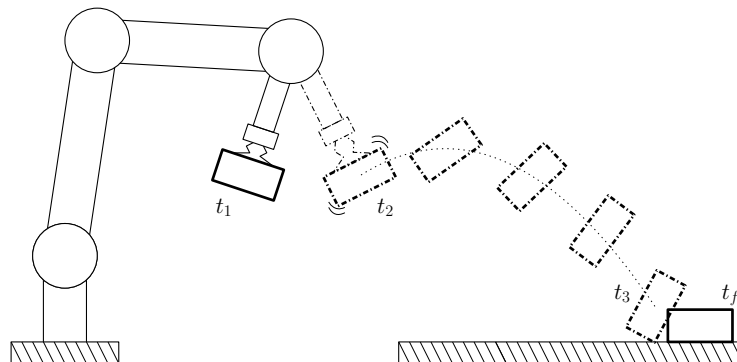


Figure 1.2: Schematic representation of the three phases during the tossing of packages: t_1 , the first phase where the package is in contact with the gripper; t_2 , the second phase when the package is in free flight; t_3 , the third phase where the package hits the conveyor and comes to its final end-state at t_f .

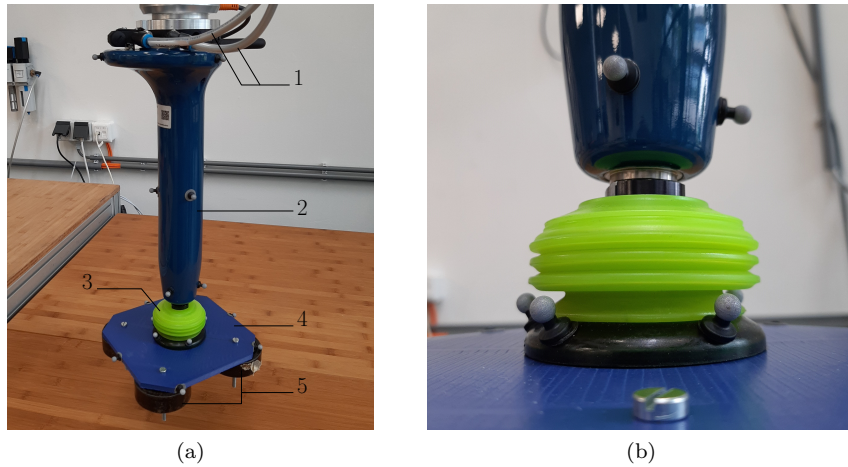


Figure 1.3: Two pictures of the gripper holding a plastic plate. In Figure (a) the following parts are indicated: the input airflow tubes for the ejector (1); the tool-arm (2); the compressed bellows suction cup (3); the plastic plate (4); and the weights, which are rigidly attached to the plastic plate (5). Figure (b) shows a close-up picture of the bellows suction cup being compressed by holding a package.

The bellows suction cup, evaluated in this project, is of type piGRIP S1-7 made by Piab [8], see Figure 1.4. The bellows in combination with the soft foam on the lip make sure that the suction cup can handle the compliance and large dimensional tolerances, which makes it suitable for handling the large versatility in packages [9]. However, due to its bellows, the suction cup is not stiff in all directions and does bend quite easily. Note that the bellows suction cup is axially symmetric, which will be used for modeling the stiffness and damping of the bellows suction cup. Furthermore, a bellows-type suction cup has a lower holding force as well as a bigger chance of residual flow (leakage) compared to a bellowless design. The leakage typically occurs under considerable accelerations of the robot arm, which could lead to unwanted release of the package. This leakage is not considered in this project, since this project focuses on the identification of the bellow suction cup during the holding phase. However, this needs to be a point of attention in further research, especially for the release phase and the robot motion planning for the actual tossing of parcels.

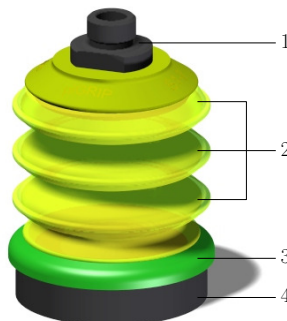


Figure 1.4: A schematic representation of the used bellows suction cup of type piGRIP S1-7 made by Piab [8]. The different parts are: a Male G-thread fitting of size 3/8" (1), three bellows (2), lip of 70 mm in outer diameter (3), and soft foam (4).

1.2 Literature review

In this section, a literature review is presented. First, in Section 1.2.1, some literature about automation and robotic tossing is presented. Thereafter, in Section 1.2.2, the found literature about the modeling of stiffness of elastic elements in 3D space is presented.

1.2.1 Automation and robotic tossing

There has already been done a lot of research in the automation of logistic work [11, 12]. Some of these face the challenge to speed up the package handling of pick-and-place system. An example of this is [13]. This paper presents an approach for optimal smooth trajectory planning of high-speed pick-and-place parallel robots. The goal of the current research, as a part of the I.A.M. project, is to speed up the package handling of a picking robot by tossing the packages on a conveyor belt. The robotic tossing of items is a quite new field of research. However, an example of an already existing tossing robot arm is the TossingBot [10], shown in Figure 1.5a. The TossingBot can throw 600 items of several different shapes per hour, but with only a success rate of 85% that the items end up in the correct bin. Note that the bins are placed outside the robot arm its reachable area. To achieve this, physics-based models are used to plan the release position and velocity, and to calculate the aerial trajectory along the ballistic path, in combination with deep learning for the control of the TossingBot. When comparing the results of the TossingBot with the current research, one should note that the tossing of items in a bin is a simplified problem compared to the tossing of items on a conveyor belt, see Figure 1.1. This is because the impact dynamics are less relevant; namely, for tossing parcels on the conveyor the constraints on the rest-pose are more strict. Once an item is tossed in a bin, it cannot bounce further to the next bin. However, when an item is tossed on a conveyor belt, it can bounce further which results in a different rest place of the tossed item on the conveyor belt.

In this MSc. project, the experiments will be performed using an already existing robot arm system, namely, the Smart Item Robotics system (SIR), shown in Figure 1.5b, which is designed by Smart Robotics [14] in collaboration with Vanderlande [15]. This robot has 6 Degrees Of Freedom (DOF) which provides considerable flexibility allowing the robot to handle a wide variety of items of variable shape and size. Furthermore, the UR10 has a 1300 mm work radius and can carry a payload up to 10kg [16]. Up till now, the SIR system is used for bin-to-bin applications [17] (picking from and placing in stationary bins) and bin-to-belt applications [18] (placing on a running conveyor belt). For both applications applies that the dimensions of the package are taken into account before placing the package in a bin or on a belt. Additionally, intelligent stacking enables the efficient positioning of goods in a bin, while products are handled smoothly

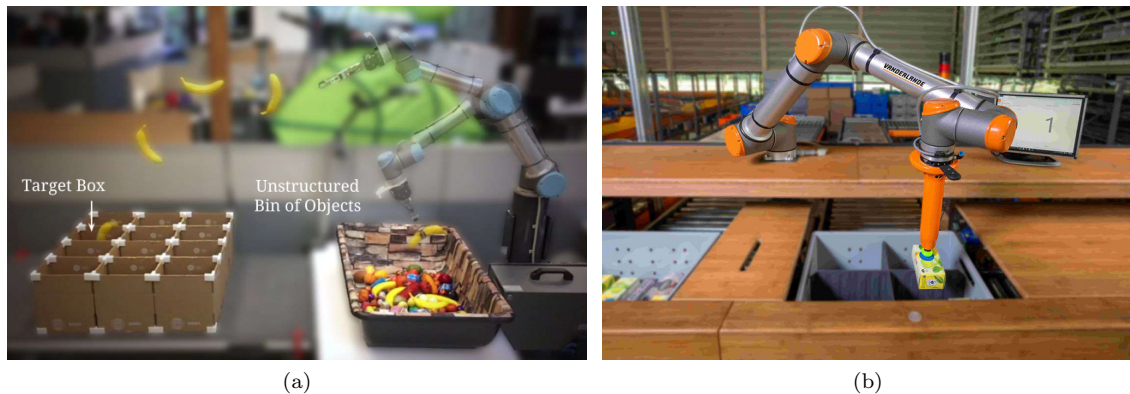


Figure 1.5: In here: (a) shows the TossingBot tossing objects in bins [10] and (b) shows the SIR system executing a bin-to-bin task.

and securely [19]. This intelligent way of stacking items in a bin can be used for picking, with a capacity of up to 600 items per hour [20]. To deal with the many different package types, the SIR system is equipped with a vacuum suction gripper. An ejector generates the partial vacuum in the suction cup using the Venturi effect [21]. The used ejector in the SIR system can make use of blow-off, which shortens the release time.

1.2.2 Bellows suction cup dynamics

Suction cups are widely used in pick-and-place robot systems. An already given example is the SIR system. Another example of the usage of a suction cup is the depalletizing robot of [22]. Furthermore, the usage of a suction cup can also be combined with other gripping tools, such as in [23]. In here, a suction cup is combined with a three-fingered robotic grabbing system. Even though the suction cups are widely used, there is not a lot of specific literature about the identification and modeling of the dynamic behavior of a bellows suction cup. However, the bellows suction cup could be considered as an elastic element, connecting the tooling arm with the package during the holding phase.

About the modeling of stiffness, the following relevant literature is found. Fasse and Breedveld studied the spatial-geometric modeling of elastically coupled rigid bodies. To model the elasticity, a potential energy function should be obtained. From such elastic potential energy function, a spring wrench can be obtained. In [24], Fasse and Breedveld state some criteria which an elastic potential energy function should satisfy. The criteria are: (1) The potential energy functions should be *sufficiently diverse*. Given any local stiffness behavior, there must exist parameters that exactly model this local behavior. (2) The potential energy functions should be *parsimonious*. There should not be more parameters than necessary to model arbitrary local behavior. Together, sufficient diversity and parsimony imply that the parameters of the energy function can be identified with the stiffness matrix [25]. (3) The potential energy functions should be *frame-indifferent*. If both rigid bodies undergo the same rigid body transformation then the potential energy should be unchanged. Frame-indifference implies that Newton's third law of motion does hold, thus the wrenches acting on the bodies are equal and opposite. (4) The potential energy function should be *port-indifferent*. If a potential function is port-indifferent, then it does not matter which body is named which. So, reversing the names of the frames does not influence the potential energy. In [24] and the follow-up paper [26], Fasse en Breedveld modeled the elastic element as two rigid bodies, connected via a 6-dimensional spring. Furthermore, Fasse and Breedveld provided multiple spring wrenches, however without providing the corresponding potential energy functions. These wrenches differ in the parametrization of the pose. They provide a spring wrench based on a set of twists $\mathfrak{se}(3)$, which maps a set of rigid body transformation $SE(3)$ via the exponential mapping. This spring wrench based on twists is however not used, since it had no clear physical interpretation. Furthermore, they provide a method based on generalized coordinates where they parametrized the rotation by Euler angles, which is also not used in this report. When describing the orientation by an Euler (like) angle parametrization, this would give a discontinuity in the mapping. This discontinuity would appear for angles near 0 or 2π [27]. Therefore, in this report, we come up with a new potential energy function using the criteria defined by Fasse and Breedveld.

The work of Zhang [25, 28] is a continuation of the work of Fasse and Breedveld. Furthermore, Zhang gives a representation of rigid body displacement by using a combination of Cartesian coordinates and quaternions. The work of Qui shows a screw theory based stiffness analysis [29]. Furthermore, in [30], Qui provides a 6-dimensional compliance analysis and validation of ortho-planar springs. In [31], Zefran provides a geometric approach to the study of the Cartesian stiffness matrix. Stramigioli and Duinham did research to variable spatial spring control for robot control applications [32]. In [33], Rangel provided a dynamic analysis of a single cylinder hermetic reciprocating compressor. This paper could be interesting because he imposed some structure to the stiffness matrix based on the geometry of the system. Furthermore, [34] presents a method to identify nonlinear stiffness characteristics of elastic continuum mechanics. This identification

approach is not followed in this report, which is elaborated upon in Section 4.3.2. However, this paper could be useful for the improvement of the identification procedure of the stiffness and damping matrices in further research.

Some studies investigate the performance of suction cups. In the theoretical and experimental study [35], the performance of a flat suction cup is observed in the presence of lateral loads. Furthermore, research on fast pick-and-place systems with suction cups [36] has been performed. This research investigates the critically fast handling speed, which is the fastest possible movement when holding an object such that it does not slip or fall from the suction cup. These last two sources are interesting when studying the release of parcels, which is not a part of this report.

The challenge for this report is to come up with a model that describes the dynamics of the bellows suction cup during the holding phase. Therefore, we want to come up with a potential energy function that should describe the elastic energy of the bellows suction cup during the holding phase. Hereby, the potential energy function should satisfy the criteria as stated by Fasse and Breedveld. Furthermore, the damping of the bellows suction cup needs to be incorporated in the model to predict the package state during the holding phase.

1.3 Problem definition and research goal

To increase the productivity of the logistic work, automation is needed. The problem is that the current robotic manipulators are either too slow, too inflexible in usage, have a too large footprint, and/or are too expensive. A possible (partial) solution for parcel picking systems being too slow would be tossing the parcels instead of placing them by using a robot arm. However, there is still a lot unknown about the dynamic handling of parcels, such as the dynamic behavior of the bellows suction cup, which is used to hold the parcels. Therefore, numerical models should be created and validated to predict the trajectory and final state of the tossed package. More precisely, this report focuses on the identification and modeling of the bellows suction cup dynamics when holding a package. So in the scope of this report, the problem definition is stated as:

Due to the currently unmodeled bellows suction cup dynamics, it is impossible to predict the package state accurately, given the tool-arm trajectory and velocity.

With “package state”, we indicate the pose and velocity of the package. The research goal is defined directly from the problem definition, namely:

Construct and validate a model which describes the bellows suction cup dynamics, such that the state of a package (with known properties) held by the gripper can be predicted accurately given the tool-arm trajectory and velocity, and given underpressure in the bellows suction cup.

This research goal is divided into several sub-goals:

1. *Collect relevant measurement data on the bellows suction cup dynamics and system parameters, and ensure that the data is reusable and publicly available to stimulate further research on this topic.*
2. *Construct a model which describes the state (pose and velocity) of the fully known parcel when held by the gripper.*
3. *Determine the limits of the constructed model, i.e., until what working speed (different accelerations and velocities of the robot arm and package) and for what package properties should the model still predict the state of the package accurately.*

The goal is to build a model which can predict the state of packages up to 4kg, as this is the intended maximum weight of the parcels that will be tossed, for a given tool-arm trajectory and

velocity. It is however hard to give an exact maximum allowed error of the predicted state, because one of the goals of the I.A.M. project is to predict the final parcel state when the parcel has landed on the conveyor. This means that the maximum allowed error of the model describing the holding phase depends on the accuracy of the models describing the release of the parcel and the model describing the impact dynamics of the parcel on the conveyor. However, a first estimation for the maximum allowed error could be a maximum of 5% error for making a shacking motion with the tooling arm up to 3Hz.

The last sub-goal would be:

4. *Compare the numerical and experimental data and determine the accuracy of the model.*

Note that this project focuses on the identification and modeling of the dynamic behavior of the bellows suction cup, solely during the holding phase. This means that only the deformation of the bellows suction cup, as a result of the forces and moments working on the suction cup lip, is considered. For predicting the actual state of the package at the moment of release, this report would not be sufficient. First of all, the release phase is not considered in this report. Additional research is needed to come up with a model which can describe the parcel-gripper dynamics during the release. Such model should contain the dependency of the package state on the pressure within the gripper. The use of blow-off will probably have a big influence on the package dynamics. The second point of attention would be the deformation of the cardboard packages themselves. The sides of the cardboard packages are quite flexible and the deformation of the package will have an influence on the parcel-gripper dynamics. To isolate the bellows suction cup dynamics, the plastic plate, as shown in Figure 1.3a, is used for performing the measurements instead of cardboard parcels. The plastic plate is much stiffer compared to the sides of cardboard parcels and therefore more suitable for performing experiments.

1.4 Structure of the report

The structure of this report will be as follows. Chapter 2 provides the mathematical preliminaries for the work in the remainder of the report. First, in Section 2.1, the used Lie group theory is elaborated, where after the used multibody notation for rigid body dynamics is presented, in Section 2.2. In Chapter 3, the modeling of the bellows suction cup is presented. This starts in Section 3.1 with the free body diagram of the bellows suction cup and package. Furthermore, the model describing the dynamics of the package is presented. This is followed by an elaboration on the modeling of the stiffness and damping of the bellows suction cup in Section 3.3 and Section 3.4, respectively. Finally, Section 3.5 provides information about the numerical implementation of the model in MATLAB, together with some validation of this numerical implementation. Chapter 4 provides the information of the model parameter identification and the experimental data. In Section 4.1, the measurement procedure and way of processing the data are presented. Hereafter, in Section 4.2, measurements to identify the nominal length of the bellows suction cup during the holding phase are presented. Next, in Section 4.3, the dynamic experiments to identify the stiffness and damping of the bellows suction cup are elaborated upon. In this section, the Savitzky-Golay filtering on $SO(3) \times \mathbb{R}^3$, which is used to obtain approximations of the velocities and accelerations, is elaborated upon. After that, the results of the parameter identification are presented in combination with the validation of these results. In Chapter 5, the conclusions of this report and the recommendations for further research on this topic are presented.

Chapter 2

Mathematical Preliminaries

This chapter will provide the mathematical preliminaries for this report. First, in Section 2.1, the used Lie group theory is elaborated upon. Thereafter, in Section 2.2, the used notation will be introduced.

2.1 Lie groups theory

In this section, first the basic notation and operations on Lie groups are discussed. Next, two well-known Lie groups are discussed. These are: the Special Orthogonal group, in Section 2.1.2, which represents the orientation of a rigid body in 3D space; and the Special Euclidean group, Section 2.1.3, used to describe the pose of rigid bodies in 3D space. The required theory is already clearly presented by Jongeneel [37], and for reference purposes repeated in this section in a slightly altered form.

2.1.1 Preliminaries on Lie groups

A *Lie group* is a group, which also is a smooth differentiable manifold, consisting of a set \mathcal{G} and an operator \circ , such that the following properties hold [38]:

- For any $g_1, g_2 \in \mathcal{G}$ it holds that if $g_1 \circ g_2 = g_3$, then $g_3 \in \mathcal{G}$.
- For any $g_1, g_2, g_3 \in \mathcal{G}$ it holds that $(g_1 \circ g_2) \circ g_3 = g_1 \circ (g_2 \circ g_3)$.
- There exist an element $e \in \mathcal{G}$, known as the *identity*, such that for any $g_1 \in \mathcal{G}$ it holds that $g_1 \circ e = g_1$ and $e \circ g_1 = g_1$.
- Every element $g_1 \in \mathcal{G}$ has an *inverse*, denoted by g_1^{-1} such that $g_1^{-1} \in \mathcal{G}$ and for which holds that $g_1^{-1} \circ g_1 = e$ and $g_1 \circ g_1^{-1} = e$.

In a Lie group, the group operator and inversion are smooth functions. Furthermore, a Lie group is known to be *abelian* if $g_1 \circ g_2 = g_2 \circ g_1$ for $g_1, g_2 \in \mathcal{G}$. It is however well known that both the Special Euclidean group SE(3) as well as the Special Orthogonal group SO(3) are nonabelian groups, such that we can distinguish a *left* and a *right* translation, which will become clear in Section 2.2. We will assume the operation is understood from the context, such that we will omit its symbol for the sake of brevity.

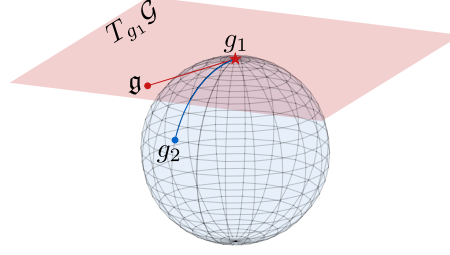


Figure 2.1: The exponential and logarithmic mappings on a Lie group transfer points between the group and the tangent space. Here, g_2 is mapped to \mathfrak{g} in the tangent space at g_1 by the logarithmic mapping. The inverse operation is accomplished by the exponential mapping.

The exponential and logarithmic map of a Lie group. Every Lie group comes with a *Lie algebra*, which is the tangent space of the Lie group at the identity endowed with a binary operation. The exponential and logarithmic map allow to transfer elements between the Lie group and the Lie algebra. The exponential map locally maps an element of the tangent space to the group, whereas the logarithmic map of a Lie group transfers elements from the Lie group to its tangent space. In Lie group theory, the group product and inversion allow to transfer the exponential and logarithmic mappings over the entire group. Consider Figure 2.1, where g_1 and g_2 are both elements of the group \mathcal{G} . A tangent space is considered at g_1 , indicated by $T_{g_1}\mathcal{G}$. A point $\mathfrak{g} \in T_{g_1}\mathcal{G}$ can now be mapped to the group, resulting in g_2 , according to

$$g_2 = g_1 \exp(\mathfrak{g}). \quad (2.1)$$

On the other hand, g_2 can be mapped to the tangent space $T_{g_1}\mathcal{G}$ resulting in \mathfrak{g} according to

$$\mathfrak{g} = \log(g_1^{-1}g_2). \quad (2.2)$$

For more information on Lie groups and Lie algebras, the reader is referred to [39].

Direct product of groups. Another property of Lie groups allows us to combine groups. Given the Lie group \mathcal{H} with operation \bullet and group \mathcal{G} with operation \circ , it is given that the direct product of these groups, denoted as $\mathcal{H} \times \mathcal{G}$, is a Lie group as well. The formed Lie group consists of a set, which is a Cartesian product of the sets of \mathcal{H} and \mathcal{G} , which results in the ordered pairs (h, g) where $h \in \mathcal{H}$ and $g \in \mathcal{G}$. The resulting group operation is defined component-wise such that

$$(h_1, g_1)(h_2, g_2) = (h_1 \bullet h_2, g_1 \circ g_2). \quad (2.3)$$

2.1.2 The Special Orthogonal group SO(3)

The 3-dimensional *Special Orthogonal* group is formed by the set of $\mathbb{R}^{3 \times 3}$ orthogonal matrices with determinant equal to 1 given by

$$\text{SO}(3) := \{ \mathbf{R} \in \mathbb{R}^{3 \times 3} \mid \mathbf{R}^T \mathbf{R} = \mathbf{I}_3, \det(\mathbf{R}) = 1 \}, \quad (2.4)$$

which becomes a Lie group under the matrix product. The matrices \mathbf{R} are referred to as *rotation matrices* and describe the relative rotation of one frame to another. The Lie algebra of SO(3), denoted as $\mathfrak{so}(3)$, is identified by the 3×3 skew-symmetric matrices of the form

$$\boldsymbol{\omega}^\wedge := \begin{bmatrix} 0 & -\omega_z & \omega_y \\ \omega_z & 0 & -\omega_x \\ -\omega_y & \omega_x & 0 \end{bmatrix} \in \mathfrak{so}(3), \quad (2.5)$$

where $\boldsymbol{\omega} = [\omega_x \ \omega_y \ \omega_z]^T \in \mathbb{R}^3$ and $(\cdot)^\wedge$ is known as the *hat*-operator as in [40, 41]. The exponential mapping for $\text{SO}(3)$ can efficiently be computed using Rodrigues' formula as in [42, 43] such that

$$\mathbf{R} = \mathbf{I}_3 + \frac{\sin(\|\boldsymbol{\omega}\|)}{\|\boldsymbol{\omega}\|} \boldsymbol{\omega}^\wedge + \frac{(1 - \cos(\|\boldsymbol{\omega}\|))}{\|\boldsymbol{\omega}\|^2} (\boldsymbol{\omega}^\wedge)^2, \quad (2.6)$$

where $\|\boldsymbol{\omega}\| = \sqrt{\omega_x^2 + \omega_y^2 + \omega_z^2}$. It is convenient to know that ω_x, ω_y , and ω_z form the direction of rotation and $\theta = \|\boldsymbol{\omega}\|$ gives the corresponding angle of rotation. The logarithmic map is then effectively computed by inverting (2.6), which yields

$$\theta = \begin{cases} \cos^{-1}\left(\frac{\text{tr}(\mathbf{R})-1}{2}\right) & \text{if } \mathbf{R} \neq \mathbf{I}_3, \\ 2\pi k & \text{if } \mathbf{R} = \mathbf{I}_3, \end{cases} \quad (2.7)$$

$$\boldsymbol{\omega}^\wedge = \begin{cases} \frac{\theta}{2\sin(\theta)} (\mathbf{R} - \mathbf{R}^T) & \text{if } \mathbf{R} \neq \mathbf{I}_3, \\ \mathbf{0} & \text{if } \mathbf{R} = \mathbf{I}_3, \end{cases} \quad (2.8)$$

where k is an arbitrarily chosen integer. Note that the exponential map is a many-to-one map such that representations of \mathbf{R} that rely on $\boldsymbol{\omega}$ are not uniquely covering $\text{SO}(3)$ [44]. Furthermore, the inverse is given by the matrix inverse and the identity element is given by the 3×3 identity matrix \mathbf{I}_3 .

2.1.3 The Special Euclidean group $\text{SE}(3)$

The 3-dimensional *Special Euclidean* group is formed by the set given by

$$\text{SE}(3) := \left\{ \mathbf{H} = \begin{bmatrix} \mathbf{R} & \mathbf{p} \\ \mathbf{0}_{1 \times 3} & 1 \end{bmatrix} \in \mathbb{R}^{4 \times 4} \mid \mathbf{R} \in \text{SO}(3), \mathbf{p} \in \mathbb{R}^3 \right\}, \quad (2.9)$$

which becomes a Lie group under the matrix product. It is often referred to as the group of rigid body transformations, and \mathbf{H} is often referred to as a *homogeneous transformation matrix*. The Lie algebra of $\text{SE}(3)$, denoted by $\mathfrak{se}(3)$, is identified by the 4×4 matrices of the form

$$\begin{bmatrix} \boldsymbol{\omega}^\wedge & \mathbf{v} \\ \mathbf{0}_{1 \times 3} & 0 \end{bmatrix} \in \mathfrak{se}(3), \quad (2.10)$$

with $\boldsymbol{\omega}^\wedge \in \mathfrak{so}(3)$ and $\mathbf{v} \in \mathbb{R}^3$. Given a vector $\mathbf{v} = [\mathbf{v} \ \boldsymbol{\omega}]^T \in \mathbb{R}^6$ with $\mathbf{v} \in \mathbb{R}^3$ and $\boldsymbol{\omega} \in \mathbb{R}^3$, we apply the hat-operator to write \mathbf{v} as an element of $\mathfrak{se}(3)$ according to

$$\mathbf{v}^\wedge = \begin{bmatrix} \mathbf{v} \\ \boldsymbol{\omega} \end{bmatrix}^\wedge = \begin{bmatrix} \boldsymbol{\omega}^\wedge & \mathbf{v} \\ \mathbf{0}_{1 \times 3} & 0 \end{bmatrix} \in \mathfrak{se}(3). \quad (2.11)$$

Since $\boldsymbol{\omega}^\wedge$ is equal to an element in \mathbb{R}^3 with the cross product, we will in the remainder refer to this as $\boldsymbol{\omega} \in \mathbb{R}_\times^3$, where the subscript $(\cdot)_\times$ refers to the cross product on \mathbb{R}^3 . Physically, if \mathbf{v} and $\boldsymbol{\omega}$ are expressed in a body-fixed frame, \mathbf{v} corresponds to the linear velocity of the origin of that frame, while $\boldsymbol{\omega}$ corresponds to the angular velocity of the rigid body. In kinematics, elements of $\mathfrak{se}(3)$ are referred to as *twists*. The exponential mapping, which maps an element of $\mathfrak{se}(3)$ to $\text{SE}(3)$, is given by the matrix exponential and, as shown in [41], every rigid transformation can be written as the exponential of some twist. Furthermore, the inverse of an element $\mathbf{H} \in \text{SE}(3)$ is given by

$$\mathbf{H}^{-1} = \begin{bmatrix} \mathbf{R}^T & -\mathbf{R}^T \mathbf{p} \\ \mathbf{0}_{1 \times 3} & 1 \end{bmatrix}, \quad (2.12)$$

and the identity element is given by the 4×4 identity matrix \mathbf{I}_4 .

2.2 Multibody notation for rigid body dynamics

In this section, we present the notation of [40], as will be used throughout this report to describe rigid body dynamics. First, in Section 2.2.1 it is shown how we formally write the position and orientation of a rigid body. Next, in Sections 2.2.2 and 2.2.3, it is shown how the velocity of a rigid body is expressed. There after, Section 2.2.4 shows how external forces and torques applied to the rigid body are expressed. The content of these sections is an altered version of the work form Jongeneel [37], such that the frames correspond to the frame definitions as used in this project. At last, in Section 2.2.5, the used notation for differentiation in $SE(3)$, $SO(3)$, and \mathbb{R}^3 is presented.

2.2.1 Notation of coordinate frames and points

A coordinate frame is defined as the combination of a point, called the *origin*, and an *orientation frame* in the 3D space. A capital letter is used to denote each frame. As example, for a frame A , we will write its origin as \mathbf{o}_A and its orientation frame as $[A]$ such that, formally, we write $A = (\mathbf{o}_A, [A])$. Coordinate frames can move through space in time with respect to other coordinate frames. They are typically assigned to rigid bodies to describe their position and orientation in space.

For a point \mathbf{p} , its coordinates with respect to A are written as the coordinate vector ${}^A\mathbf{p}$. This coordinate vector represents the 3D geometric vector $\vec{r}_{\mathbf{o}_A, \mathbf{p}}$ connecting the point \mathbf{p} with \mathbf{o}_A , pointing towards \mathbf{p} and is expressed in terms of A . Formally, we can write this as

$${}^A\mathbf{p} := \begin{bmatrix} \vec{r}_{\mathbf{o}_A, \mathbf{p}} \cdot \vec{x}_A \\ \vec{r}_{\mathbf{o}_A, \mathbf{p}} \cdot \vec{y}_A \\ \vec{r}_{\mathbf{o}_A, \mathbf{p}} \cdot \vec{z}_A \end{bmatrix} \in \mathbb{R}^3, \quad (2.13)$$

where \cdot denotes the scalar product and \vec{x}_A , \vec{y}_A , and \vec{z}_A are the unit vectors defining the orientation frame $[A]$. Given the frames A and B , we describe the coordinate transformation from B to A by use of the *rotation matrix* ${}^A\mathbf{R}_B \in SO(3)$. Note that this coordinate transformation is only depending on the orientation and is independent of the positions of \mathbf{o}_A and \mathbf{o}_B . To describe both the position and orientation of frame B relative to frame A , hereafter referred to as the *pose*, we use the 4×4 *homogeneous transformation matrix* ${}^A\mathbf{H}_B \in SE(3)$ given by

$${}^A\mathbf{H}_B := \begin{bmatrix} {}^A\mathbf{R}_B & {}^A\mathbf{o}_B \\ \mathbf{0}_{1 \times 3} & 1 \end{bmatrix}. \quad (2.14)$$

2.2.2 Notation of rotational velocity

Any point \mathbf{p} attached to a rigid body with coordinate frame B follows a path in spacial coordinates given by

$${}^A\mathbf{p}(t) = {}^A\mathbf{R}_B(t) {}^B\mathbf{p}. \quad (2.15)$$

The velocity of ${}^A\mathbf{p}(t)$ is then given by the time derivative of (2.15), resulting in

$${}^A\dot{\mathbf{p}} = \frac{d}{dt}({}^A\mathbf{p}(t)) = {}^A\dot{\mathbf{R}}_B(t) {}^B\mathbf{p}. \quad (2.16)$$

It follows that we can rewrite equation (2.16) as

$${}^A\dot{\mathbf{p}} = {}^A\dot{\mathbf{R}}_B {}^A\mathbf{R}_B^{-1} {}^A\mathbf{R}_B {}^B\mathbf{p}, \quad (2.17)$$

where we omitted the time dependencies for the sake of brevity. We can now conveniently define the *instantaneous spatial angular velocity* as ${}^A\boldsymbol{\omega}_{A,B} \in \mathbb{R}^3$, given by

$${}^A\boldsymbol{\omega}_{A,B}^\wedge := {}^A\dot{\mathbf{R}}_B {}^A\mathbf{R}_B^{-1}, \quad (2.18)$$

where we used $(\cdot)^\wedge$ as the *hat*-operator to write an element of \mathbb{R}^3 as a skew-symmetric matrix according to (2.5). Similar to (2.18) we define the *instantaneous body angular velocity* as ${}^B\boldsymbol{\omega}_{A,B} \in \mathbb{R}^3$, which is given by

$${}^B\boldsymbol{\omega}_{A,B}^\wedge := {}^A\mathbf{R}_B^{-1}A\dot{\mathbf{R}}_B. \quad (2.19)$$

2.2.3 Notation of rigid body velocity

We now consider both angular and linear velocities of a frame. Consider the homogeneous matrix mapping a point expressed in terms of frame B to a point expressed in terms of frame A , as given by (2.14). Similar to the property that multiplying ${}^A\mathbf{R}_B$ by ${}^A\mathbf{R}_B^{-1}$ results in a skew-symmetric matrix, we can apply a similar operation to the homogeneous matrix. Multiplying ${}^A\dot{\mathbf{H}}_B$ from the right by the inverse of ${}^A\mathbf{H}_B$ leads to

$$\begin{aligned} {}^A\dot{\mathbf{H}}_B {}^A\mathbf{H}_B^{-1} &= \begin{bmatrix} A\dot{\mathbf{R}}_B & A\dot{\mathbf{o}}_B \\ \mathbf{0}_{1 \times 3} & 0 \end{bmatrix} \begin{bmatrix} A\mathbf{R}_B^T & -A\mathbf{R}_B^T A\mathbf{o}_B \\ \mathbf{0}_{1 \times 3} & 1 \end{bmatrix} \\ &= \begin{bmatrix} A\dot{\mathbf{R}}_B A\mathbf{R}_B^T & A\dot{\mathbf{o}}_B - A\dot{\mathbf{R}}_B A\mathbf{R}_B^T A\mathbf{o}_B \\ \mathbf{0}_{1 \times 3} & 0 \end{bmatrix} \\ &= \begin{bmatrix} A\boldsymbol{\omega}_{A,B}^\wedge & A\mathbf{v}_{A,B} \\ \mathbf{0}_{1 \times 3} & 0 \end{bmatrix}, \end{aligned} \quad (2.20)$$

which takes the same form of (2.11), and is an element of $\mathfrak{se}(3)$. The *right trivialized* velocity of frame B with respect to frame A is then defined as

$${}^A\mathbf{v}_{A,B} := \begin{bmatrix} A\mathbf{v}_{A,B} \\ A\boldsymbol{\omega}_{A,B} \end{bmatrix} \in \mathbb{R}^6. \quad (2.21)$$

Similarly, by multiplying on the left, one obtains

$$\begin{aligned} {}^A\mathbf{H}_B^{-1}A\dot{\mathbf{H}}_B &= \begin{bmatrix} A\mathbf{R}_B^T & -A\mathbf{R}_B^T A\mathbf{o}_B \\ \mathbf{0}_{1 \times 3} & 1 \end{bmatrix} \begin{bmatrix} A\dot{\mathbf{R}}_B & A\dot{\mathbf{o}}_B \\ \mathbf{0}_{1 \times 3} & 0 \end{bmatrix} \\ &= \begin{bmatrix} A\mathbf{R}_B^T A\dot{\mathbf{R}}_B & A\mathbf{R}_B^T A\dot{\mathbf{o}}_B \\ \mathbf{0}_{1 \times 3} & 0 \end{bmatrix} \\ &= \begin{bmatrix} B\boldsymbol{\omega}_{A,B}^\wedge & B\mathbf{v}_{A,B} \\ \mathbf{0}_{1 \times 3} & 0 \end{bmatrix}, \end{aligned} \quad (2.22)$$

which results in the *left trivialized* velocity of frame B with respect to frame A , given by

$${}^B\mathbf{v}_{A,B} := \begin{bmatrix} B\mathbf{v}_{A,B} \\ B\boldsymbol{\omega}_{A,B} \end{bmatrix} \in \mathbb{R}^6. \quad (2.23)$$

The relation between the right and left trivialized velocity is given by the so called adjoint map [45]. We will denote this by ${}^A\mathbf{X}_B$ and define it as

$${}^A\mathbf{X}_B := \begin{bmatrix} A\mathbf{R}_B & A\mathbf{o}_B^\wedge A\mathbf{R}_B \\ \mathbf{0}_{3 \times 3} & A\mathbf{R}_B \end{bmatrix} \in \mathbb{R}^{6 \times 6}, \quad (2.24)$$

such that the right and left trivialized velocities are related through

$${}^A\mathbf{v}_{A,B} = {}^A\mathbf{X}_B {}^B\mathbf{v}_{A,B}. \quad (2.25)$$

2.2.4 Wrench notation

We can write the coordinates of a given wrench with respect to a frame B as

$${}_B\mathbf{f} := \begin{bmatrix} {}_B\mathbf{f} \\ {}_B\boldsymbol{\tau} \end{bmatrix} \in \mathbb{R}^6, \quad (2.26)$$

where ${}_B\mathbf{f}$ is the translational component of the wrench and ${}_B\boldsymbol{\tau}$ the angular component. This wrench can be expressed in terms of another frame A by the use of the wrench coordinate transformation ${}_A\mathbf{X}^B$ such that

$${}_A\mathbf{f} = {}_A\mathbf{X}^B {}_B\mathbf{f}. \quad (2.27)$$

This coordinate transformation is closely related to the adjoint map ${}^A\mathbf{X}_B$, given by (2.24), and is defined as

$${}_A\mathbf{X}^B := {}^B\mathbf{X}_A^T = \begin{bmatrix} {}^A\mathbf{R}_B & \mathbf{0}_{3 \times 3} \\ -{}^A\mathbf{R}_B {}^B\mathbf{o}_A^\wedge & {}^A\mathbf{R}_B \end{bmatrix} = \begin{bmatrix} {}^A\mathbf{R}_B & \mathbf{0}_{3 \times 3} \\ {}^A\mathbf{o}_B^\wedge {}^A\mathbf{R}_B & {}^A\mathbf{R}_B \end{bmatrix}. \quad (2.28)$$

In some cases, one needs to express the wrench with respect to a frame B with the orientation in terms of frame A . This is for example the case with gravity, where the direction of the gravity force is independent of time with respect to the inertial frame A . This is possible by introducing a new frame by combining the frames A and B . This frame is given as $B[A] := (\mathbf{o}_B, [A])$, hence, the frame whose origin coincides with the origin of B and whose orientation coincides with the orientation of A . In such a case, we can express the wrench as ${}_{B[A]}\mathbf{f}$. The relation between ${}_{B[A]}\mathbf{f}$ and ${}_B\mathbf{f}$ is then given by

$${}_B\mathbf{f} = {}_B\mathbf{X}^{B[A]} {}_{B[A]}\mathbf{f}, \quad (2.29)$$

where, from (2.28), we obtain

$${}_B\mathbf{X}^{B[A]} = \begin{bmatrix} {}^A\mathbf{R}_B^T & \mathbf{0}_{3 \times 3} \\ \mathbf{0}_{3 \times 3} & {}^A\mathbf{R}_B^T \end{bmatrix}. \quad (2.30)$$

Finally, the time derivative of a wrench coordinate transformation ${}_A\mathbf{X}^B$ is given by

$${}_A\dot{\mathbf{X}}^B = {}_A\mathbf{X}^B {}^B\mathbf{v}_{A,B} \bar{\times}^*, \quad (2.31)$$

where $\bar{\times}^*$ represents the dual cross-product between a twist and a wrench as in [40] and whose matrix representation is given by

$${}^B\mathbf{v}_{A,B} \bar{\times}^* = \begin{bmatrix} {}^B\boldsymbol{\omega}_{A,B}^\wedge & \mathbf{0}_{3 \times 3} \\ {}^B\mathbf{v}_{A,B}^\wedge & {}^B\boldsymbol{\omega}_{A,B}^\wedge \end{bmatrix}. \quad (2.32)$$

2.2.5 Notation of derivatives

Last, we consider the notation used for taking derivative on $\text{SE}(3)$. Let ${}^A\delta\mathbf{H}_B$ denote the infinitesimal perturbation of the pose of frame B with respect to frame A , such that ${}^A\delta\mathbf{H}_B \in T_{\mathbf{H}_B}\text{SE}(3)$. This can be expanded into the rotational and translation components as

$${}^A\delta\mathbf{H}_B = \begin{bmatrix} {}^A\delta\mathbf{R}_B & {}^A\delta\mathbf{o}_B \\ \mathbf{0}_{1 \times 3} & 0 \end{bmatrix}, \quad (2.33)$$

where ${}^A\delta\mathbf{R}_B \in T_{\mathbf{R}_B}\text{SO}(3)$. Now, let

$${}^B\boldsymbol{\Delta}_{A,B}^\wedge := {}^A\mathbf{H}_B^{-1} {}^A\delta\mathbf{H}_B, \quad (2.34)$$

where ${}^B\boldsymbol{\Delta}_{A,B}^\wedge \in \mathbb{R}^6$ denotes the trivialized infinitesimal perturbation. Note that ${}^B\boldsymbol{\Delta}_{A,B}^\wedge$ is a twist and that ${}^B\boldsymbol{\Delta}_{A,B}^\wedge \in \mathfrak{se}(3)$. Again, expanding into rotational and translation components we have

$${}^B\boldsymbol{\Delta}_{A,B}^\wedge = \begin{bmatrix} {}^B\boldsymbol{\Delta}_{A,B}^\circ \\ {}^B\boldsymbol{\Delta}_{A,B}^\mathbf{R} \end{bmatrix}^\wedge = \begin{bmatrix} {}^B\boldsymbol{\Delta}_{A,B}^\mathbf{R}^\wedge & {}^B\boldsymbol{\Delta}_{A,B}^\circ \\ \mathbf{0}_{1 \times 3} & 0 \end{bmatrix}, \quad (2.35)$$

in which ${}^B\Delta_{A,B}^{\circ}$ denotes the linear part of the twist and ${}^B\Delta_{A,B}^{\mathbf{R}}$ the angular part of the twist, such that ${}^B\Delta_{A,B}^{\mathbf{R}\wedge} \in \mathfrak{so}(3)$. We can write (2.34) as

$${}^A\delta\mathbf{H}_B := {}^A\mathbf{H}_B {}^B\Delta_{A,B}^{\wedge}, \quad (2.36)$$

which can be expanded in

$${}^A\delta\mathbf{R}_B = {}^A\mathbf{R}_B {}^B\Delta_{A,B}^{\mathbf{R}\wedge}, \quad (2.37)$$

$${}^A\delta\mathbf{o}_B = {}^A\mathbf{R}_B {}^B\Delta_{A,B}^{\circ}. \quad (2.38)$$

Equations (2.37) and (2.38) are expressions for the infinitesimal perturbation of the orientation and position, which can be used for taking the partial derivative of a function which depends on ${}^A\mathbf{H}_B$.

Chapter 3

Modeling the Bellows Suction Cup Dynamics

In this chapter, the model used to describe the dynamics of the bellows suction cup during the holding phase is introduced. First, in Section 3.1, the used coordinate frames and the equations of motion are introduced. In Section 3.2, the nominal configuration of the bellows suction cup during the holding phase is discussed. Hereafter, the stiffness and damping are elaborated upon in Sections 3.3 and 3.4. The developed model will be used to simulate the forward dynamics, of which the numerical implementation is discussed in Section 3.5.

3.1 Frame definitions and equations of motion

In this work, we will use frame A as an inertial frame, fixed with respect to the world surface, and we express all motions with respect to this frame. We assign frame B to the center of mass of the parcel or to the center of mass of plastic plate with rigidly attached weights, as shown in Figure 1.3a. Furthermore, we assign the frame S to the center of the contact area of the suction cup lip with the package. These coordinate frames are schematically depicted in Figure 3.1.

From manual inspection can be concluded that it takes quite some force to make the suction cup lip slip over the surface of the package/object held by the gripper. Therefore, the following assumption is made.

Assumption 1 *There is no slip between the suction cup lip and the package/object held by the gripper during the holding phase.*

Furthermore, in this project we assume.

Assumption 2 *The package/object held by the gripper is rigid and does not deform.*

Because of this assumption, the experiments are performed using a plastic plate with the rigidly attached weights, as shown in Figure 1.3a, because the plastic plate is much stiffer compared to the cardboard parcels. Because the weights are rigidly attached to the plastic plate, we also have the following assumption.

Assumption 3 *There is no moving mass in the parcel, the center of mass is always at the same position in the parcel, so frame B will not move with respect to the parcel itself.*

Because of these assumptions, we can say that the pose of the package with respect to the suction cup lip is fixed, thus ${}^S\mathbf{H}_B$ is a constant. In other words, the bellows suction cup lip and the parcel/object held by the gripper form one rigid body, with two assigned frames: frame S at the

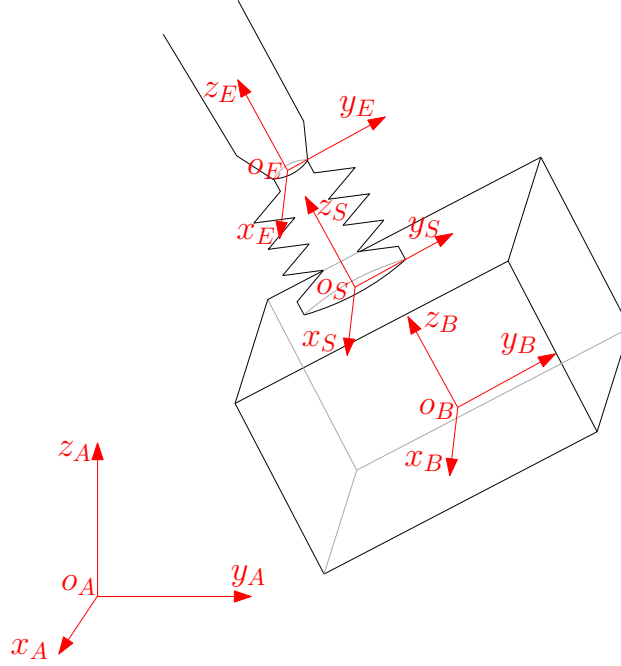


Figure 3.1: Frames E is the coordinate frame fixed to the tip of the tooling arm, the point where the end-effector (bellows suction cup) is attached. Frame S is the coordinate frame fixed to the center of the contact area of the suction cup lip with the package. Frame B is the frame fixed to the center of mass of the package. Frame A is the absolute reference frame, which does not move with respect to the earth.

center of the contact surface of the suction cup lip and package, and frame B at the center of mass. By choice, we define that $[S] := [B]$ for the holding phase, which means that ${}^S\mathbf{R}_B := \mathbf{I}_3$. In order to make a model of the holding phase, insights into the forces and moments between the bellows suction cup and package are needed. Figure 3.2 shows a Free Body Diagram (FBD) which contains these forces and moments. According to the third law of Newton, we state that

$${}^E\mathbf{f}_{TA \rightarrow SC} = -{}^E\mathbf{f}_{SC \rightarrow TA} \quad (3.1)$$

and

$${}^S\mathbf{f}_{PA \rightarrow SC} = -{}^S\mathbf{f}_{SC \rightarrow PA}, \quad (3.2)$$

where ${}^E\mathbf{f}_{TA \rightarrow SC}$ is the wrench acting from the tool-arm on the suction cup at frame E , ${}^E\mathbf{f}_{SC \rightarrow TA}$ is the wrench acting from the suction cup on the tool-arm at frame E , ${}^S\mathbf{f}_{PA \rightarrow SC}$ is the wrench acting from the package on the suction cup at frame S , and ${}^S\mathbf{f}_{SC \rightarrow PA}$ is the wrench acting from the suction cup on the package at frame E .

Assumption 4 *We assume that the bellows suction cup itself is massless as the deformation of the bellows suction cup is mainly the result of the gravity and inertial forces of the held package.*

Therefore, we can write the wrench equality

$${}^E\mathbf{f}_{TA \rightarrow SC} = -{}^E\mathbf{f}_{PA \rightarrow SC}, \quad \text{or} \quad {}^S\mathbf{f}_{TA \rightarrow SC} = -{}^S\mathbf{f}_{PA \rightarrow SC}, \quad (3.3)$$

where ${}^E\mathbf{f}_{TA \rightarrow SC}$ is the wrench acting from the tool-arm on the suction cup at frame E ; ${}^E\mathbf{f}_{PA \rightarrow SC}$ is the wrench acting from the package on the suction cup, written in frame E ; ${}^S\mathbf{f}_{TA \rightarrow SC}$ is the wrench acting from the tool-arm on the suction cup, written in frame S ; and ${}^S\mathbf{f}_{PA \rightarrow SC}$ is the wrench acting from the package on the suction cup at frame S .

Although it is not of importance in this report, the tool-arm is not assumed to be massless. Because of the mass of the tool-arm, we have that

$${}^E\mathbf{f}_{RO\rightarrow TA} \neq -{}^E\mathbf{f}_{SC\rightarrow TA}, \quad (3.4)$$

where ${}^E\mathbf{f}_{RO\rightarrow TA}$ is the wrench acting from the robot arm on the tool-arm, written in frame E ; and ${}^E\mathbf{f}_{SC\rightarrow TA}$ is the wrench acting from the suction cup on the tool-arm at frame E .

In order to model the dynamics of the package interconnected to the bellows suction cup during the holding phase, we make use of Newton-Euler equations [27], given as

$${}_B\mathbb{M}_B^B \dot{\mathbf{v}}_{A,B} + {}^B\mathbf{v}_{A,B} \bar{\times} {}_B\mathbb{M}_B^B \mathbf{v}_{A,B} = {}_B\mathbf{X}^S s\mathbf{f}_{SC\rightarrow PA} + {}_B\mathbf{f}_g, \quad (3.5)$$

where ${}_B\mathbb{M}_B$ is the generalized inertia tensor of the package expressed in frame B , as elaborated upon in Appendix A, $s\mathbf{f}_{SC\rightarrow PA}$ is the wrench acting from the suction cup on the package at point

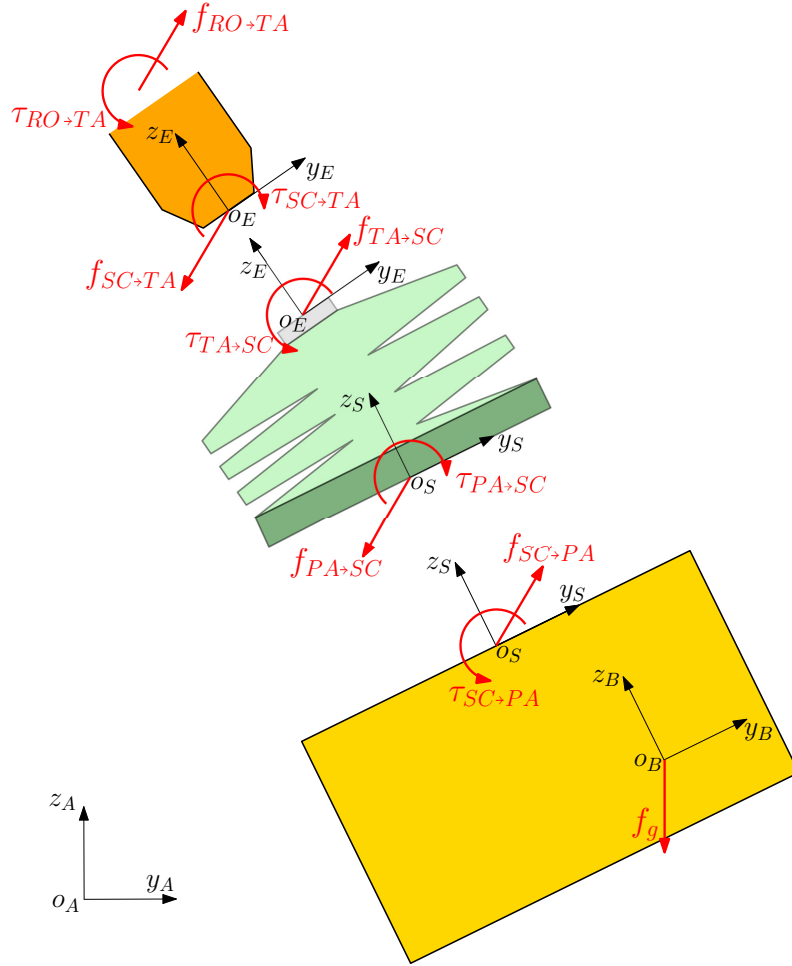


Figure 3.2: Free Body Diagram of the bellows suction cup and package in a planar perspective during the holding phase. In the picture are: \mathbf{f}_g the gravitational force acting on the center of mass of the package, $\mathbf{f}_{SC\rightarrow PA}$ and $\boldsymbol{\tau}_{SC\rightarrow PA}$ are the forces and moments acting on the package coming from the suction cup, $\mathbf{f}_{PA\rightarrow SC}$ and $\boldsymbol{\tau}_{PA\rightarrow SC}$ are the forces and moments acting on the suction cup coming from the package, $\mathbf{f}_{TA\rightarrow SC}$ and $\boldsymbol{\tau}_{TA\rightarrow SC}$ are the forces and moments acting on the suction cup coming from the tooling arm, $\mathbf{f}_{SC\rightarrow TA}$ and $\boldsymbol{\tau}_{SC\rightarrow TA}$ are the forces and moments acting on the tooling arm coming from the suction cup, and $\mathbf{f}_{RO\rightarrow TA}$ and $\boldsymbol{\tau}_{RO\rightarrow TA}$ are the forces and moments acting on the tooling arm coming from the robot.

S , and ${}_B\mathbf{f}_g$ is the wrench describing the gravity acting at frame B , which is positioned at the center of mass of the package. The gravity acting on the package is written as

$${}_B\mathbf{f}_g = \begin{bmatrix} -mg {}^A\mathbf{R}_B^{-1} {}^A\mathbf{z}_A \\ \mathbf{0}_{3 \times 1} \end{bmatrix}, \quad (3.6)$$

where g is the gravitational acceleration. Note that the gravity acts per definition in the $-z_A$ direction.

To model the dynamic behavior of the bellows suction cup and package during the holding phase, the bellows suction cup and the interconnected package will be modeled as a mass-spring-damper system. The wrench acting from the suction cup on the package, ${}_S\mathbf{f}_{SC \rightarrow PA}$, is the result of the stiffness and damping of the bellows suction cup. Therefore, we have

$${}_S\mathbf{f}_{SC \rightarrow PA} = {}_S\mathbf{f}_{SC \rightarrow PA, spring}(\mathbf{K}, {}^E\mathbf{H}_S) + {}_S\mathbf{f}_{SC \rightarrow PA, damper}(\mathbf{D}, {}^S\mathbf{v}_{E,S}), \quad (3.7)$$

where ${}_S\mathbf{f}_{SC \rightarrow PA, spring}(\mathbf{K}, {}^E\mathbf{H}_S)$ is the wrench resulting from the stiffness of the bellows suction cup, which depends on the pose of frame S with respect to frame E and stiffness matrix \mathbf{K} , and ${}_S\mathbf{f}_{SC \rightarrow PA, damper}(\mathbf{D}, {}^S\mathbf{v}_{E,S})$ is the wrench resulting from the damping of the bellows suction cup, which depends on the velocity of frame S with respect to frame E and damping matrix \mathbf{D} . The derivation of the spring and damper wrenches are presented in Sections 3.3 and 3.4, respectively. Note that during the holding phase a (partial) vacuum is created by the ejector to hold the package. Regarding this vacuum, we adopt the following assumption.

Assumption 5 *The underpressure within the gripper maintains constant during the holding phase.*

Because of this assumption, it is not necessary to model the force acting on the package as the result of the underpressure within the bellows suction cup. This will be elaborated upon in the next section. Furthermore, note that by writing the wrench that acts between the suction cup lip and the package as (3.7), we make use of Assumption 1. Since we assume no slip between the suction cup lip and package, there is no need to model the friction between the suction cup lip and the package.

3.2 Nominal configuration bellows suction cup

When modeling the bellows suction cup and package as a mass-spring-damper system, we need to consider the nominal configuration of the bellows suction cup. A choice could be the unloaded suction cup, i.e., a suction cup that does not hold an object, as shown in Figure 3.3a. Herein, l_0 indicates the nominal length of the bellows suction cup. Choosing this as the nominal configuration results in the following static force equilibrium when holding a package, as shown in Figure 3.3b,

$$\left({}_S\mathbf{f}_{SC \rightarrow Pa, spring}(\mathbf{K}, {}^E\mathbf{H}_S) + {}_S\mathbf{X}^B {}_B\mathbf{f}_g \right) + {}_S\mathbf{f}_{SC \rightarrow Pa, pres} = 0, \quad (3.8)$$

where ${}_S\mathbf{f}_{SC \rightarrow Pa, pres}$ is the wrench resulting from the underpressure within the suction cup. From this, it can be concluded that by choosing the nominal configuration of the bellows suction cup as the configuration during rest, we need to model both the spring force and the force resulting from the underpressure.

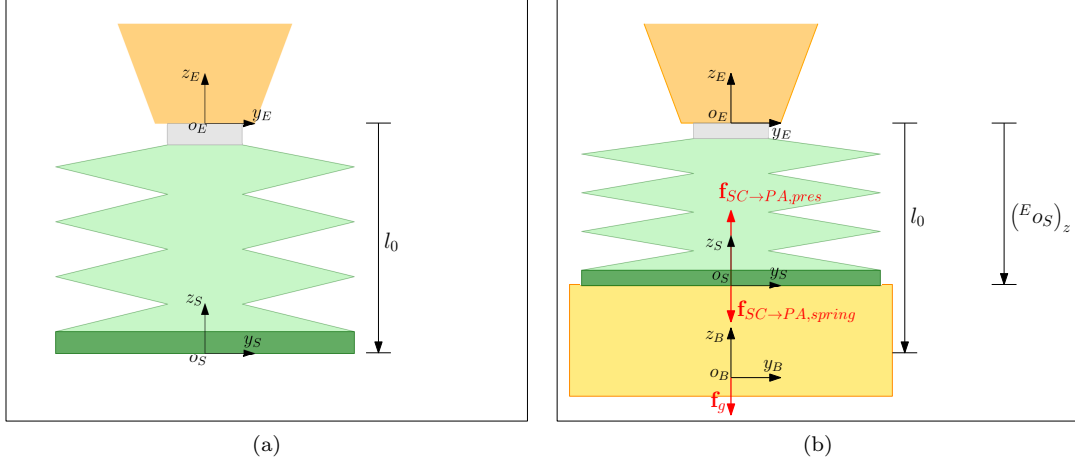


Figure 3.3: Two schematic representations of the bellows suction cup are presented. Figure (a) shows the first option for the nominal configuration of the bellows suction cup, namely a suction cup which is not loaded with any package. Figure (b) shows the forces which need to be modeled when using the nominal configuration as depicted in Figure (a).

Another option for the nominal configuration is shown in Figure 3.4a, where l_0 again indicates the nominal length of the bellows suction cup. Herein is schematically shown how the bellows suction cup is being compressed by holding an ideal massless plate. By choosing this as the nominal configuration and because of Assumption 5, we obtain the static equilibrium as in Figure 3.4b, when holding a package of a certain mass. This static equilibrium can be written as

$${}_S \mathbf{f}_{SC \rightarrow Pa, spring} (\mathbf{K}, {}^E \mathbf{H}_S) + {}_S \mathbf{X}_B^B \mathbf{f}_g (m) = 0. \quad (3.9)$$

From (3.9), it can be concluded, that by choosing the nominal configuration as in Figure 3.4a, only the stiffness needs to be modeled and thus not the pressure effect. This simplifies the model which will be built to describe the bellows suction cup dynamics during the holding phase. Therefore,

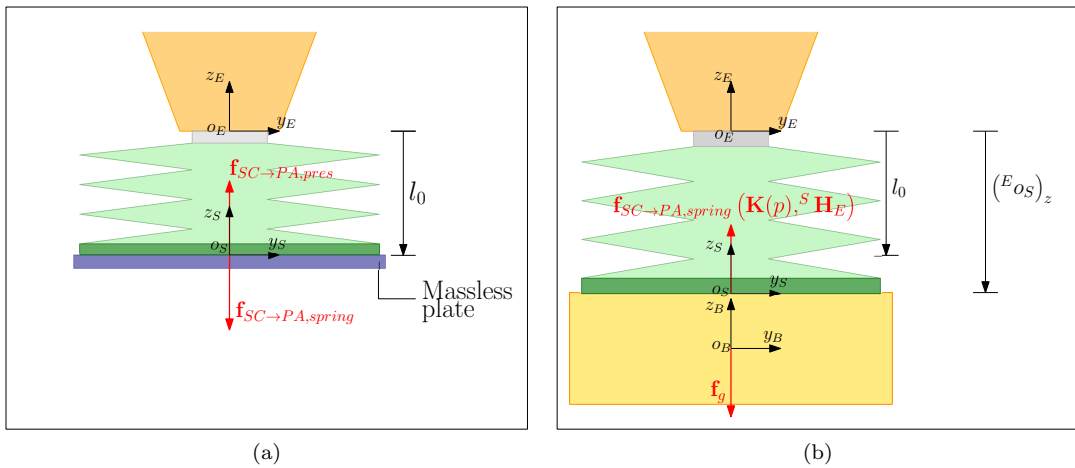


Figure 3.4: Two schematic representations of the compressed bellows suction cup are presented. Figure (a) shows the chosen nominal configuration of the bellows suction cup, namely the compressed bellows suction cup when holding an ideal massless plate. Figure (b) shows the forces which need to be modeled when using the nominal configuration as depicted in Figure (a).

in the scope of this report, we choose the nominal length of the bellows suction as indicated in Figure 3.4a.

By choosing the nominal bellows suction cup length during the holding phase as in Figure 3.4a, we assumed that the pressure in the bellows suction cup stays constant. By changing the ejector setting, this pressure level within the suction cup can be changed. Be aware that changing this pressure level in the bellows suction cup would lead to a different nominal length of the bellows suction cup, l_0 , and a different stiffness of the bellows suction cup. The identification of the nominal length of the bellows suction cup during the holding phase is presented in Section 4.2.

3.3 Modeling of stiffness

In this section, the derivation of the spring wrench is presented. First, the frames for the relative displacement and the center of stiffness are introduced in Section 3.3.1. Next, the derivation of the spring wrench from a potential energy function is presented in Section 3.3.2. Finally, in Section 3.3.3, a small displacements approximation is given for the obtained spring wrench.

3.3.1 Frames for relative displacement

To obtain the spring wrench, ${}^S\mathbf{f}_{SC \rightarrow Pa, spring}$, we need to define the relative displacements of frame S with respect to frame E . Therefore, we introduce the frames S_1 and S_2 , which define the centers of stiffness [24, 25, 28, 29], as shown in Figure 3.5a. These frames are attached to each other via a coupled linear torsional spring. Furthermore, by definition it holds that $[S_1] = [S]$ and $[S_2] = [E]$. When the suction cup is in nominal pose, as shown in Figure 3.5b, we have that frames S_1 and S_2 coincide, which means that no spring force is working on the centers of stiffness.

The pose of frame S_1 with respect to S_2 in terms of frames E and S , can be obtained by

$${}^{S_2}\mathbf{H}_{S_1} \left({}^A\mathbf{H}_E, {}^A\mathbf{H}_S \right) = {}^{S_2}\mathbf{H}_E {}^A\mathbf{H}_E^{-1} {}^A\mathbf{H}_S {}^S\mathbf{H}_{S_1}. \quad (3.10)$$

The pose of the tooling arm and the suction cup lip, ${}^A\mathbf{H}_E$ and ${}^A\mathbf{H}_S$ respectively, are known from the measurement or simulation data. The remaining right-hand side terms of (3.10) can be

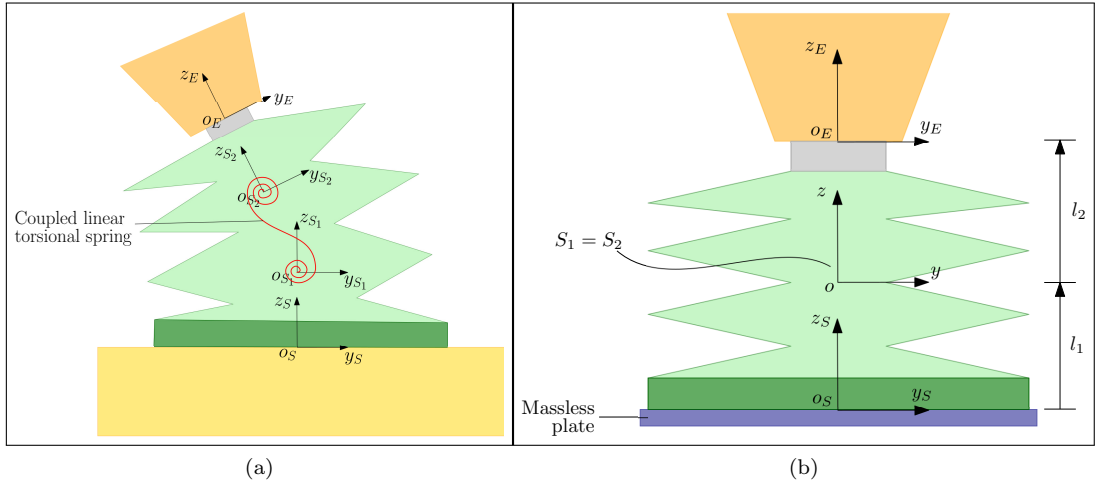


Figure 3.5: Two figures showing frames S_1 and S_2 . Figure (a) shows a schematic picture indicating frames S_1 and S_2 which are connected via a coupled linear torsional spring. Figure (b) shows the nominal pose of the bellows suction cup for the holding phase. The massless plate indicates that the bellows suction cup is compressed due to the underpressure within the gripper, but the bellows suction cup is not elongated due to the mass of a package.

explicitly written by

$${}^{S_2}\mathbf{H}_E = \left[\begin{array}{c|c} \mathbf{I}_3 & l_2 {}^E\mathbf{z}_E \\ \mathbf{0}_{1 \times 3} & 1 \end{array} \right], \quad (3.11)$$

$${}^S\mathbf{H}_{S_1} = \left[\begin{array}{c|c} \mathbf{I}_3 & l_1 {}^S\mathbf{z}_S \\ \mathbf{0}_{1 \times 3} & 1 \end{array} \right], \quad (3.12)$$

where l_1 and l_2 are the constant link lengths as indicated in Figure 3.5b, and ${}^E\mathbf{z}_E = {}^S\mathbf{z}_S = [0 \ 0 \ 1]^T$. Note that $({}^{S_2}\mathbf{o}_E)_x = ({}^{S_2}\mathbf{o}_E)_y = ({}^S\mathbf{o}_{S_1})_x = ({}^S\mathbf{o}_{S_1})_y = 0$, because of the symmetry of the bellows suction cup. Substitution of (3.11) and (3.12) in (3.10) gives

$${}^{S_2}\mathbf{H}_{S_1} ({}^E\mathbf{H}_S) = \left[\begin{array}{c|c} {}^E\mathbf{R}_S & l_2 {}^E\mathbf{z}_E + l_1 {}^E\mathbf{R}_S {}^S\mathbf{z}_S + {}^E\mathbf{o}_S \\ \mathbf{0}_{1 \times 3} & 1 \end{array} \right]. \quad (3.13)$$

The values for l_1 and l_2 are presented in Section 4.2.

3.3.2 Derivation spring wrench

To derive the spring wrench, we first need to come up with a spring potential energy function. From this spring potential energy function we can then derive a spring wrench which has a geometric meaning [24, 25, 28, 32]. At first thought, the following potential energy function would be a candidate to describe the elastic energy of a 6-degree-of-freedom spring:

$$P_0(\mathbf{H}) = \frac{1}{2} \left[\begin{array}{c} \mathbf{o} \\ \log(\mathbf{R})^\vee \end{array} \right]^T \mathbf{K} \left[\begin{array}{c} \mathbf{o} \\ \log(\mathbf{R})^\vee \end{array} \right], \quad (3.14)$$

where we used the short-hand notation $\mathbf{H} = {}^{S_2}\mathbf{H}_{S_1}$, $\mathbf{R} = {}^{S_2}\mathbf{R}_{S_1}$, and $\mathbf{o} = {}^{S_2}\mathbf{o}_{S_1}$. Furthermore, the stiffness matrix can be written as

$$\mathbf{K} = \left[\begin{array}{c|c} \mathbf{K}_{oo} & \mathbf{K}_{oR} \\ \mathbf{K}_{Ro} & \mathbf{K}_{RR} \end{array} \right] \in \mathbb{R}^{6 \times 6}, \quad (3.15)$$

where the translation (\mathbf{K}_{oo}) and orientation (\mathbf{K}_{RR}) terms are symmetric, and for the coupling terms hold that $\mathbf{K}_{oR} = \mathbf{K}_{Ro}^T$. Hence, the stiffness matrix \mathbf{K} is symmetric. Note that, in (3.14), the orientation of frame S_1 with respect to frame S_2 is written as the logarithmic mapping of the rotation matrix, which enables us to describe the orientation in three distinct rotations, in contrary to Euler angles [27, 41, 46, 47].

When verifying the criteria for an elastic potential energy function, as established by Fasse and Breedveld [24], we see that (3.14) is not port-indifferent, since that $P_0(\mathbf{H}) \neq P_0(\mathbf{H}^{-1})$. For this reason, the following potential energy function is suggested in this report:

$$P_0(\mathbf{H}) = \frac{1}{2} \left[\begin{array}{c} 1/2(\mathbf{I} + \mathbf{R}^T)\mathbf{o} \\ \log(\mathbf{R})^\vee \end{array} \right]^T \mathbf{K} \left[\begin{array}{c} 1/2(\mathbf{I} + \mathbf{R}^T)\mathbf{o} \\ \log(\mathbf{R})^\vee \end{array} \right], \quad (3.16)$$

where \mathbf{K} still has the same structure as in (3.15). This new potential energy function, (3.16), is port-indifferent and also satisfies the three other criteria of Fasse and Breedveld, as described in Section 1.2. Note that this chosen potential energy function is not the only possible potential energy function. There are possibly many more candidate potential energy functions, which could satisfy the requirements as stated by Fasse and Breedveld [24]. Just like (3.16), these potential energy functions should describe the local stiffness for small deformations, $\mathbf{R} \approx \mathbf{I}_3$ and $\mathbf{o} \approx \mathbf{0}_{3 \times 1}$.

The difference in these potential energy functions would be how they evolve for large deformation, $\mathbf{R} \not\approx \mathbf{I}_3$ and $\mathbf{o} \not\approx \mathbf{0}_{3 \times 1}$.

Implementation-wise, it would be computationally expensive to have a potential energy function like (3.16) because of the matrix logarithm of the rotation matrix. For this reason, we approximate the matrix logarithm in (3.16) by using (B.7), as presented in Appendix B. In this way, we obtain the following spring potential energy function:

$$P_0(\mathbf{H}) = \frac{1}{8} \begin{bmatrix} (\mathbf{I} + \mathbf{R}^T)\mathbf{o} \\ (\mathbf{R} - \mathbf{R}^T)^\vee \end{bmatrix}^T \mathbf{K} \begin{bmatrix} (\mathbf{I} + \mathbf{R}^T)\mathbf{o} \\ (\mathbf{R} - \mathbf{R}^T)^\vee \end{bmatrix}, \quad (3.17)$$

which will be used in this project.

Similar to one-degree-of-freedom spring systems, the wrench describing the spring forces and moments can be obtained by partially differentiating the elastic potential energy function with respect to the degrees of freedom. To write down the partial derivative of (3.17), we need to know the partial derivative $D\mathbf{h}(\mathbf{H}) \cdot \mathbf{H}\Delta^\wedge$, where $\Delta = {}^{S_1}\Delta_{S_2, S_1}$ and

$$\mathbf{h}(\mathbf{H}) := \begin{bmatrix} (\mathbf{I} + \mathbf{R}^T)\mathbf{o} \\ (\mathbf{R} - \mathbf{R}^T)^\vee \end{bmatrix}. \quad (3.18)$$

By using the notation as presented in Section 2.2.5, we obtain

$$D\mathbf{h}(\mathbf{H}) \cdot \mathbf{H}\Delta^\wedge = \begin{bmatrix} (\mathbf{I} + \mathbf{R}^T)\mathbf{R}\Delta^\circ + (\Delta^{\mathbf{R}^\wedge})^T \mathbf{R}^T \mathbf{o} \\ (\mathbf{R}\Delta^{\mathbf{R}^\wedge} - (\Delta^{\mathbf{R}^\wedge})^T \mathbf{R}^T)^\vee \end{bmatrix}. \quad (3.19)$$

By using $(\Delta^{\mathbf{R}^\wedge})^T \mathbf{R}^T \mathbf{o} = (\mathbf{R}^T \mathbf{o})^\wedge \Delta^{\mathbf{R}}$, we can write (3.19) as

$$D\mathbf{h}(\mathbf{H}) \cdot \mathbf{H}\Delta^\wedge = \begin{bmatrix} (\mathbf{R} + \mathbf{I}) \Delta^\circ + (\mathbf{R}^T \mathbf{o})^\wedge \Delta^{\mathbf{R}} \\ (\mathbf{R}\Delta^{\mathbf{R}^\wedge} - (\Delta^{\mathbf{R}^\wedge})^T \mathbf{R}^T)^\vee \end{bmatrix}. \quad (3.20)$$

By using (3.20), we can write the partial derivative of the used potential energy function, as

$$DP_0(\mathbf{H}) \mathbf{H}\Delta^\wedge = \frac{1}{4} \begin{bmatrix} (\mathbf{I} + \mathbf{R}^T)\mathbf{o} \\ (\mathbf{R} - \mathbf{R}^T)^\vee \end{bmatrix}^T \mathbf{K} \begin{bmatrix} (\mathbf{R} + \mathbf{I}) \Delta^\circ + (\mathbf{R}^T \mathbf{o})^\wedge \Delta^{\mathbf{R}} \\ (\mathbf{R}\Delta^{\mathbf{R}^\wedge} - (\Delta^{\mathbf{R}^\wedge})^T \mathbf{R}^T)^\vee \end{bmatrix}. \quad (3.21)$$

Then, by using

$$\left(\mathbf{R}\Delta^{\mathbf{R}^\wedge} - (\Delta^{\mathbf{R}^\wedge})^T \mathbf{R}^T \right)^\vee = (\text{tr}(\mathbf{R}) \mathbf{I}_3 - \mathbf{R}^T) \Delta^{\mathbf{R}}, \quad (3.22)$$

[48] and performing some algebraic manipulation, we can write (3.21) in the form

$$DP_0(\mathbf{H}) \mathbf{H}\Delta^\wedge = \frac{1}{4} \underbrace{\begin{bmatrix} (\mathbf{I} + \mathbf{R}^T)\mathbf{o} \\ (\mathbf{R} - \mathbf{R}^T)^\vee \end{bmatrix}^T \mathbf{K} \begin{bmatrix} \mathbf{R} + \mathbf{I} & (\mathbf{R}^T \mathbf{o})^\wedge \\ \mathbf{0}_{3 \times 3} & (\text{tr}(\mathbf{R}) \mathbf{I}_3 - \mathbf{R}^T) \end{bmatrix}}_{S_1 \mathbf{f}_{L_1 \rightarrow L_2, spring}^T} \Delta, \quad (3.23)$$

in which we expressed the partial derivative of the potential energy function as the product of a wrench with a twist. The spring wrench can be written explicitly, as

$$S_1 \mathbf{f}_{L_1 \rightarrow L_2, spring} = \frac{1}{4} \begin{bmatrix} \mathbf{R}^T + \mathbf{I}_3 & \mathbf{0}_{3 \times 3} \\ -(\mathbf{R}^T \mathbf{o})^\wedge & (\text{tr}(\mathbf{R}) \mathbf{I}_3 - \mathbf{R}) \end{bmatrix} \mathbf{K} \begin{bmatrix} (\mathbf{I}_3 + \mathbf{R}^T)\mathbf{o} \\ (\mathbf{R} - \mathbf{R}^T)^\vee \end{bmatrix}, \quad (3.24)$$

where L_1 and L_2 indicate the bodies fixed to frames S_1 and S_2 , respectively. So, L_1 is the part of the bellows suction cup between frame S_1 and S , and L_2 is the part of the bellows suction cup between frame S_2 and E , as shown in Figure 3.5a. Note that (3.24) is the spring wrench working on the center of stiffness S_1 . By using the wrench transformation ${}_S\mathbf{X}^{S_1}$, which is explicitly written as

$${}_S\mathbf{X}^{S_1} = \begin{bmatrix} \mathbf{I}_3 & \mathbf{0}_{3 \times 3} \\ l_1 {}^S\mathbf{z}_S^\wedge & \mathbf{I}_3 \end{bmatrix}, \quad (3.25)$$

we can write ${}_{S_1}\mathbf{f}_{L_1 \rightarrow L_2, spring}$ as the wrench acting on frame S by

$${}_S\mathbf{f}_{Pa \rightarrow SC, spring} = {}_S\mathbf{X}^{S_1} {}_{S_1}\mathbf{f}_{L_1 \rightarrow L_2}. \quad (3.26)$$

Writing (3.26) and reversing the direction of the wrench, such that we have the wrench acting from the suction cup on the package, we obtain

$${}_S\mathbf{f}_{SC \rightarrow Pa, spring} = -\frac{1}{4} \begin{bmatrix} \mathbf{I}_3 & \mathbf{0}_{3 \times 3} \\ l_1 {}^S\mathbf{z}_S^\wedge & \mathbf{I}_3 \end{bmatrix} \begin{bmatrix} \mathbf{R}^T + \mathbf{I}_3 & \mathbf{0}_{3 \times 3} \\ -(\mathbf{R}^T \mathbf{o})^\wedge & (\text{tr}(\mathbf{R}) \mathbf{I}_3 - \mathbf{R}) \end{bmatrix} \mathbf{K} \begin{bmatrix} (\mathbf{I}_3 + \mathbf{R}^T) \mathbf{o} \\ (\mathbf{R} - \mathbf{R}^T)^\vee \end{bmatrix}, \quad (3.27)$$

which represents the spring wrench we need for our model, Equations (3.5) and (3.7). In Appendix C, a derivation is provided on how we go from (3.23) to (3.27) by deriving the mapping

$${}_{S_1}\mathbf{X}_S: {}^S\Delta_{E,S} \mapsto {}_{S_1}\Delta_{S_2,S_1}. \quad (3.28)$$

3.3.3 Wrenches resulting from small displacements

For very small displacements and rotations we have that $\mathbf{H} \approx \mathbf{I}_4 + \Delta^\wedge$, where $\mathbf{H} = {}^{S_2}\mathbf{H}_{S_1}$ and $\Delta = {}_{S_1}\Delta_{S_2,S_1}$ is a small twist displacement [24, 28]. This can be divided in a rotation and translation part, such that we have $\mathbf{o} \approx \Delta^\circ$ and $\mathbf{R} \approx \mathbf{I}_3 + \Delta^{\mathbf{R}\wedge}$. Substitution of these in (3.24), and by using that $\Delta^{\mathbf{R}\wedge} \in \mathfrak{so}(3)$ and $\Delta^{\mathbf{R}\wedge} \Delta^\circ \approx \mathbf{0}_{3 \times 1}$, results in

$${}_{S_1}\mathbf{f}_{L_1 \rightarrow L_2, spring} = \frac{1}{4} \begin{bmatrix} -\Delta^{\mathbf{R}\wedge} + 2\mathbf{I}_3 & \mathbf{0}_{3 \times 3} \\ -\Delta^{\mathbf{o}\wedge} & 2\mathbf{I}_3 - \Delta^{\mathbf{R}\wedge} \end{bmatrix} \mathbf{K} \begin{bmatrix} 2\Delta^\circ \\ 2\Delta^{\mathbf{R}} \end{bmatrix}. \quad (3.29)$$

Now, again by using $\Delta^{\mathbf{R}\wedge} \Delta^\circ \approx \mathbf{0}_{3 \times 1}$, $\Delta^{\mathbf{o}\wedge} \Delta^\circ \approx \mathbf{0}_{3 \times 1}$, and $\Delta^{\mathbf{R}\wedge} \Delta^{\mathbf{R}} \approx \mathbf{0}_{3 \times 1}$, (3.29) can be written as

$${}_{S_1}\mathbf{f}_{L_1 \rightarrow L_2, spring} = \frac{1}{4} \begin{bmatrix} 2\mathbf{I}_3 & \mathbf{0}_{3 \times 3} \\ \mathbf{0}_{3 \times 3} & 2\mathbf{I}_3 \end{bmatrix} \mathbf{K} \begin{bmatrix} 2\Delta^\circ \\ 2\Delta^{\mathbf{R}} \end{bmatrix}, \quad (3.30)$$

$$= \mathbf{K} \begin{bmatrix} \Delta^\circ \\ \Delta^{\mathbf{R}} \end{bmatrix}. \quad (3.31)$$

This confirms that \mathbf{K} determines the stiffness for ${}^A\mathbf{H}_{S_1} = {}^A\mathbf{H}_{S_2}$. In other words, \mathbf{K} can be chosen as a conventional stiffness matrix, for example as in classic beam theory [25].

3.4 Modeling of damping

To model the damping of the bellows suction cup, a coupled translational-angular linear damper will be modeled. This damper will be positioned at the same place as the coupled linear-torsional spring, between frames S_1 and S_2 , as in Figure 3.5a. The damping wrench, working on frame S_1 , can be written as

$${}_{S_1}\mathbf{f}_{L_2 \rightarrow L_1, damper} = -{}_{S_1}\mathbf{D}_{S_1} {}^{S_1}\mathbf{v}_{S_2,S_1}, \quad (3.32)$$

where

$${}_{S_1}\mathbf{D}_{S_1} := \frac{1}{2} \left(\mathbf{P} + {}_{S_1}\mathbf{X}^{S_2} \mathbf{P} {}_{S_2}\mathbf{X}_{S_1} \right). \quad (3.33)$$

In here, matrix \mathbf{P} is a positive (semi-)definite matrix that contains the damping coefficient times $\frac{1}{2}$. A more detailed explanation on writing damping matrix ${}_{S_1}\mathbf{D}_{S_1}$ as a parameterization of the positive (semi-)definite matrix \mathbf{P} is presented in Appendix D. For simulation and parameter identification purposes, we need to write the wrench such that it acts from the suction cup on the package at frame S . Therefore, we rewrite (3.32) by using the wrench transformation ${}_S\mathbf{X}^{S_1}$ and

$${}_{S_1}\mathbf{v}_{S_2,S_1} = {}_{S_1}\mathbf{X}_S^S \mathbf{v}_{E,S}, \quad (3.34)$$

of which the derivation can be found in Appendix E, into

$${}_S\mathbf{f}_{SC \rightarrow Pa, damper} = -{}_S\mathbf{D}_S^S \mathbf{v}_{E,S}, \quad (3.35)$$

where

$${}_S\mathbf{D}_S := \frac{1}{2} {}_S\mathbf{X}^{S_1} \left(\mathbf{P} + {}_{S_1}\mathbf{X}^{S_2} \mathbf{P} {}_{S_2}\mathbf{X}_{S_1} \right) {}_{S_1}\mathbf{X}_S \quad (3.36)$$

$$= \frac{1}{2} \left({}_S\mathbf{X}^{S_1} \mathbf{P} {}_{S_1}\mathbf{X}_S + {}_S\mathbf{X}^{S_2} \mathbf{P} {}_{S_2}\mathbf{X}_S \right). \quad (3.37)$$

The passivity of the damping wrench is elaborated upon in Appendix D.1. In short, the power injected by the damper can be written as

$$\left\langle {}_{S_1}\mathbf{f}_{L_2 \rightarrow L_1, damper}, {}_{S_1}\mathbf{v}_{S_2,S_1} \right\rangle = - \left({}_{S_1}\mathbf{D}_{S_1} {}_{S_1}\mathbf{v}_{S_2,S_1} \right)^T {}_{S_1}\mathbf{v}_{S_2,S_1}, \quad (3.38)$$

which will be negative when ${}_{S_1}\mathbf{D}_{S_1} \geq 0$, trivially when $\mathbf{P} \geq 0$.

3.5 Numerical implementation and validation

In this section, the implementation of the forward dynamics in MATLAB is discussed. This implementation enables us to simulate the package pose and the deformation of the bellows suction cup as a function of time. The model we want to simulate is

$$\mathbb{M}\dot{\mathbf{v}} + \mathbf{v} \bar{\mathbf{x}}^* \mathbb{M} \mathbf{v} = \mathbf{f}_{SC \rightarrow Pa} \left(\mathbf{K}, {}^E\mathbf{H}_S, \mathbf{D}, {}^S\mathbf{v}_{E,S} \right) + \mathbf{f}_g(\mathbf{H}), \quad (3.39)$$

where we used the short-hand notation $\mathbb{M} = {}_B\mathbb{M}_B$, $\mathbf{v} = \begin{bmatrix} \mathbf{v} \\ \boldsymbol{\omega} \end{bmatrix} = {}_B\mathbf{v}_{A,B} = \begin{bmatrix} {}_B\mathbf{v}_{A,B} \\ {}_B\boldsymbol{\omega}_{A,B} \end{bmatrix}$, $\mathbf{f}_g(\mathbf{H}) = {}_B\mathbf{f}_g({}^A\mathbf{H}_B)$, and

$$\mathbf{f}_{SC \rightarrow Pa} \left(\mathbf{K}, {}^E\mathbf{H}_S, \mathbf{D}, {}^S\mathbf{v}_{E,S} \right) = {}_B\mathbf{X}^S \left({}_S\mathbf{f}_{SC \rightarrow Pa, spring} \left(\mathbf{K}, {}^E\mathbf{H}_S \right) + {}_S\mathbf{f}_{SC \rightarrow Pa, damper} \left(\mathbf{D}, {}^S\mathbf{v}_{E,S} \right) \right).$$

To simulate this system using MATLAB, we write (3.39) as a set of first-order differential equations. Doing so, we take \mathbf{o} , \mathbf{R} , and \mathbf{v} as the states we want to simulate, which gives the following set of first-order differential equations:

$$\frac{d}{dt} \mathbf{o} = \dot{\mathbf{o}} = \mathbf{R} \mathbf{v}, \quad (3.40)$$

$$\frac{d}{dt} \mathbf{R} = \dot{\mathbf{R}} = \mathbf{R} \boldsymbol{\omega}^\wedge, \quad (3.41)$$

$$\frac{d}{dt} \mathbf{v} = \dot{\mathbf{v}} = \mathbb{M}^{-1} \left(-\mathbf{v} \bar{\mathbf{x}}^* \mathbb{M} \mathbf{v} + \mathbf{f}_{SC \rightarrow Pa} \left(\mathbf{K}, {}^E\mathbf{H}_S, \mathbf{D}, {}^S\mathbf{v}_{E,S} \right) + \mathbf{f}_g(\mathbf{H}) \right). \quad (3.42)$$

The input for the simulation is the pose and velocity data of the tool-arm frame, ${}^A\mathbf{H}_E$ and ${}^A\mathbf{v}_{E,A}$, respectively. The variable-step ODE-solvers of MATLAB are more accurate compared to the fixed-step solvers. Therefore, a variable-step ODE-solver solver is used to simulate the system. Because of the usage of a variable-step ODE solver, it is necessary to interpolate the inputted pose and velocity data of the tooling arm online, as the time integration step of the ODE-solver will probably be smaller than the sampling time of the input data. All though higher-order interpolation gives the most accurate interpolation result, the interpolation is performed in a linear fashion. This is because linear interpolation needs much less computational effort. Hence, linear interpolation will be much faster. The usage of linear interpolation is possible, because of the high sampling frequency of the input data, 360 Hz. The short sample time makes it possible to interpolate linearly without having large errors in the approximated pose and velocity of the tooling arm. Another option would be using spline interpolation. For spline interpolation, a low-degree polynomial is fitted for each data interval such that the polynomials pieces fit to each other. This spline interpolation is faster compared to higher-order interpolation, but still slower compared to linear interpolation.

The linear interpolation of the tool arm velocity, ${}^A\mathbf{v}_{E,A}$, can directly be performed without any problems, which is also the case for the position data, ${}^A\mathbf{o}_E$. This is however not the case for the orientation data. The interpolation of the orientation data is performed on the logarithmic mapping of ${}^A\mathbf{R}_E$, which is in $\mathfrak{so}(3)$. The result of this interpolation on $\mathfrak{so}(3)$ data is written back into a rotation matrix by using the exponential mapping, such that we have an interpolated rotation matrix as an element of $\text{SO}(3)$.

Validation

To examine whether the simulation code provides the correct forward dynamics results, several validating simulations can be performed. Two of these are presented below. Both validations are quantitative checks on the energy in the system. Hereby we consider the elastic potential energy of the bellows suction cup, P_0 , as in (3.17). The kinetic energy of the package is given by

$$E_{kin} = \frac{1}{2} {}^B\mathbf{v}_{A,B}^T {}^B\mathbb{M}_B {}^B\mathbf{v}_{A,B}, \quad (3.43)$$

and the gravitational energy is given by

$$E_g = m g \left({}^A\mathbf{o}_B \right)_z. \quad (3.44)$$

The two validating checks on the simulation are performed by keeping the tool-arm in a fixed pose, where ${}^A\mathbf{o}_E \neq \mathbf{0}_{3 \times 1}$ and ${}^A\mathbf{R}_E \neq \mathbf{I}_3$. Doing so, we use an initial pose of the package, which is not the static equilibrium pose. In this way the package will start to oscillate in all directions, depending on the chosen initial conditions.

The system parameters and initial conditions used for the validating simulations are as follows. The used system stiffness and damping matrices are:

$$\mathbf{K} = \begin{bmatrix} 200 & 10 & 30 & 3.2 & 2 & 1.3 \\ 10 & 180 & 20 & 0.7 & 4.3 & 2.5 \\ 30 & 20 & 1.55 \cdot 10^3 & 1 & 0.9 & 3.5 \\ 3.2 & 0.7 & 1 & 2 & 0.8 & 1 \\ 2 & 4.3 & 0.9 & 0.8 & 3 & 0.5 \\ 1.3 & 2.5 & 3.5 & 1 & 0.5 & 4 \end{bmatrix}, \quad (3.45)$$

$$\mathbf{P} = \begin{bmatrix} 2.5 & 0.5 & 1.5 & 0.34 & 0.025 & 0.004 \\ 0.5 & 2 & 1.5 & 0.2 & 0.07 & 0.15 \\ 1.5 & 1.5 & 4 & 0.2 & 0.08 & 0.1 \\ 0.34 & 0.2 & 0.2 & 0.25 & 0.1 & 0.08 \\ 0.025 & 0.07 & 0.08 & 0.1 & 0.3 & 0.05 \\ 0.004 & 0.15 & 0.1 & 0.08 & 0.05 & 0.4 \end{bmatrix}. \quad (3.46)$$

The stiffness and damping matrices are chosen manually, such that the simulated deformation does not become too large. Choosing a too low stiffness could cause the suction cup lip to rotate more than π radians, which would cause numerical problems. Note that both matrices are symmetric and positive definite. Furthermore, the nominal length of the bellows suction cup is chosen as 0.0482m, such that $l_1 = l_2 = 0.0241$ m. The simulations are performed for a box with a mass of 2 kg and a size $0.2 \times 0.2 \times 0.2$ m, which corresponds to the inertia matrix

$${}^B\mathbb{M}_B = \begin{bmatrix} 2 & 0 & 0 & 0 & 0 & 0 \\ 0 & 2 & 0 & 0 & 0 & 0 \\ 0 & 0 & 2 & 0 & 0 & 0 \\ 0 & 0 & 0 & 0.0133 & 0 & 0 \\ 0 & 0 & 0 & 0 & 0.0133 & 0 \\ 0 & 0 & 0 & 0 & 0 & 0.0133 \end{bmatrix}. \quad (3.47)$$

The initial pose of the package with respect to the absolute frame is

$${}^A\mathbf{H}_B = \begin{bmatrix} 0.5956 & -0.1185 & 0.7945 & -0.2004 \\ -0.1408 & 0.9584 & 0.2485 & 0.2661 \\ -0.7909 & -0.2598 & 0.5541 & 0.0301 \\ 0 & 0 & 0 & 1 \end{bmatrix}. \quad (3.48)$$

The initial velocity of the package is ${}^B\mathbf{v}_{A,B} = \mathbf{0}_{6 \times 1}$. Furthermore, the fixed pose of the tooling arm is

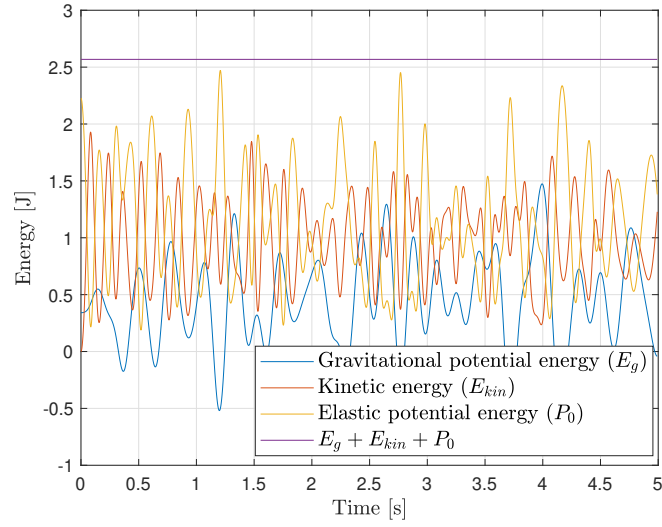
$${}^A\mathbf{H}_E = \begin{bmatrix} 0.9865 & -0.1459 & 0.0743 & -0.2000 \\ 0.1307 & 0.9751 & 0.1789 & 0.3000 \\ -0.0986 & -0.1668 & 0.9811 & 0.1800 \\ 0 & 0 & 0 & 1 \end{bmatrix}. \quad (3.49)$$

First, the simulation is performed without the damping model, so there is no energy dissipating and thus it should be that

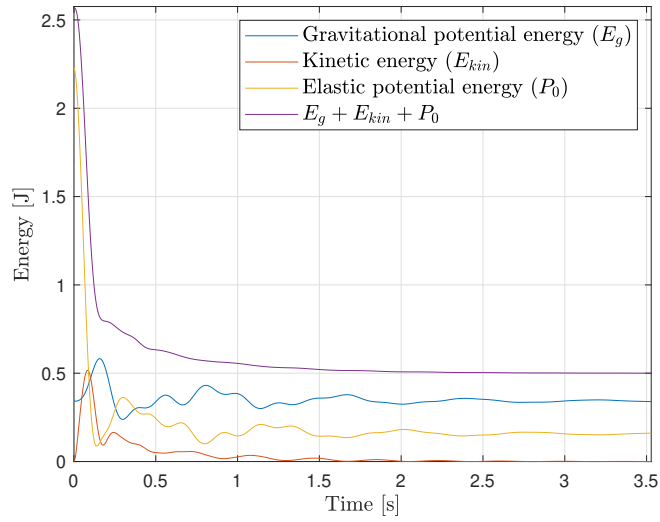
$$E_{kin} + P_0 + E_g = \text{constant}. \quad (3.50)$$

Figure 3.6a shows the resulting energies of such simulation. Herein can be seen that (3.50) is indeed true.

The second validating simulation is the same as the first validating simulation, but this time the damping is included. The result, in terms of energy, can be seen in Figure 3.6b. Here can be seen that the total amount of energy is always decreasing and approaches $P_0 + E_g$ for the static equilibrium pose. That the total amount of energy is decreasing at all times does agree with the expected outcome. The presence of damping in the system means that there is dissipating energy continuously when the bellows suction cup deforms.



(a)



(b)

Figure 3.6: Both figures represent the kinetic energy, the elastic potential energy, the gravitational energy, and the sum of those energies. Figure (a) shows the resulting energies when the damping is excluded. Figure (b) shows the resulting energies when the damping is included.

Chapter 4

Experimental data collection and parameter identification

This chapter is dedicated to the model parameter identification experiments and the way of processing the obtained data. First, in Section 4.1, the measurement procedure and the processing of the raw motion capture data are discussed. Hereafter, the results of the static measurements are presented. These static measurements are performed to identify the nominal length of the bellows suction cup during the holding phase, as elaborated upon in Section 3.2 and shown in Figure 3.4a. Last, the identification procedure and the obtained values for the stiffness and damping matrices are presented in Section 4.3. The obtained stiffness matrix corresponds to \mathbf{K} as in spring potential energy function (3.17) and its derived spring wrench (3.27). The obtained damping matrix corresponds to \mathbf{P} as in (3.33). Also presented in this section are the validating simulation results, which are compared to the measurement data.

4.1 Measurement procedure and data pre-processing

This section provides an overview of the measurement procedure and data pre-processing, to clarify which data has been used for the parameter identification. Furthermore, this elaboration can be used when carrying out more experiments for further research.

First, a brief elaboration upon the used measurement setup is presented. Figure 4.1 shows the measurement setup and its components. The OptiTrack cameras are used to track the markers

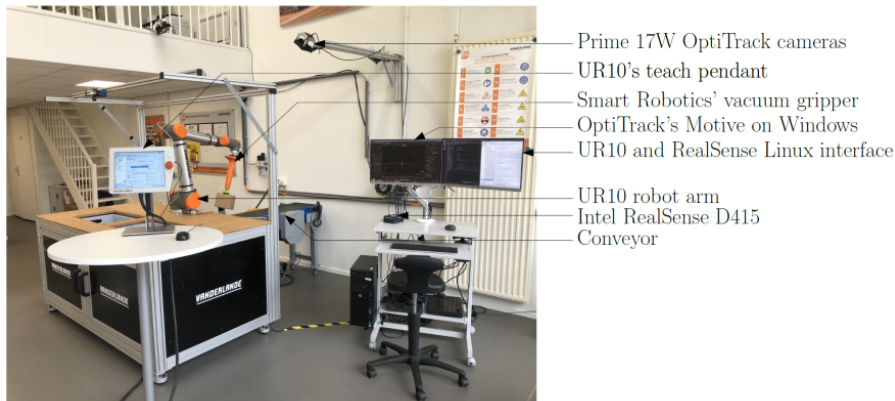


Figure 4.1: The measurement setup with all its components indicated [7].

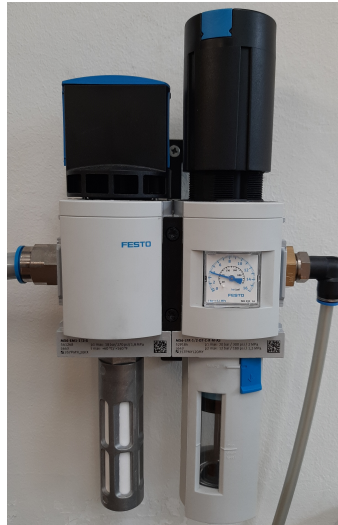


Figure 4.2: The flow regulator that is used to regulate the primary flow to the ejector in that is placed in the gripper. The flow regulator is tuned to 4 bar.

which are placed on the gripper, suction cup lip, package, or other objects of which the pose needs to be tracked. The data from the OptiTrack cameras is processed in Motive. Motive is the software that processes the camera data into position data of the markers in the 3D space. In Motive, it is possible to assign several markers to a rigid body, for example the box, the suction cup lip, or the tool-arm. This makes it possible to obtain the pose data of these rigid bodies from Motive. Furthermore, the measurement setup consists a RealSense camera. This camera is used to film the experiments such that it is possible to watch what happened during the measurements afterward. Although it is also possible to program the movements of the UR10 robot via Python on a Linux interface, the movements of the robot arm are programmed using the UR10 its teach pendant. Herein, the position of individual motors of the UR10 can be set, as well as the pose of the end-effector of the UR10. Figure 4.1 shows the measurement setup as it was at the start of this project. During the project, the measurement setup has been changed a bit, however, the different components are still the same. The important difference is the new positioning of the OptiTrack cameras and the addition of one Prime^X 22 OptiTrack camera. Changing the camera positioning and adding one more camera did lead to better object tracking. Not indicated in Figure 4.1 is the flow regulator used to regulate the primary airflow, also called the motive flow (not related to the Motive software), to the ejector that creates the (partial) vacuum within the gripper. This airflow regulator is shown in Figure 4.2. For all experiments performed for this report holds that they are carried out for a primary flow with a pressure of 4 bar (measured at the flow regulator). The measurement data that will be saved and stored in a data base contains: the OptiTrack data, the Intel RealSense camera data, the UR10 data (including the data of the pressure sensor in the gripper), and a YAML-file which contains the measurements specifications. More information about the measurement setup can be found in [7].

4.1.1 Measurement procedure

When executing the measurements using the OptiTrack system, the frame associated with the tip of the tooling arm and the frame at the suction cup lip, E_M and S_M , respectively, are both tracked with respect to the Motive calibration frame M . Frame S_M is tracked by using a plastic plate with markers, as shown in Figure 5.2. This is because the markers on the side of the plastic plate are much better visible for the OptiTrack cameras compared to the markers placed on the suction cup lip itself. This results in fewer frame drops in the measurement data.

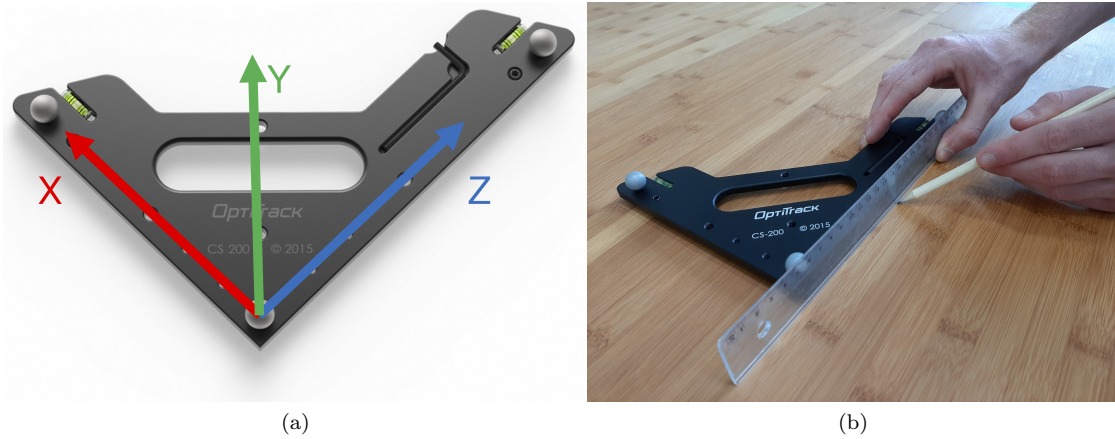


Figure 4.3: In this figure, the Ground Plane Calibration Square is shown, where Figure (a) shows the used Ground Plane Calibration Square with the corresponding axes assigned by Motive [49] and Figure (b) illustrates the line drawn along the \mathbf{z}_M axes.

Next, the measurement procedure is presented. It might not directly be evident why some steps in the measurement procedure are taken, but this will become clear in post-processing of the data in Section 4.1.2. In the post-processing, the orientation data of the suction cup lip and the tooling arm are manipulated to make sure that ${}^E\mathbf{R}_S = \mathbf{I}_3$ for the tooling arm being held in a vertical orientation. With a vertical orientation of the tooling arm, it is meant that the tooling arm points perpendicular to the earth surface such that \mathbf{z}_A and \mathbf{z}_E point in the exact same direction. The property ${}^E\mathbf{R}_S = \mathbf{I}_3$ when the gripper is held in a vertical orientation is desired, because it would mean that there is no moment working from the suction cup on the package in static equilibrium (${}^S\boldsymbol{\tau}_{SC \rightarrow Pa} = \mathbf{0}_{3 \times 1}$).

For all measurements the following procedure is followed:

1. The procedure starts with the calibration of the OptiTrack system. First, the ground plane is leveled by using the spirit levels incorporated in the Ground Plane Calibration Square provided with the OptiTrack system, as shown in Figure 4.3a. Before setting the ground plane in Motive (frame M), the \mathbf{z}_M -axis is drawn on the surface on which the Ground Plane Calibration Square rests, as shown in Figure 4.3b. This surface is a sheet of wood, which lies on the conveyor to protect the conveyor from being damaged by the unwanted impact of the plastic plate with the attached weights when the plastic plate is released unintentionally. Because of the drawn line on the sheet of wood, the sheet of wood may not move between the calibration and measurements or during the measurements. If the sheet of wood would be moved, then the drawn \mathbf{z}_M axes would not align anymore to the calibration frame M in Motive. This would mean that a new ground plane M should be set in Motive by redoing the calibration.
2. Next, the plastic plate is placed on the drawn \mathbf{z}_M -axis line, such that the frame fixed to the plastic plate is aligned with the \mathbf{z}_M -axis, as shown in Figure 4.4. This step is not necessarily essential, since that the orientation of the plastic plate is also known from Motive, but makes the post-processing of the data easier.
3. The following step is to pick up the plastic plate with the gripper. Doing so, the tooling arm is placed vertically, so \mathbf{z}_E and \mathbf{z}_A point in the same direction. This is done by using the robot command window of the UR10 teach pedant, as indicated in Figure 4.1, in which the desired pose of the tool center point (TCP) can be given as an input. By placing the tool-arm in a vertical orientation, the assumption is made that the robot bench is exactly leveled. The

positioning of the gripper in vertical orientation is used in the post-processing and for the static measurement, which is elaborated upon in Sections 4.1.2 and 4.2, respectively.

4. Once the gripper has picked up the plastic plate, the robot arm can move to the first pose point of the measurement routine. By making this movement, only the position of the TCP is changed, so the orientation is kept vertically, as in the previous step. When the robot is moved to the starting position of the trajectory, which is always a vertical orientation for the tooling arm, the weights can be attached to the plastic plate. The weights are placed symmetrically with respect to the bellows suction cup to prevent it from bending when the tooling arm is held in starting pose, and thus to make sure that ${}^E\mathbf{R}_S = \mathbf{I}_3$ at the start of the measurement recording. Here is elaborated upon in Section 4.1.2.
5. The last step is the measurement recording itself. Every recording starts with a short period, 1 or 2 seconds, where the tooling arm stands still in a vertical orientation, followed by the programmed robot path. The data of the short period before the movements will be used to process the measurement data such that there is no lateral and rotational offset between frame S and frame E during the starting pose (gripper standing still in a vertical orientation while holding the plate). This data processing is elaborated upon in the next section.

4.1.2 Rotational and lateral offset compensation

From Motive, we have the tooling arm and the suction cup lip pose data, ${}^M\mathbf{H}_{S_M}$ and ${}^M\mathbf{H}_{E_M}$, respectively. Figure 4.5 shows the pose of the suction cup lip with respect to the tip of the tooling arm, written in the frames as assigned in Motive. Even without knowing the exact frame definition of frames E_M and S_M , the following should be considered when processing the data from E_M and S_M to E and S . Note that the frames E_M and S_M are the frames associated with the tip of the tooling arm and the suction cup lip, as defined in Motive. Frames E and S are the frames associated with the tip of the tooling arm and the suction cup lip, as defined in this report (see Figure 3.1).

Because of the axial symmetry of the bellows suction cup, it is assumed that $({}^E\mathbf{o}_S)_x = ({}^E\mathbf{o}_S)_y = 0$ when the gripper is held vertically. This means that, when the gripper is held in the starting pose (tooling arm pointing perpendicular to the earth), there should be no lateral spring force working on the package, $(s\mathbf{f}_{SC \rightarrow PA})_x = (s\mathbf{f}_{SC \rightarrow PA})_y = 0$. From the upper plot of Figure 4.5, where the blue and orange lines show the lateral displacement of frame S_M with respect to frame E_M , it can be seen that there is a small (around 1mm) lateral displacement offset. The lateral displacement offset is the result of the misalignment during the placing of the suction cup on the plastic plate. This means that we picked up the plastic plate with a lateral offset and have therefore $({}^E\mathbf{o}_S)_x \neq 0$ and $({}^E\mathbf{o}_S)_y \neq 0$. According to our spring model, this means that lateral spring forces

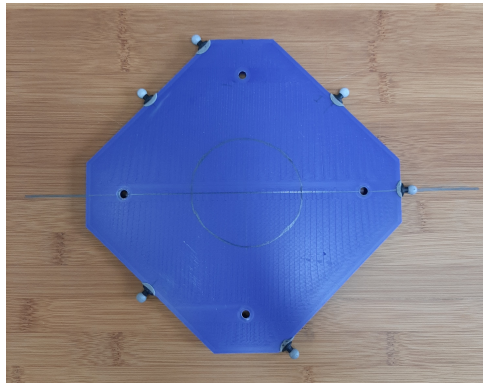


Figure 4.4: The placement of the plastic plate on the drawn \mathbf{z}_M -axis.

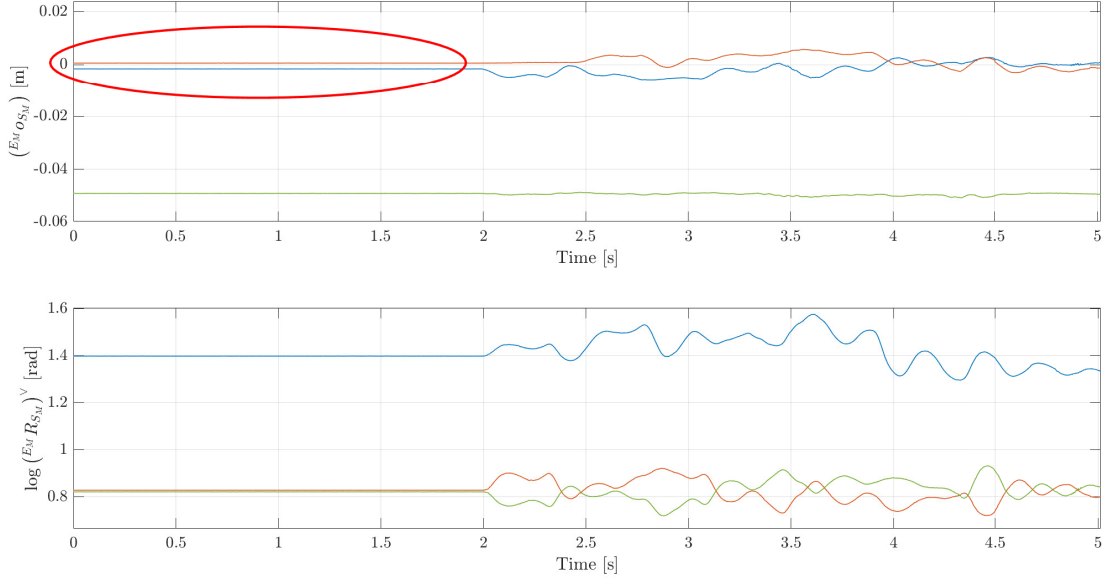


Figure 4.5: The pose data of the suction cup lip with respect to the tip of the tooling arm, written in the frames as defined in Motive.

are acting on the package when the gripper is held in starting pose, $({}^S \mathbf{f}_{SC \rightarrow Pa, spring})_x \neq 0$ and $({}^S \mathbf{f}_{SC \rightarrow Pa, spring})_y \neq 0$. These lateral forces do not make sense when considering the axial symmetry of the bellows suction cup and could be problematic for the stiffness identification. Therefore, it is necessary to manipulate the data, to ensure that $({}^E \mathbf{o}_S)_x = ({}^E \mathbf{o}_S)_y = 0$. In summary, when picking up the plastic plate with the gripper, we have that $({}^E \mathbf{o}_S)_x \neq 0$ and $({}^E \mathbf{o}_S)_y \neq 0$ due to the misalignment of the suction cup lip on the plastic plate. Because the misalignment is small (around 1mm), we manipulate the data such that we have $({}^E \mathbf{o}_S)_x = ({}^E \mathbf{o}_S)_y = 0$ for the starting pose. Doing this manipulation, we also assume that $({}^S \mathbf{f}_{SC \rightarrow PA, spring})_x = ({}^S \mathbf{f}_{SC \rightarrow PA, spring})_y = 0$ for the starting pose.

The second point of attention is that for the orientation of the suction cup lip with respect to the tip of the tooling arm we desire that ${}^E \mathbf{R}_S = \mathbf{I}_3$ for the starting pose. This gives rise to a similar issue as for the lateral offset. If it would be that ${}^E \mathbf{R}_S \neq \mathbf{I}_3$, then there would be acting moments on the package coming from the suction cup as a result of the modeled rotational stiffness, ${}^S \boldsymbol{\tau}_{SC \rightarrow PA, spring} \neq \mathbf{0}_{3 \times 1}$. Again, because of the axial symmetry of the bellows suction cup, this would not make sense. So, when going from frames as defined in Motive to the frame definition as used in this report, we need to keep in mind that we want ${}^E \mathbf{R}_S = \mathbf{I}_3$ for the starting pose. Again, the purpose of this manipulation of the data is to ensure that the data can be used for the parameter identification.

In this section, we use $t(t_0)$ to indicate ‘at the starting pose’, which means a vertical orientation of the gripper which holds the plastic plate and the rigidly attached weights. As explained above, we want to pre-process the data such that we have ${}^E \mathbf{R}_S = \mathbf{I}_3$ and $({}^E \mathbf{o}_S)_x = ({}^E \mathbf{o}_S)_y = 0$ at the starting pose, so that ${}^{E(t_0)} \mathbf{R}_{S(t_0)} = \mathbf{I}_3$ and $({}^{E(t_0)} \mathbf{o}_{S(t_0)})_x = ({}^{E(t_0)} \mathbf{o}_{S(t_0)})_y = 0$. Therefore, we perform the following steps:

1. First, frame A , which is the absolute world frame as used in this report (see Figure 3.1), is defined from frame M . This is done for the ${}^M \mathbf{H}_{S_M}$ and ${}^M \mathbf{H}_{E_M}$ data. For the pose data of

the tip of the tooling arm, this can be done by

$${}^A\mathbf{H}_{E_M}(t_k) = {}^A\mathbf{H}_M {}^M\mathbf{H}_{E_M}(t_k) = \begin{bmatrix} -1 & 0 & 0 & 0 \\ 0 & 0 & 1 & 0 \\ 0 & 1 & 0 & 0 \\ 0 & 0 & 0 & 1 \end{bmatrix} {}^M\mathbf{H}_{E_M}(t_k), \quad (4.1)$$

where $k \in \{1, \dots, N\}$ and N is the number of data points. This can be done in a similar way for the suction cup lip pose data.

2. Next, we want to calculate the offset between frames E_M and S_M in the lateral displacement directions and the orientation. The calculation of these offsets is done in the following steps:

- (a) We define ${}^A\mathbf{H}_{E_M(t_0)[E(t_0)]}$ and ${}^A\mathbf{H}_{S_M(t_0)[S(t_0)]}$, where $E_M(t_0)[E(t_0)] = \left(\mathbf{o}_{E_M(t_0)}, [E(t_0)] \right)$.

Note that frame $E_M(t_0)$ is the frame at the tip of the tooling arm as defined in Motive, and frame $E(t_0)$ is the frame at the tip of the tooling arm as used in this report, both for the starting pose of the tool-arm. For the orientation of the tooling arm and the suction cup lip in starting pose, we define ${}^A\mathbf{R}_{E(t_0)} = {}^A\mathbf{R}_{S(t_0)} = \mathbf{I}_3$. The reason for this is that by choosing ${}^A\mathbf{R}_{E(t_0)} = {}^A\mathbf{R}_{S(t_0)}$, we also have that ${}^{E(t_0)}\mathbf{R}_{S(t_0)} = \mathbf{I}_3$, which is, as explained before, desirable for the parameter identification. Furthermore, choosing ${}^A\mathbf{R}_{S(t_0)} = \mathbf{I}_3$ is more of a practical choice to simplify things. The way that the plastic plate is aligned with the Motive ground plane M (and equivalently aligned with the absolute world frame A), as described in Step 2 of Section 4.1.1, enables us to have ${}^A\mathbf{R}_{B(t_0)} = \mathbf{I}_3$. This also means that ${}^S\mathbf{R}_B = \mathbf{I}_3$, which simplifies things a bit. So, writing ${}^A\mathbf{H}_{E_M(t_0)[E(t_0)]}$ and ${}^A\mathbf{H}_{S_M(t_0)[S(t_0)]}$ gives us

$${}^A\mathbf{H}_{E_M(t_0)[E(t_0)]} = \begin{bmatrix} \mathbf{I}_3 & {}^A\mathbf{o}_{E_M(t_0)} \\ \mathbf{0}_{1 \times 3} & 1 \end{bmatrix}, \quad (4.2)$$

$${}^A\mathbf{H}_{S_M(t_0)[S(t_0)]} = \begin{bmatrix} \mathbf{I}_3 & {}^A\mathbf{o}_{S_M(t_0)} \\ \mathbf{0}_{1 \times 3} & 1 \end{bmatrix}. \quad (4.3)$$

- (b) Next, the offset in the position and orientation of the suction cup with respect to the tip of the tooling arm is calculated. The rotation from the frames as defined in Motive to the frame definition as used in this report can be written as

$${}^{E_M(t_0)}\mathbf{H}_{E_M(t_0)[E(t_0)]} = {}^A\mathbf{H}_{E_M(t_0)}^{-1} {}^A\mathbf{H}_{E_M(t_0)[E(t_0)]} = \begin{bmatrix} {}^{E_M(t_0)}\mathbf{R}_{E(t_0)} & \mathbf{0}_{3 \times 1} \\ \mathbf{0}_{1 \times 3} & 1 \end{bmatrix}, \quad (4.4)$$

$${}^{S_M(t_0)}\mathbf{H}_{S_M(t_0)[S(t_0)]} = {}^A\mathbf{H}_{S_M(t_0)}^{-1} {}^A\mathbf{H}_{S_M(t_0)[S(t_0)]} = \begin{bmatrix} {}^{S_M(t_0)}\mathbf{R}_{S(t_0)} & \mathbf{0}_{3 \times 1} \\ \mathbf{0}_{1 \times 3} & 1 \end{bmatrix}. \quad (4.5)$$

The above obtained homogeneous transformation matrices can be used to rotate the pose data from Motive, E_M and S_M , to the frame definition as used in this report, E and S . Note that ${}^{E_M(t_0)}\mathbf{R}_{E_M(t_0)[E(t_0)]} \neq {}^{S_M(t_0)}\mathbf{R}_{S_M(t_0)[S(t_0)]}$. Next, the offset in lateral position is calculated by

$${}^{E_M(t_0)[E(t_0)]}\mathbf{H}_{S_M(t_0)[S(t_0)]} = {}^A\mathbf{H}_{E_M(t_0)[E(t_0)]}^{-1} {}^A\mathbf{H}_{S_M(t_0)[S(t_0)]} = \begin{bmatrix} \mathbf{I}_3 & {}^{E_M(t_0)}\mathbf{o}_{S_M(t_0)} \\ \mathbf{0}_{1 \times 3} & 1 \end{bmatrix}. \quad (4.6)$$

Ideally, it would be that $\left({}^{E_M(t_0)}\mathbf{o}_{S_M(t_0)} \right)_x = \left({}^{E_M(t_0)}\mathbf{o}_{S_M(t_0)} \right)_y = 0$. However, this is not the case, as shown in Figure 4.5. Therefore, there is a clear need to compensate for this such that $\left({}^{E(t_0)}\mathbf{o}_{S(t_0)} \right)_x = \left({}^{E(t_0)}\mathbf{o}_{S(t_0)} \right)_y = 0$.

3. The next step is to calculate the pose of the suction cup lip with respect to the tooling arm for every time step using the Motive data

$${}^E\mathbf{H}_{S_M}(t_k) = {}^A\mathbf{H}_{E_M}(t_k)^{-1} {}^A\mathbf{H}_{S_M}(t_k) \quad (4.7)$$

for $k \in \{1, \dots, N\}$.

4. Now we have (4.7), we can adjust this data. First, the rotational offset between E_M and S_M is eliminated by using (4.4) and (4.5) such that

$${}^{E_M[E]}\mathbf{H}_{S_M[S]}(t_k) = {}^{E_M(t_0)}\mathbf{H}_{E_M(t_0)[E(t_0)]}^{-1} {}^{E_M}\mathbf{H}_{S_M}(t_k) {}^{S_M(t_0)}\mathbf{H}_{S_M(t_0)[S(t_0)]}, \quad (4.8)$$

$$= \begin{bmatrix} {}^E\mathbf{R}_S(t_k) & {}^{E_M}\mathbf{o}_{S_M}(t_k) \\ \mathbf{0}_{1 \times 3} & 1 \end{bmatrix}, \quad (4.9)$$

for $k \in \{1, \dots, N\}$. Note that (4.8) is a slight abuse of notation, but remember that ${}^{E_M(t_0)}\mathbf{H}_{E_M(t_0)[E(t_0)]}$ and ${}^{S_M(t_0)}\mathbf{H}_{S_M(t_0)[S(t_0)]}$ are just the rotational transformations from the frame definitions as in Motive to the frame definitions as used in this report.

5. Next, the lateral displacement offset in ${}^{E_M[E]}\mathbf{H}_{S_M[S]}(t_k)$ will be compensated. This is done is done by

$${}^E\mathbf{o}_S(t_k) = {}^{E_M}\mathbf{o}_{S_M}(t_k) - \begin{bmatrix} \left({}^{E_M(t_0)}\mathbf{o}_{S_M(t_0)} \right)_x \\ \left({}^{E_M(t_0)}\mathbf{o}_{S_M(t_0)} \right)_y \\ 0 \end{bmatrix}, \quad (4.10)$$

such that we have

$${}^E\mathbf{H}_S(t_k) = \begin{bmatrix} {}^E\mathbf{R}_S(t_k) & {}^E\mathbf{o}_S(t_k) \\ \mathbf{0}_{1 \times 3} & 1 \end{bmatrix}. \quad (4.11)$$

for $k \in \{1, \dots, N\}$.

6. The last step is to obtain the pose data of the suction cup lip and the tooling arm (written in the frame definition as used in this report), both with respect to the absolute frame. For the tooling arm data we adjust the orientation by

$${}^A\mathbf{H}_E(t_k) = {}^A\mathbf{H}_{E_M}(t_k) {}^{E_M(t_0)}\mathbf{H}_{E_M(t_0)[E(t_0)]}. \quad (4.12)$$

Note that frames E and E_M have the same origin, but different orientations, as can be seen in (4.4). So the homogeneous transformation matrix ${}^{E_M(t_0)}\mathbf{H}_{E_M(t_0)[E(t_0)]}$ is effectively ${}^{E_M(t_0)}\mathbf{H}_{E(t_0)}$. For the suction cup lip pose data we compute

$${}^A\mathbf{H}_S(t_k) = {}^A\mathbf{H}_E(t_k) {}^E\mathbf{H}_S(t_k). \quad (4.13)$$

For (4.12) and (4.13) hold that they are both done for every time step, so $k \in \{1, \dots, N\}$. Important to note is that by using (4.13), as well the rotational correction as the correction for the lateral position is taken into consideration.

The result of the data adjustment is shown in Figure 4.6, where the processed pose data, ${}^E\mathbf{H}_S(t_k)$, is visualized. Looking at the starting pose, the first two seconds, it can be concluded that the lateral displacement offset is eliminated, $({}^E\mathbf{o}_S)_x = ({}^E\mathbf{o}_S)_y = 0$. This means that there will be no spring force acting on the package in the lateral direction when the gripper is held in the starting pose. Furthermore, it can be concluded that ${}^E\mathbf{R}_S = \mathbf{I}_3$ for the first two seconds. This means that there is also no moment acting on the package for the gripper being in the starting pose. This makes the pose data suitable for the parameter identification.

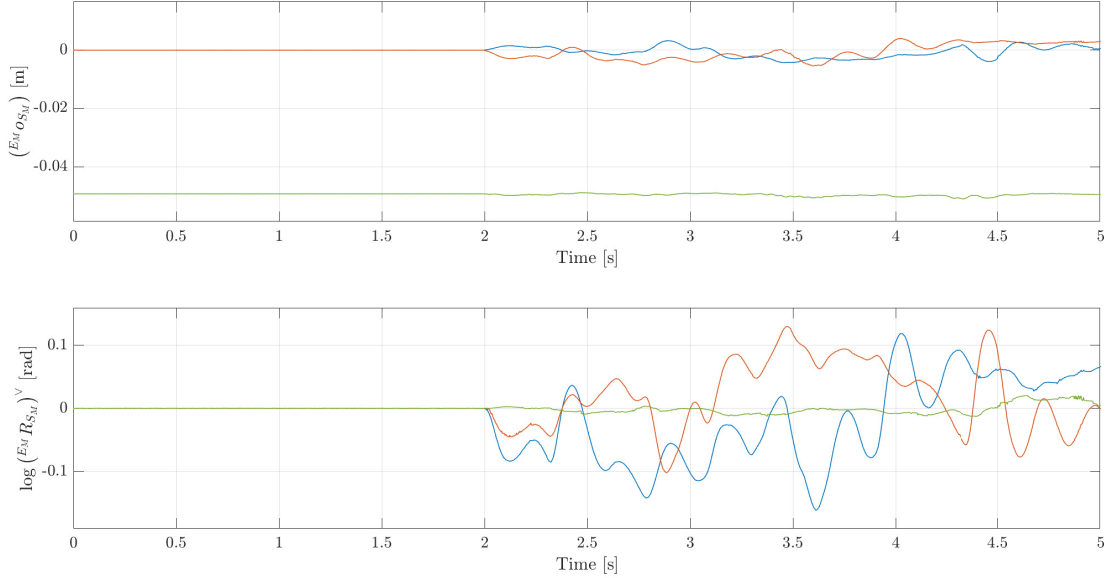


Figure 4.6: The resulting pose data of the suction cup lip with respect to the tip of the tooling arm, written in the frames as used in this report.

4.2 Nominal bellows suction cup length identification

One of the parameters which needs to be identified is the nominal length of the bellows suction cup during the holding phase, l_0 , as shown in Figure 4.7, and explained in Section 3.2. The identification of this parameter is done by performing static experiments. A schematic representation and a picture of these experiments are shown in Figures 4.8a and 4.8b, respectively. In Figure 4.8a can be seen that the length of the bellows suction cup, $({}^E \mathbf{o}_S)_z$, is measured for a given mass attached to the plastic plate. This is done while keeping the tooling arm in a vertical orientation, as explained in step 3 of Section 4.1.1. An important note is that the weights are placed (with hand-eye precision) symmetrically around the center of the bellows suction cup. This way, the frame fixed to the center of mass of the package, frame B (not drawn in Figure 4.8a), would align

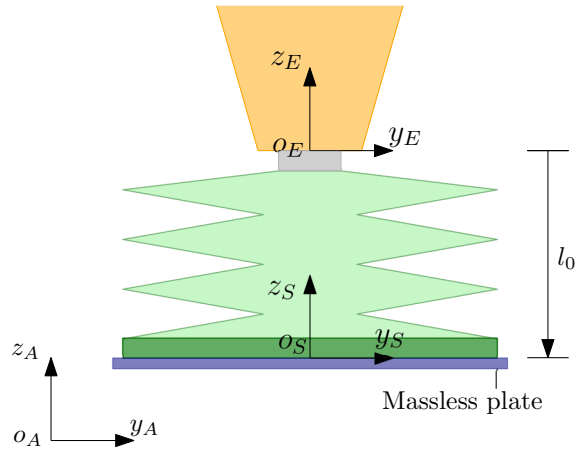


Figure 4.7: Nominal length bellows suction cup during holding phase.

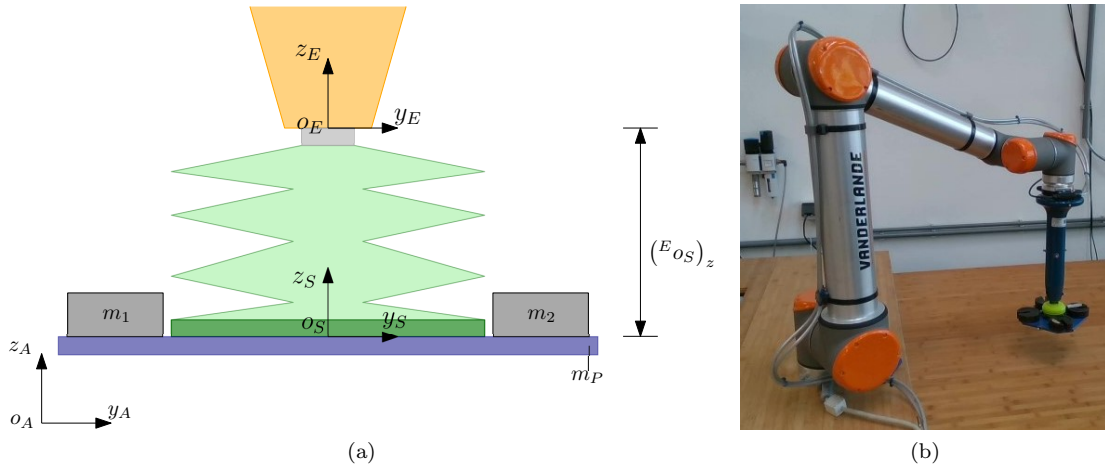


Figure 4.8: Figure (a) shows a schematic representation of the static measurements, used to identify the nominal length of the bellows suction cup. Here indicate m_1 and m_2 the masses of the weights and m_P indicates the mass of the plastic plate. Figure (b) is a picture of such static experiment.

with the \mathbf{z}_S -axis. This would mean that $[S] = [E]$ and thus also that axes \mathbf{z}_B and \mathbf{z}_S do align with \mathbf{z}_E . As a result of this, the deformation of the bellows suction cup is only in the $-\mathbf{z}_E$ direction when adding weights to the plastic plate. So, the bellows suction cup will only elongate and will not bend.

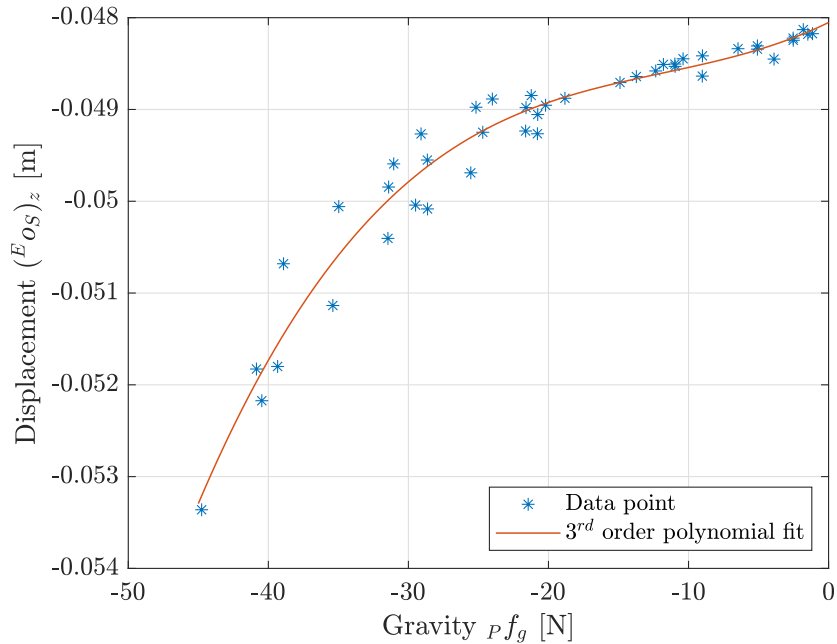


Figure 4.9: Results of the static measurements to identify the nominal length of the bellows suction cup during holding phase. On the x-axis is shown the gravity that acts on the plastic plate and weights.

The results of the static experiments are shown in Figure 4.9. Herein, the separate measurement points and a third-order polynomial fitted to these data points are visualized. The polynomial is fitted using the least-squares method. The third-order polynomial fit shows a linear relation between displacement and force for small deformations. This linear behavior means that the stiffness is constant in this region. For gravity larger than -20N , the non-linearity becomes visible. From this can be concluded that the bellows suction cup has a degressive spring characteristic. Furthermore, from the third-order polynomial fit in Figure 4.9 can be concluded that the nominal length of the bellows suction cup is -0.0481m . This is the length of the bellows suction cup when holding a massless package, which corresponds to 0N gravity in Figure 4.9.

As elaborated upon in Section 3.3.1, the bellows suction cup is modeled as two links connected via a coupled linear-torsional spring. The length of these links, l_1 and l_2 , are chosen evenly, such that $l_1 = l_2 = 0.02405\text{m}$. This means that the center of stiffness of the bellows suction cup is modeled at the middle of the suction cup. This choice is only valid when performing experiments for which the deformation stays in the linear region of the stiffness. So, this would be for experiments where the longitudinal load is between 0N and about -25N .

4.3 Stiffness and damping identification

To identify the stiffness and damping matrices, dynamic measurements are carried out. For these dynamic measurements, the gripper holds the plastic plate with rigidly attached weights. The total mass held by the gripper is 2.17kg , which corresponds to the linear region in Figure 4.9. The inertia tensor of the loaded plastic plate is

$${}_B\mathbb{M}_B = \begin{bmatrix} 2.17 & 0 & 0 & 0 & 0 & 0 \\ 0 & 2.17 & 0 & 0 & 0 & 0 \\ 0 & 0 & 2.17 & 0 & 0 & 0 \\ 0 & 0 & 0 & 0.0087 & 0 & 0 \\ 0 & 0 & 0 & 0 & 0.0087 & 0 \\ 0 & 0 & 0 & 0 & 0 & 0.0173 \end{bmatrix}. \quad (4.14)$$

The UR10 is programmed to make movements defined by arbitrarily chosen waypoints (positions and orientations defined for the UR10 end-effector). These waypoints are chosen such that the bellows suction cup deforms in many directions, which should give us a rich data set for the parameter identification. A better way would be making a trajectory for which we are sure that it would give a rich enough data set for the parameter identification. This was however not possible due to time limitations. To identify the stiffness and the damping of the bellows suction cup, the inverse dynamics of (3.5) will be used [50]. Usually, inverse dynamics is used to compute applied forces and torques that induce a measured or desired motion [51, 52]. In this project, the (internal) forces and torques are resulting from the stiffness and the damping of the bellows suction cup. The kinematic data we are using is the motion capture pose data and its estimated velocity and acceleration data. The known external force is the gravity acting on the package. When the stiffness and damping wrenches are reconstructed, by using inverse dynamics, the stiffness and damping matrices can be computed by using the measured pose data and the estimated velocity data of the suction cup lip with respect to the tool-arm.

The smoothing of the measured pose data and the estimation of the velocities and accelerations from the measured pose data is done by using a Savitzky-Golay filter, as presented in Section 4.3.1. Herein, it can be seen that the Savitzky-Golay filter will be used to smoothen the measured pose data with relatively small measurement errors. Furthermore, the motion capture data does contain some outliers with a large error. These outliers are the result of bad tracking of the markers stuck to the robot tooling arm or the plastic plate. In Appendix H, an elaboration upon the identification and exclusion of these outliers in/from the data set is presented. From this, we obtain smoothed pose data and the estimated velocity and acceleration data (which is achieved by using the Savitzky-Golay filter), which is free from outliers. This data will be used for the

identification of the stiffness and damping matrices. For this identification procedure, we use inverse dynamics and a weighted least-squares approach, as presented in Section 4.3.2. Also in this section, a validation of the obtained results is presented.

4.3.1 Estimation of linear and angular velocity and acceleration from $\text{SO}(3) \times \mathbb{R}^3$ data

To perform the parameter identification by using inverse dynamics, it is necessary to have approximations of the velocity and acceleration, see (4.65). One way of approximating these is by using the finite difference method. The result of the usage of the central difference method on measurement data can be found further in this section. The details about the central difference method on $\text{SO}(3) \times \mathbb{R}^3$ data are presented in Appendix F. In the figures presented later on, it can be seen that using the finite difference method results in very noisy approximations of the velocity and especially the acceleration. Because having accurate velocity and acceleration approximations is crucial for the parameter identification, the following method is proposed; a Savitzky-Golay filter on the pose data. A Savitzky-Golay filter uses a moving window average [53]. This averaging is done by fitting a polynomial to the data in the window. The window size and the order of the polynomial need to be tuned for a given data set. Choosing a larger window results in more averaging points and thus more noise reduction, however, one needs to keep in mind that choosing a too large window causes less accurate approximations. Choosing a higher-order polynomial to fit on the data within the window results in a better fit to the raw data, including the noise [54]. An alternative to the Savitzky-Golay filter would be using a low-pass filter in combination with the finite difference method. The similarity between a low-pass filter and a Savitzky-Golay filter is that both filters reduce high-frequency noise, but do not filter out the low-frequency noise. However, the advantage of using a Savitzky-Golay filter, and therefore the reason why this filter is used in this project, is that the time derivatives of the smoothed signal can directly be obtained from the fitted polynomial at each time step.

Applying a Savitzky-Golay filter to the position data, in \mathbb{R}^3 , is relatively straightforward. This is elaborated upon in the next part. However, for the orientation data, $\text{SO}(3)$ data, the Savitzky-Golay filtering is not that straightforward. In [55], a method for applying Savitzky-Golay filtering on $\text{SO}(3)$ motion capture data is presented. Herein, the first step is to obtain the Euler angles from the rotation matrix describing the orientation. Next, a Savitzky-Golay filter is applied to the three individual time-dependent Euler angles, where the last step is to convert these smoothed Euler angles back to a rotation matrix. Doing so, one ensures that $\mathbf{R} \in \text{SO}(3)$. However, this approach has the drawback that the smoothing of the first rotation has a larger influence on the smoothed orientation than the last rotation, because the orientation is described by three consecutive rotations [56]. Therefore, a method where a Savitzky-Golay filter is applied on the Lie algebra $\mathfrak{so}(3)$ is proposed, to smoothen the orientation data and estimate the angular velocity and acceleration. This method is developed within the Dynamics and Control section of TU/e Mechanical Engineering. This is elaborated upon after the part of the Savitzky-Golay filter on the position data. Finally, the results of the Savitzky-Golay filtering on the real measurement data are presented and compared to the central difference results.

Savitzky-Golay filtering on \mathbb{R}^3

As mentioned before, using Savitzky-Golay filtering is the fitting of polynomials to the data within a window for every time step. So, if we want to apply Savitzky-Golay filtering on the position data, we are effectively fitting polynomials on the position data for every time step. In this way, we have a n -order polynomial in \mathbb{R}^3 :

$$\mathbb{R}^3 \ni \boldsymbol{\xi}(t; \boldsymbol{\eta}) := \boldsymbol{\eta}_0 + \boldsymbol{\eta}_1 t + \frac{1}{2} \boldsymbol{\eta}_2 t^2 + \dots + \frac{1}{n!} \boldsymbol{\eta}_n t^n, \quad (4.15)$$

where $\boldsymbol{\eta} = [\boldsymbol{\eta}_0; \boldsymbol{\eta}_1; \boldsymbol{\eta}_2; \dots; \boldsymbol{\eta}_n]$ is a vector of parameters and n the order of the fitted polynomial. We can take the time derivatives of this polynomial and consider these functions at the discrete time indices $t_k = kT$, with $k \in \{1, \dots, N\}$, where N is the total number of discrete time indices and $T = 1/f_s$ is the time step. This gives us

$$\frac{d}{dt}\boldsymbol{\xi}(t_k, \boldsymbol{\eta}) = \boldsymbol{\eta}_1 + \boldsymbol{\eta}_2 t_k + \dots + \frac{1}{(n-1)!} \boldsymbol{\eta}_n t_k^{n-1}, \quad (4.16)$$

$$\frac{d^n}{dt^n}\boldsymbol{\xi}(t_k, \boldsymbol{\eta}) = \boldsymbol{\eta}_n. \quad (4.17)$$

On the measured position data $\mathbf{o}(t_k)$, obtained from the measurements, we consider a moving time window centered at t_k with the sampled points $t_w = t_k + wT$, where $w \in \{-n_w, \dots, -1, 0, 1, \dots, n_w\}$. Herein is n_w the number of data points on each side of the center of the window such that the size of the window is $2n_w + 1$. The least-squares problem is then defined by

$$\boldsymbol{\xi}^* = \arg \min_{\boldsymbol{\xi}} \sum_{w=-n_w}^{w=n_w} \|\mathbf{o}(t_w) - \boldsymbol{\xi}(t_w - t_k; \boldsymbol{\eta})\|^2. \quad (4.18)$$

The solution to this least-squares problem can be found by computing

$$\widehat{\boldsymbol{\eta}} = \left(\mathbf{A}_{SG}^T \mathbf{A}_{SG} \right)^{-1} \mathbf{A}_{SG}^T \mathbf{b}_{SG, \mathbf{o}} \in \mathbb{R}^{3n}, \quad (4.19)$$

where $\widehat{\boldsymbol{\eta}} = [\widehat{\boldsymbol{\eta}}_0; \widehat{\boldsymbol{\eta}}_1; \widehat{\boldsymbol{\eta}}_2; \dots; \widehat{\boldsymbol{\eta}}_n]$, in which $\widehat{(\cdot)}$ indicates ‘estimated’, and where

$$\mathbf{A}_{SG} = \begin{bmatrix} \mathbf{I}_3 & (t_{k-n_w} - t_k)\mathbf{I}_3 & \frac{1}{2}(t_{k-n_w} - t_k)^2\mathbf{I}_3 & \dots & \frac{1}{n!}(t_{k-n_w} - t_k)^n\mathbf{I}_3 \\ \dots & \dots & \dots & \dots & \dots \\ \mathbf{I}_3 & (t_{k-1} - t_k)\mathbf{I}_3 & \frac{1}{2}(t_{k-1} - t_k)^2\mathbf{I}_3 & \dots & \frac{1}{n!}(t_{k-1} - t_k)^n\mathbf{I}_3 \\ \mathbf{I}_3 & (t_k - t_k)\mathbf{I}_3 & \frac{1}{2}(t_k - t_k)^2\mathbf{I}_3 & \dots & \frac{1}{n!}(t_k - t_k)^n\mathbf{I}_3 \\ \mathbf{I}_3 & (t_{k+1} - t_k)\mathbf{I}_3 & \frac{1}{2}(t_{k+1} - t_k)^2\mathbf{I}_3 & \dots & \frac{1}{n!}(t_{k+1} - t_k)^n\mathbf{I}_3 \\ \dots & \dots & \dots & \dots & \dots \\ \mathbf{I}_3 & (t_{k+n_w} - t_k)\mathbf{I}_3 & \frac{1}{2}(t_{k+n_w} - t_k)^2\mathbf{I}_3 & \dots & \frac{1}{n!}(t_{k+n_w} - t_k)^n\mathbf{I}_3 \end{bmatrix} \quad (4.20)$$

and

$$\mathbf{b}_{SG, \mathbf{o}} = \begin{bmatrix} \mathbf{o}(t_{k-n_w}) \\ \dots \\ \mathbf{o}(t_{k-1}) \\ \mathbf{o}(t_k) \\ \mathbf{o}(t_{k+1}) \\ \dots \\ \mathbf{o}(t_{k+n_w}) \end{bmatrix}, \quad (4.21)$$

such that $\mathbf{A}_{SG} \in \mathbb{R}^{3(2n_w+1) \times 3n}$ and $\mathbf{b}_{SG, \mathbf{o}} \in \mathbb{R}^{3(2n_w+1)}$. The fitted $\widehat{\boldsymbol{\eta}}$ describes the estimated polynomial and its derivatives, centered around the point t_k , which are given by

$$\widehat{\boldsymbol{\xi}}(t_{k+w}, \widehat{\boldsymbol{\eta}}) = \widehat{\boldsymbol{\eta}}_0 + \widehat{\boldsymbol{\eta}}_1(t_{k+w} - t_k) + \frac{1}{2}\widehat{\boldsymbol{\eta}}_2(t_{k+w} - t_k)^2 + \dots + \frac{1}{n!}\widehat{\boldsymbol{\eta}}_n(t_{k+w} - t_k)^n, \quad (4.22)$$

$$\frac{d}{dt}\widehat{\boldsymbol{\xi}}(t_{k+w}, \widehat{\boldsymbol{\eta}}) = \widehat{\boldsymbol{\eta}}_1 + \widehat{\boldsymbol{\eta}}_2(t_{k+w} - t_k) + \dots + \frac{1}{(n-1)!}\widehat{\boldsymbol{\eta}}_n(t_{k+w} - t_k)^{n-1}, \quad (4.23)$$

$$\frac{d^n}{dt^n}\widehat{\boldsymbol{\xi}}(t_{k+w}, \widehat{\boldsymbol{\eta}}) = \widehat{\boldsymbol{\eta}}_n, \quad (4.24)$$

$$(4.25)$$

where $w \in \{-n_w, \dots, -1, 0, 1, \dots, n_w\}$ as before. Note that this means that at the time index of interest, t_k , $\widehat{\boldsymbol{\xi}}$ and its derivatives are given by

$$\widehat{\mathbf{o}}(t_k) = \widehat{\boldsymbol{\eta}}_0, \quad (4.26)$$

$$\widehat{\dot{\mathbf{o}}}(t_k) = \widehat{\boldsymbol{\eta}}_1, \quad (4.27)$$

$$\widehat{\ddot{\mathbf{o}}}(t_k) = \widehat{\boldsymbol{\eta}}_2, \quad (4.28)$$

$$\frac{d^n}{dt^n} \widehat{\mathbf{o}}(t_k) = \widehat{\boldsymbol{\eta}}_n. \quad (4.29)$$

Now, the left-trivialized linear velocity and acceleration can be obtained by

$${}^B \widehat{\mathbf{v}}_{A,B}(t_k) = \widehat{\mathbf{R}}^T(t_k) \widehat{\mathbf{o}}(t_k), \quad (4.30)$$

$${}^B \widehat{\dot{\mathbf{v}}}_{A,B}(t_k) = \widehat{\mathbf{R}}^T(t_k) \widehat{\dot{\mathbf{o}}}(t_k) + \dot{\widehat{\mathbf{R}}}^T(t_k) \widehat{\mathbf{o}}(t_k), \quad (4.31)$$

where $\widehat{\mathbf{R}}$ is as in (G.60). The right-trivialized linear velocity and acceleration can be computed by

$${}^A \widehat{\mathbf{v}}_{A,B}(t_k) = \begin{bmatrix} {}^A \widehat{\mathbf{R}}_B & {}^A \widehat{\mathbf{o}}_B^A \widehat{\mathbf{R}}_B \end{bmatrix} {}^B \widehat{\mathbf{v}}_{A,B}(t_k), \quad (4.32)$$

$${}^A \widehat{\dot{\mathbf{v}}}_{A,B}(t_k) = \begin{bmatrix} {}^A \widehat{\mathbf{R}}_B & {}^A \widehat{\dot{\mathbf{o}}}_B^A \widehat{\mathbf{R}}_B \end{bmatrix} {}^B \widehat{\dot{\mathbf{v}}}_{A,B}(t_k). \quad (4.33)$$

As a side note on the Savitzky-Golay filtering of the position and orientation data, the fitting of a polynomial on the data with the moving window is done for every time instant, except for a time interval at the beginning and at the end of the measurement as it is not possible to fit an entire window on those time instances. More explicitly, the Savitzky-Golay filter is only used at t_k for which $k \in \{n_w + 1, \dots, N - n_w - 1\}$. There are ways to apply the Savitzky-Golay filter on the data of time instants t_k where $k \in \{1, \dots, n_w\} \cup \{N - n_w, \dots, N\}$ [57], however, this is not incorporated in this project as it is not a problem to exclude a few data points from the parameter identification.

Next, the Savitzky-Golay filtering on the position data is validated by applying the Savitzky-Golay filtering on synthetic position data. The synthetic position data is created as following. First, we express

$$\mathbf{o}(t_k) = \mathbf{a}_0 + \mathbf{a}_1 \sin(2\pi f_c t_k), \quad (4.34)$$

$$\dot{\mathbf{o}}(t_k) = \mathbf{a}_1 2\pi f_c \cos(2\pi f_c t_k), \quad (4.35)$$

$$\ddot{\mathbf{o}}(t_k) = -\mathbf{a}_1 (2\pi f_c)^2 \sin(2\pi f_c t_k), \quad (4.36)$$

where $f_c = 1$, $\mathbf{a}_0 = \begin{bmatrix} 0.2 \\ 0.1 \\ -0.2 \end{bmatrix}$, and $\mathbf{a}_1 = \begin{bmatrix} 0.6 \\ -0.4 \\ 0.5 \end{bmatrix}$. The synthetic position data is created for a sampling frequency of 360Hz, which is also the sampling frequency used for the measurements. Using (4.34)-(4.36), the right trivialized linear velocities and accelerations are computed analytically by

$$\mathbf{v}(t_k) = \dot{\mathbf{o}}(t_k) - \dot{\mathbf{R}}(t_k) \mathbf{R}^T(t_k) \mathbf{o}(t_k), \quad (4.37)$$

$$\dot{\mathbf{v}}(t_k) = \ddot{\mathbf{o}}(t_k) - \dot{\mathbf{R}}(t_k) \mathbf{R}^T(t_k) \dot{\mathbf{o}}(t_k) - \ddot{\mathbf{R}}(t_k) \mathbf{R}^T(t_k) \mathbf{o}(t_k), \quad (4.38)$$

where $\dot{\mathbf{R}}(t_k)$ and $\ddot{\mathbf{R}}(t_k)$ are computed by (G.60) and (G.63). The noise corrupted synthetic position data is obtained by

$$\mathbf{o}(t_k) = \mathbf{a}_0 + \mathbf{a}_1 \sin(2\pi f_c t_k) + u(t_k), \quad (4.39)$$

where $u(t_k)$ is the noise which is a random number from a normally distributed set of numbers with mean 0 and standard deviation equal to $\frac{1}{1000}$.

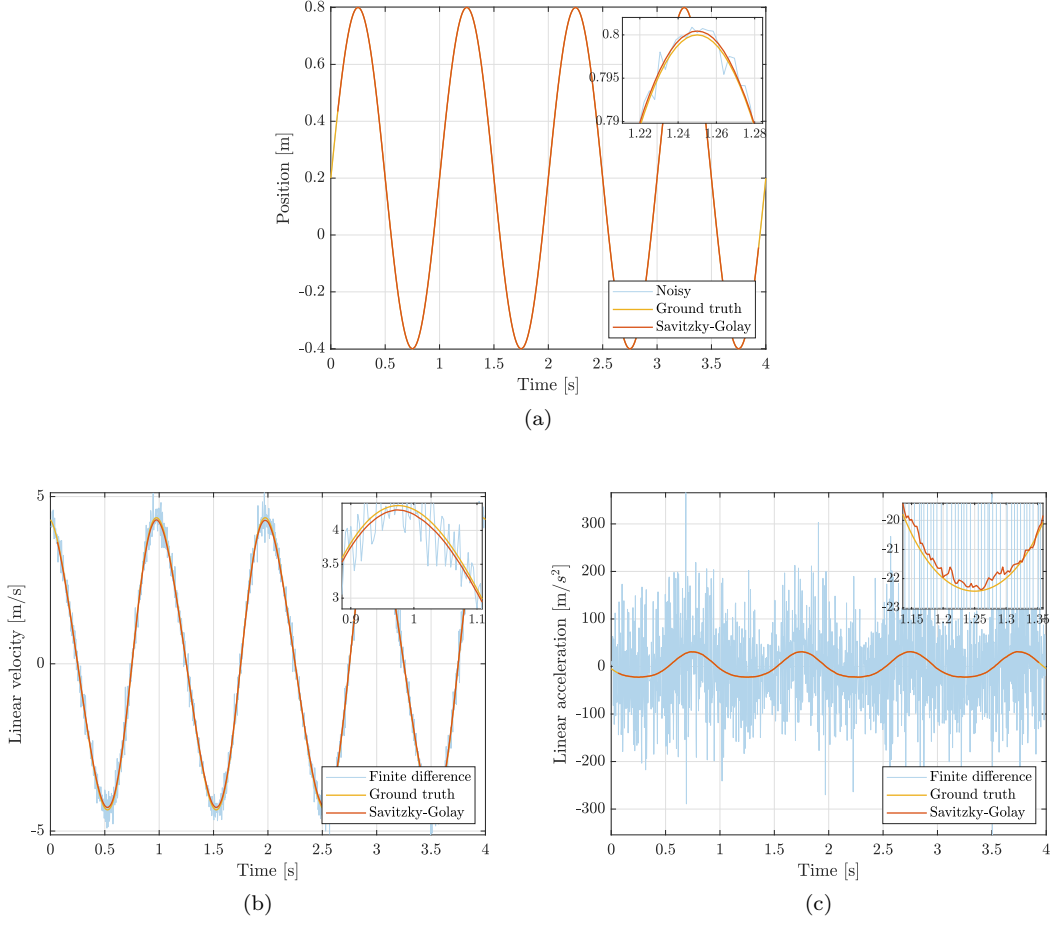


Figure 4.10: The result of the Savitzky-Golay filtering and finite difference approach on noise corrupted synthetic data, compared to the ground truth data synthetic data. Figure (a) shows the position data (${}^A\mathbf{o}_B$). Figures (b) and (c) show the right trivialized linear velocity (${}^A\mathbf{v}_{A,B}$) and acceleration (${}^A\dot{\mathbf{v}}_{A,B}$), respectively.

Figure 4.10a shows the estimated position data, and Figures 4.10b and 4.10c show the estimated linear velocity and acceleration, respectively. Note that Figures 4.10a, 4.10b, and 4.10c show only the result for 1 DOF, namely the position, velocity and acceleration in the x -direction. For the Savitzky-Golay filtering, a window size of 47, so $n_w = 23$, and a 2^{nd} -order polynomial is used. From Figures 4.10b and 4.10c can be concluded that the Savitzky-Golay estimated linear velocity and acceleration are much more accurate compared to the finite difference estimated linear velocity and acceleration.

Savitzky-Golay filtering on $\text{SO}(3)$ data

To apply Savitzky-Golay filtering on the orientation data, we are effectively fitting polynomials on the orientation data for every time step. To write the orientation in a polynomial form, we will use the Lie algebra of the orientation data. In this way we have a n -order polynomial in $\mathfrak{so}(3)$

$$\mathfrak{so}(3) \ni \xi(t; \boldsymbol{\eta}) := \boldsymbol{\eta}_0 + \boldsymbol{\eta}_1 t + \frac{1}{2} \boldsymbol{\eta}_2 t^2 + \dots + \frac{1}{n!} \boldsymbol{\eta}_n t^n, \quad (4.40)$$

where $\boldsymbol{\eta} = [\boldsymbol{\eta}_0; \boldsymbol{\eta}_1; \boldsymbol{\eta}_2; \dots; \boldsymbol{\eta}_n]$ is again a vector of parameters and n is the order of the polynomial fitted to the data within each window. Similar to the Savitzky-Golay filtering on the position data, we can take the time derivatives of this polynomial and consider these functions at the discrete time indices t_k . This gives us

$$\frac{d}{dt} \boldsymbol{\xi}(t_k, \boldsymbol{\eta}) = \boldsymbol{\eta}_1 + \boldsymbol{\eta}_2 t_k + \dots + \frac{1}{(n-1)!} \boldsymbol{\eta}_n t_k^{n-1}, \quad (4.41)$$

$$\frac{d^n}{dt^n} \boldsymbol{\xi}(t_k, \boldsymbol{\eta}) = \boldsymbol{\eta}_n. \quad (4.42)$$

On the orientation data $\mathbf{R}(t_k)$, obtained from the measurements, we again consider a moving time window centered at t_k with the sampled points $t_w = t_k + wT$. This results in the following least-squares problem:

$$\boldsymbol{\xi}^* = \arg \min_{\boldsymbol{\xi}} \sum_{w=-n_w}^{w=n_w} \|\log(\mathbf{R}(t_w) \mathbf{R}(t_k)^{-1}) - \boldsymbol{\xi}(t_w - t_k; \boldsymbol{\eta})\|^2. \quad (4.43)$$

The solution to this least-squares problem can be found by computing

$$\hat{\boldsymbol{\eta}} = \left(\mathbf{A}_{SG}^T \mathbf{A}_{SG} \right)^{-1} \mathbf{A}_{SG}^T \mathbf{b}_{SG, \mathbf{R}} \in \mathbb{R}^{3n}, \quad (4.44)$$

where $\mathbf{A}_{SG} \in \mathbb{R}^{3(2n_w+1) \times 3n}$ is the same as (4.20) and $\mathbf{b}_{SG, \mathbf{R}} \in \mathbb{R}^{3(2n_w+1)}$ is given by

$$\mathbf{b}_{SG, \mathbf{R}} = \begin{bmatrix} \log(\mathbf{R}(t_{k-n_w}) \mathbf{R}(t_k)^T)^\vee \\ \dots \\ \log(\mathbf{R}(t_{k-1}) \mathbf{R}(t_k)^T)^\vee \\ \log(\mathbf{R}(t_k) \mathbf{R}(t_k)^T)^\vee \\ \log(\mathbf{R}(t_{k+1}) \mathbf{R}(t_k)^T)^\vee \\ \dots \\ \log(\mathbf{R}(t_{k+n_w}) \mathbf{R}(t_k)^T)^\vee \end{bmatrix}. \quad (4.45)$$

In (4.44), $\hat{\boldsymbol{\eta}}$ describes the estimated polynomial and its derivatives, centered around the point t_k , which are given by

$$\hat{\boldsymbol{\xi}}(t_{k+w}, \hat{\boldsymbol{\eta}}) = \hat{\boldsymbol{\eta}}_0 + \hat{\boldsymbol{\eta}}_1(t_{k+w} - t_k) + \frac{1}{2} \hat{\boldsymbol{\eta}}_2(t_{k+w} - t_k)^2 + \dots + \frac{1}{n!} \hat{\boldsymbol{\eta}}_n(t_{k+w} - t_k)^n, \quad (4.46)$$

$$\frac{d}{dt} \hat{\boldsymbol{\xi}}(t_{k+w}, \hat{\boldsymbol{\eta}}) = \hat{\boldsymbol{\eta}}_1 + \hat{\boldsymbol{\eta}}_2(t_{k+w} - t_k) + \dots + \frac{1}{(n-1)!} \boldsymbol{\eta}_n(t_{k+w} - t_k)^{n-1}, \quad (4.47)$$

$$\frac{d^n}{dt^n} \hat{\boldsymbol{\xi}}(t_{k+w}, \hat{\boldsymbol{\eta}}) = \hat{\boldsymbol{\eta}}_n, \quad (4.48)$$

$$(4.49)$$

where $w \in \{-n_w, \dots, -1, 0, 1, \dots, n_w\}$ as before. Note that this means that at the time index of interest, t_k , $\hat{\boldsymbol{\xi}}$ and its derivatives are given by

$$\hat{\boldsymbol{\xi}}(t_k, \hat{\boldsymbol{\eta}}) = \hat{\boldsymbol{\eta}}_0, \quad (4.50)$$

$$\frac{d}{dt} \hat{\boldsymbol{\xi}}(t_k, \hat{\boldsymbol{\eta}}) = \hat{\boldsymbol{\eta}}_1, \quad (4.51)$$

$$\frac{d^n}{dt^n} \hat{\boldsymbol{\xi}}(t_k, \hat{\boldsymbol{\eta}}) = \hat{\boldsymbol{\eta}}_n. \quad (4.52)$$

Next we can compute

$$\hat{\mathbf{R}}(t_k) = \exp(\hat{\boldsymbol{\eta}}_0^\wedge) \mathbf{R}(t_k), \quad (4.53)$$

$$\hat{\boldsymbol{\omega}}(t_k) = d \exp(\hat{\boldsymbol{\eta}}_0) \cdot \hat{\boldsymbol{\eta}}_1, \quad (4.54)$$

$$\hat{\boldsymbol{\omega}}(t_k) = d^{2(+)} \exp(\hat{\boldsymbol{\eta}}_0) \cdot (\hat{\boldsymbol{\eta}}_1, \hat{\boldsymbol{\eta}}_1) + d \exp(\hat{\boldsymbol{\eta}}_0) \cdot \hat{\boldsymbol{\eta}}_2, \quad (4.55)$$

where $\widehat{\mathbf{R}}(t_k)$ is the approximated rotation matrix, and $\widehat{\boldsymbol{\omega}}(t_k)$ and $\widehat{\dot{\boldsymbol{\omega}}}(t_k)$ are the approximation right trivialized angular velocity and acceleration, respectively. Furthermore, $d\exp$ is the right trivialized tangent of the exponential mapping and $\mathfrak{d}^{2(+)}\exp$ is the right trivialized geometric Hessian of the exponential mapping with respect to the (+) Cartan-Schouten connection. The derivation of these relations can be found in Appendix G.

Next, the Savitzky-Golay filter on the orientation data is validated by using synthetic synthetic data, which is similar to the validation of the Savitzky-Golay filter on position data. The synthetic data is created as follows. First, we express

$$\boldsymbol{\xi}(t_k) = \mathbf{a}_0 + \mathbf{a}_1 \sin(2\pi f_c t_k), \quad (4.56)$$

$$\dot{\boldsymbol{\xi}}(t_k) = \mathbf{a}_1 2\pi f_c \cos(2\pi f_c t_k), \quad (4.57)$$

$$\ddot{\boldsymbol{\xi}}(t_k) = -\mathbf{a}_1 (2\pi f_c)^2 \sin(2\pi f_c t_k), \quad (4.58)$$

where $f_c = 1$ is the moving frequency of the signal, $\mathbf{a}_0 = \begin{bmatrix} 0.05 \\ -0.15 \\ 0.2 \end{bmatrix}$, and $\mathbf{a}_1 = \begin{bmatrix} 0.4 \\ 0.7 \\ -0.7 \end{bmatrix}$. The synthetic data is again created for a sampling frequency of 360Hz. Using (4.56)-(4.58), the rotation matrices, angular velocities, and angular accelerations can be computed analytically by

$$\mathbf{R}(t_k) = \exp(\boldsymbol{\xi}^\wedge), \quad (4.59)$$

$$\boldsymbol{\omega}(t_k) = d\exp(\boldsymbol{\xi}) \cdot \dot{\boldsymbol{\xi}}, \quad (4.60)$$

$$\dot{\boldsymbol{\omega}}(t_k) = \mathfrak{d}^{2(+)}\exp(\boldsymbol{\xi}) \cdot (\dot{\boldsymbol{\xi}}, \dot{\boldsymbol{\xi}}) + d\exp(\boldsymbol{\xi}) \cdot \ddot{\boldsymbol{\xi}}, \quad (4.61)$$

for $k \in \{1, \dots, N\}$. The noise corrupted synthetic orientation data is obtained by

$$\boldsymbol{\xi}(t_k) = \mathbf{a}_0 + \mathbf{a}_1 \sin(2\pi f_c t_k) + u(t_k), \quad (4.62)$$

$$(4.63)$$

where $u(t_k)$ is again the noise which is a random number from a normally distributed set of numbers with mean 0 and standard deviation equal to $\frac{1}{1000}$.

The result of the Savitzky-Golay filter on synthetic SO(3) data is shown in Figures 4.11a, 4.11b, and 4.11c. Herein, only 1 DOF is shown, namely the rotation around the x -axis of the absolute frame, A . This result is obtained by choosing a window size of 47, so $n_w = 23$, and by fitting an order 2 polynomial. Just like as the Savitzky-Golay filtering on position data, one can see that the Savitzky-Golay estimated angular velocity and acceleration are much more accurate compared to the finite difference method estimated angular velocity and acceleration.

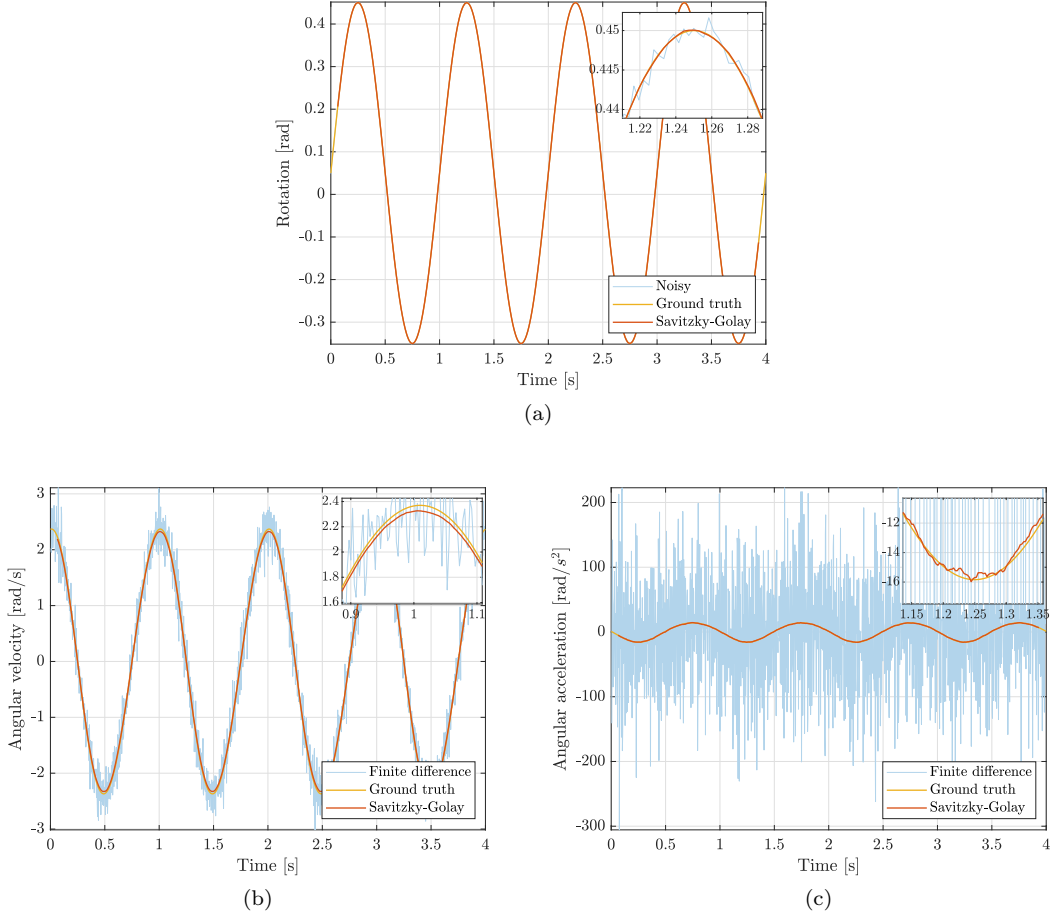


Figure 4.11: The result of the Savitzky-Golay filtering and finite difference on noise corrupted synthetic data, compared to the ground truth data synthetic data. Figures (a) shows the rotation around the x -axis ($({}^A\xi_B)_x$) Figures (b) and (c) show the right-trivialized angular velocity ($({}^A\omega_{A,B})_x$) and angular acceleration ($({}^A\dot{\omega}_{A,B})_x$), respectively.

Velocity and acceleration estimations from measurement data

The Savitzky-Golay filtering is performed on the pose data of the package (${}^A\mathbf{H}_B$) and the tool-arm (${}^A\mathbf{H}_E$). This because we need to have the package body-fixed velocity ${}^B\mathbf{v}_{A,B}$ and ${}^B\dot{\mathbf{v}}_{A,B}$ to use inverse dynamics. However, from the measurements we have the pose data of the suction cup lip (${}^A\mathbf{H}_S$) instead of the pose data of the package (${}^A\mathbf{H}_B$). To this end, first, the pose data of the package is calculated by

$${}^A\mathbf{H}_B(t_k) = {}^A\mathbf{H}_S(t_k) {}^S\mathbf{H}_B, \quad (4.64)$$

for $k \in \{1 \dots N\}$. The homogeneous transformation matrix ${}^S\mathbf{H}_B$ is a constant since we assumed no slip and no deformation of the held package (the plastic plate with attached weights).

The result of the Savitzky-Golay filtering of the $\text{SO}(3) \times \mathbb{R}^3$ data of frame B with respect to frame A is shown in Figures 4.12 and 4.13. The blue lines indicate the estimation by using the finite difference method and the orange lines indicate the estimation from using Savitzky-Golay filtering. A window size of 31 is used and a 3^{rd} -order polynomial is fitted.

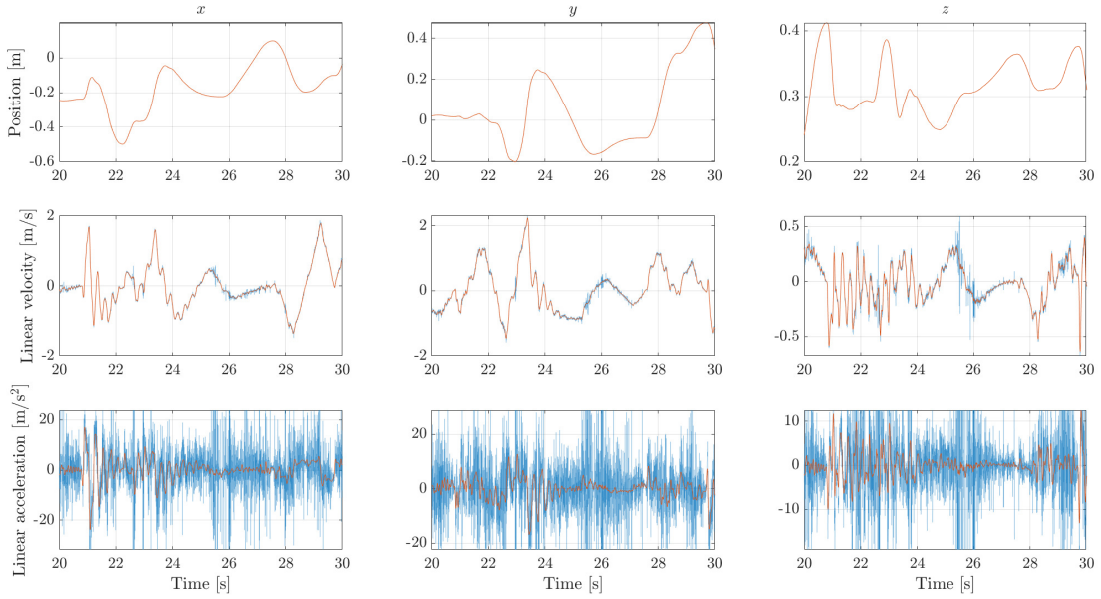


Figure 4.12: A visualization of the smoothed position data (${}^A\mathbf{o}_B$) and the estimated right trivialized linear velocity and acceleration of frame B with respect to frame A , ${}^A\mathbf{v}_{A,B}$ and ${}^A\dot{\mathbf{v}}_{A,B}$, respectively.

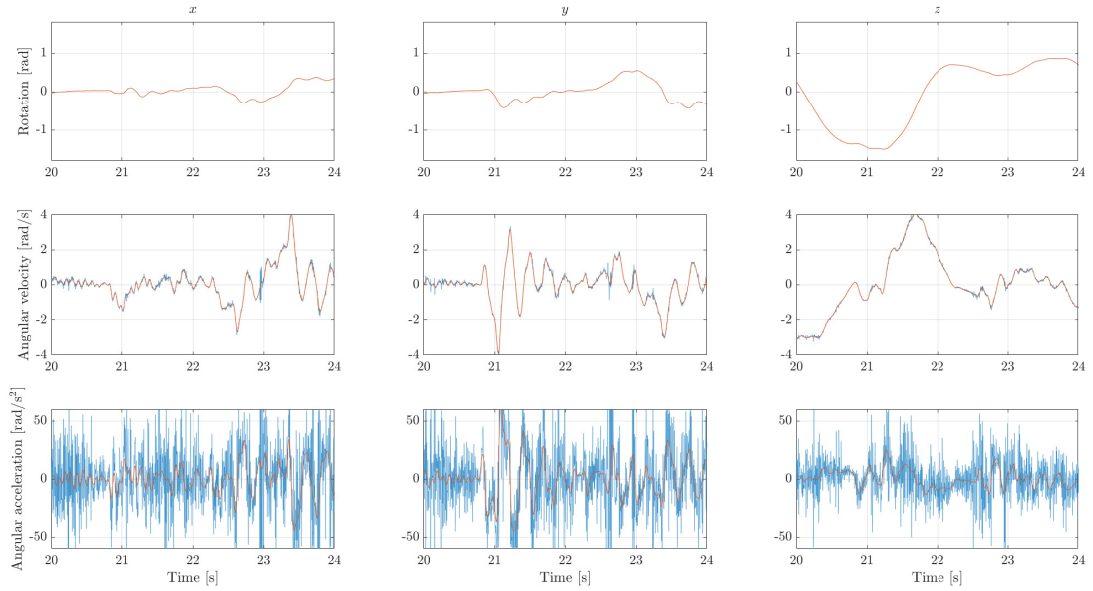


Figure 4.13: A visualization of the smoothed orientation data and the estimated right trivialized angular velocity and acceleration of frame B with respect to frame A , ${}^A\boldsymbol{\omega}_{A,B}$ and ${}^A\dot{\boldsymbol{\omega}}_{A,B}$, respectively.

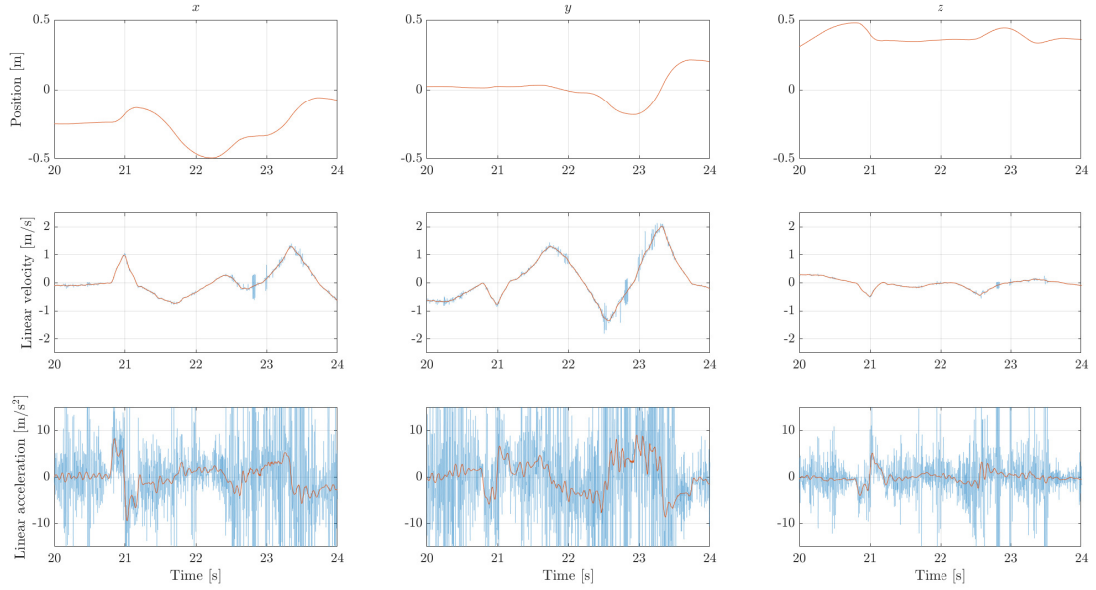


Figure 4.14: A visualization of the smoothed position data (${}^A\mathbf{o}_E$) and the estimated right trivialized linear velocity and acceleration of frame E with respect to frame A , ${}^A\mathbf{v}_{A,E}$ and ${}^A\dot{\mathbf{v}}_{A,E}$, respectively.

The result of the Savitzky-Golay filtering of the $\text{SO}(3) \times \mathbb{R}^3$ data of frame E with respect to frame

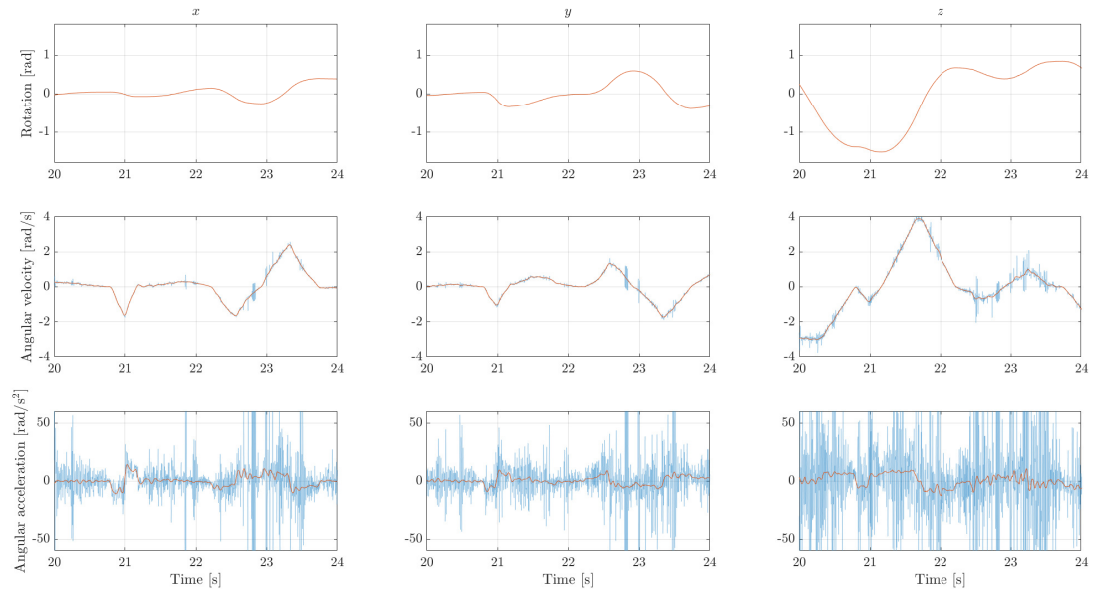


Figure 4.15: A visualization of the smoothed orientation data and the estimated right trivialized angular velocity and acceleration of frame E with respect to frame A , ${}^A\boldsymbol{\omega}_{A,E}$ and ${}^A\dot{\boldsymbol{\omega}}_{A,E}$, respectively.

A is shown in Figures 4.14 and 4.15. For this data, a window size of 51 is used and a 4th-order polynomial is fitted. A larger window and a polynomial of a higher order is used for the data describing the pose of the tip of the tooling arm, because this data contains more noise compared to the data of the package.

A remark on the use of Savitzky-Golay filtering on real measurement data is that it is rather difficult to choose the optimal Savitzky-Golay settings to obtain a reliable estimation of the velocity and the acceleration. For the synthetic data, the results of the filtering can be compared to the ground truth data as shown in Figures 4.11 and 4.10. This is however not possible for the actual measured data. Therefore, the Savitzky-Golay settings are tuned by comparing the Savitzky-Golay estimated velocity to the finite difference estimated velocity. When looking at the Savitzky-Golay estimated acceleration we aim to filter out the high frequency oscillations. Because of the large noise amplitude in the finite difference estimated acceleration, it is almost not possible to compare the Savitzky-Golay estimated acceleration to this finite difference estimated acceleration, see Figures 4.12-4.15. This makes it hard to choose the Savitzky-Golay settings such that we obtain an accurate Savitzky-Golay estimation of the acceleration.

4.3.2 Estimating of stiffness and damping matrices

First, the weighted linear least-squares procedure is explained in this section. This weighted least-squares approach is used to estimate the stiffness matrix (\mathbf{K}) and damping matrix (\mathbf{P}). Thereafter, the resulting estimations for the stiffness and damping matrices are presented. Using these estimated stiffness and damping matrices, the system is simulated for a (from a measurement) known tool-arm trajectory. To validate the model, the simulation data is compared to the measurement data.

Weighted least-squares approach

To determine the stiffness and damping matrices, inverse dynamics will be used. Recall from (3.5) and (3.7) that we have the following model

$$\mathbb{M}\dot{\mathbf{v}}(t_k) + \mathbf{v}\bar{\mathbf{x}}^*(t_k)\mathbb{M}\mathbf{v}(t_k) = \mathbf{f}_{SC \rightarrow PA} \left(\mathbf{K}, {}^E\mathbf{H}_S(t_k), \mathbf{D}, {}^S\mathbf{v}_{E,S}(t_k) \right) + \mathbf{f}_g(\mathbf{H}(t_k)), \quad (4.65)$$

where $\mathbb{M} = {}_B\mathbb{M}_B$, $\mathbf{v}(t_k) = {}^B\mathbf{v}_{A,B}(t_k)$, $\mathbf{f}_g(\mathbf{H}(t_k)) = {}_B\mathbf{f}_g({}^A\mathbf{H}_B(t_k))$, and

$$\mathbf{f}_{SC \rightarrow PA} \left(\mathbf{K}, {}^E\mathbf{H}_S(t_k), \mathbf{D}, {}^S\mathbf{v}_{E,S}(t_k) \right) = {}_B\mathbf{X}^S \left({}_S\mathbf{f}_{SC \rightarrow PA, spring} \left(\mathbf{K}, {}^E\mathbf{H}_S(t_k) \right) + {}_S\mathbf{f}_{SC \rightarrow PA, damper} \left(\mathbf{D}, {}^S\mathbf{v}_{E,S}(t_k) \right) \right).$$

Remember that, as elaborated upon in Section 3.4, the damping matrix \mathbf{D} is parametrized by matrix \mathbf{P} . Because $\mathbf{f}_{SC \rightarrow PA}$ depends linearly on matrices \mathbf{K} and \mathbf{P} , it is possible to use linear least-square fitting to identify these matrices. Therefore, we use a weighted linear least-squares approach, where the optimization problem is defined as

$$\mathbf{x}^* = \arg \min_{\mathbf{x}} \sum_{k=1}^N \left(\mathbf{c}(t_k) - \mathbf{L}(t_k)\mathbf{x} \right)^T \mathbf{W} \left(\mathbf{c}(t_k) - \mathbf{L}(t_k)\mathbf{x} \right), \quad (4.66)$$

where N is the number of data points used for the least-squares fitting and \mathbf{W} is the weighting matrix. Furthermore, we have

$$\mathbf{L}(t_k)\mathbf{x} = \mathbf{f}_{SC \rightarrow PA} \left(\mathbf{K}, {}^E\mathbf{H}_S(t_k), \mathbf{P}, {}^S\mathbf{v}_{E,S}(t_k), l_1, l_2 \right) \in \mathbb{R}^6, \quad (4.67)$$

$$\mathbf{c}(t_k) = {}_S\mathbf{X}^B \left(\mathbb{M}\dot{\mathbf{v}}(t_k) + \mathbf{v}\bar{\mathbf{x}}^*(t_k)\mathbb{M}\mathbf{v}(t_k) - \mathbf{f}_g(t_k) \right) \in \mathbb{R}^6, \quad (4.68)$$

such that $\mathbf{L}({}^E\mathbf{H}_S(t_k), {}^S\mathbf{v}_{E,S}(t_k), l_1, l_2) \in \mathbb{R}^{6 \times n_p}$ contains the kinematic terms of the spring and damping wrenches, and $\mathbf{x} \in \mathbb{R}^{n_p}$ are the entries of the symmetric (semi-)positive definite stiffness and damping matrices \mathbf{K} and \mathbf{P} . Herein is n_p the number of parameter we aim to fit, so for full and symmetric \mathbf{K} and \mathbf{P} matrices, we have $n_p = 2 \times 21 = 42$. Furthermore, note that $\mathbf{c}(t_k)$ is the estimated wrench from the suction cup to the package (using inverse dynamics).

Weighting matrix \mathbf{W} is such that $\mathbf{W} = \mathbf{Q}^{-1} \in \mathbb{R}^{6 \times 6}$, where \mathbf{Q} is the covariance matrix of the estimated wrench working from the suction cup to the package. Each element of this covariance matrix is calculated by

$$\mathbf{Q}_{i,j} = \frac{1}{N-1} \sum_{k=1}^N (\mathbf{c}_i(t_k) - \boldsymbol{\mu}_i) (\mathbf{c}_j(t_k) - \boldsymbol{\mu}_j) \in \mathbb{R}, \quad \text{for } i, j \in \{1, \dots, 6\}, \quad (4.69)$$

where

$$\boldsymbol{\mu} = \frac{1}{N} \sum_{k=1}^N \mathbf{c}(t_k) \in \mathbb{R}^6. \quad (4.70)$$

We use this weighted least-squares method because the used cost function minimizes the error in the estimated forces and torques resulting from the modeled stiffness and damping. One should realize that the forces and torques are not necessarily of the same magnitude. If this is the case, and we would use an unweighted least-squares approach, it could be that the errors in the estimated forces is penalized really hard, meanwhile the errors in the estimated torques would be barely penalized. So, the usage of the weighting matrix assures that the errors of the estimated forces and torques are penalized evenly [51, 52, 58].

Another approach of identifying the stiffness and damping matrix is by using prediction-error methods [59, 60]. This way we would minimize a cost on the basis of the difference of kinematic measured data and those produced by a model for known external forces (gravity acting on the package) and initial conditions (pose and velocity of the robot tool-arm and the package). This approach is not pursued in this report; however, in the recommendations, Section 5.2, we will come back to this approach and mention why we should have pursued this approach. The reason why we pursued the approach as presented in this section(, i.e., using inverse dynamics to estimate the forces and torques and with that the stiffness and damping matrix), is that this approach seemed to be the simplest way to estimate the stiffness and damping matrix. Furthermore, the usage of inverse dynamics was possible because we estimated the accelerations of the package from the Savitzky-Golay filtering of the pose data.

Since we can define (4.67) and (4.68) for every time instant, we can write

$$\mathbf{A} = [\mathbf{L}(t_1); \mathbf{L}(t_2); \dots; \mathbf{L}(t_N)] \in \mathbb{R}^{6N \times n_p}, \quad (4.71)$$

$$\mathbf{b} = [\mathbf{c}(t_1); \mathbf{c}(t_2); \dots; \mathbf{c}(t_N)] \in \mathbb{R}^{6N}, \quad (4.72)$$

such that we have

$$\mathbf{A}\mathbf{x} = \mathbf{b} + \mathbf{e}, \quad (4.73)$$

where \mathbf{e} is the error. For matrix \mathbf{A} holds that if $\text{rank}(\mathbf{A}) = n_p$, then the data is rich enough to solve (4.73) least-squares sense by

$$\mathbf{x}^* = (\mathbf{A}^T \mathbf{Z} \mathbf{A})^{-1} \mathbf{A}^T \mathbf{Z} \mathbf{b}, \quad (4.74)$$

where

$$\mathbf{Z} = \begin{bmatrix} \mathbf{W} & \mathbf{0}_{6 \times 6} & \dots & \mathbf{0}_{6 \times 6} \\ \mathbf{0}_{6 \times 6} & \mathbf{W} & \dots & \mathbf{0}_{6 \times 6} \\ \vdots & \vdots & \ddots & \vdots \\ \mathbf{0}_{6 \times 6} & \mathbf{0}_{6 \times 6} & \dots & \mathbf{W} \end{bmatrix} \in \mathbb{R}^{6N \times 6N}. \quad (4.75)$$

By solving (4.74) we obtain the best fit for the stiffness and damping parameters according to (4.66).

Results

In this part, the following applies for all figures:

- The blue lines indicate the x component.
- The orange lines indicate the y component.
- The green lines indicate the z component.
- The solid lines show the measured data.
- The dashed lines represent the simulated data.

Furthermore, the weighting matrices used to obtain these results are presented in Appendix I. Also, note that there is made use of two different data set, namely an identification set and a validation set [34].

The results of the parameter identification, when fitting a full and symmetric stiffness and damping matrix on the identification measurement data set, are given by (4.76) and (4.77).

$$\mathbf{K}_{full,id} = \begin{bmatrix} 5857 & -591.9 & 37.53 & 7.38 & -15.91 & -48.28 \\ -591.9 & 5132 & 222.3 & 13.41 & -7.951 & -40.44 \\ 37.53 & 222.3 & 1.121 \cdot 10^4 & 17.02 & -4.266 & -18.9 \\ 7.38 & 13.41 & 17.02 & 2.932 & -0.06731 & 0.4012 \\ -15.91 & -7.951 & -4.266 & -0.06731 & 3.365 & -0.3149 \\ -48.28 & -40.44 & -18.9 & 0.4012 & -0.3149 & 1.5400 \end{bmatrix}, \quad (4.76)$$

$$\mathbf{P}_{full,id} = \begin{bmatrix} 61.14 & 1.157 & -3.215 & 0.001236 & -0.9543 & -0.2983 \\ 1.157 & 59.43 & -2.205 & 0.9632 & -0.04314 & -0.1333 \\ -3.215 & -2.205 & 21.57 & -0.489 & 0.01763 & 0.3685 \\ 0.001236 & 0.9632 & -0.489 & 0.05569 & 0.001043 & 0.001421 \\ -0.9543 & -0.04314 & 0.01763 & 0.001043 & 0.05633 & 0.007516 \\ -0.2983 & -0.1333 & 0.3685 & 0.001421 & 0.007516 & 0.09839 \end{bmatrix}. \quad (4.77)$$

The corresponding weighting matrix, i.e., the weighting matrix which is used to obtain (4.76) and (4.77) from the identification measurement data set, is given by (I.82). In (4.76) and (4.77), it can be seen that the stiffness and damping matrix are positive definite and have positive entries on the diagonal, as one should expect. Furthermore, the axial symmetry of the bellows suction cups can be seen in these matrices. For both matrices, the indices (1,1) and (2,2) are quite similar, 12.4% difference in stiffness and 2.8% difference in damping, which indicates that the stiffness and damping is equal in both lateral directions. Also, indices (4,4) and (5,5) are quite similar, 12.8% difference in stiffness and 1.1% difference in damping, which indicates that the rotational stiffness and damping around the \mathbf{x}_E and \mathbf{y}_E should be equal. These axis-symmetrical properties of the bellows suction cup are also expected to see, because of the axial symmetry of the bellows suction cup. As the last example, it can be seen that $\mathbf{K}(1,5) \approx -\mathbf{K}(2,4)$ and $\mathbf{P}(1,5) \approx -\mathbf{P}(2,4)$, 15.7% difference in stiffness and 0.9% difference in damping. This would mean that the coupling for the rotation around the x -axis and the translation along the y -axis would be equal to the coupling for the rotation around the y -axis and the translation along the x -axis. The minus sign is the result of the choice of the coordinate frame. The exception concerning the axial symmetry of

the bellows suction cup are indices (1, 3) and (2, 3). One should expect that these are also very similar, however that is not the case. This could be the result of not using the right identification approach or using a data set that is not rich enough.

If we now use these stiffness and damping matrices for a simulation, (4.76) and (4.77), with as input the pose and estimated velocity data of the tool-arm (of the validation data set), gives the result as shown in Figure 4.16. Herein, it can be seen that there is some drift in the rotation. Furthermore, it can be seen that the rotation around the \mathbf{z}_E -axis is way off.

The drift is caused by incorrect estimated coupling terms in the estimated stiffness matrix. For example, it does not make sense that the translation in the \mathbf{z}_E -direction, elongation of the bellows suction cup, is coupled to the rotation around any axis. This would mean that, when the tooling arm is in a vertical orientation(, i.e., the tool-arm is pointing perpendicular to the earth surface) and holding a package of a certain mass such that axes \mathbf{z}_P and \mathbf{z}_E coincide, the suction cup would also bend. This is of course not the case. To solve this, a diagonal stiffness and damping matrix could be imposed. This means that no coupling terms are included. Furthermore, the observation of axial symmetry can be incorporated into the structure of the stiffness and damping matrix. This results in the following diagonal stiffness and damping matrices:

$$\mathbf{K}_{diag,id} = \begin{bmatrix} 6417 & 0 & 0 & 0 & 0 & 0 \\ 0 & 6417 & 0 & 0 & 0 & 0 \\ 0 & 0 & 1.153 \cdot 10^4 & 0 & 0 & 0 \\ 0 & 0 & 0 & 3.868 & 0 & 0 \\ 0 & 0 & 0 & 0 & 3.868 & 0 \\ 0 & 0 & 0 & 0 & 0 & 1.123 \end{bmatrix}, \quad (4.78)$$

$$\mathbf{P}_{diag,id} = \begin{bmatrix} 66.06 & 0 & 0 & 0 & 0 & 0 \\ 0 & 66.06 & 0 & 0 & 0 & 0 \\ 0 & 0 & 22.35 & 0 & 0 & 0 \\ 0 & 0 & 0 & 0.05458 & 0 & 0 \\ 0 & 0 & 0 & 0 & 0.05458 & 0 \\ 0 & 0 & 0 & 0 & 0 & 0.09736 \end{bmatrix}. \quad (4.79)$$

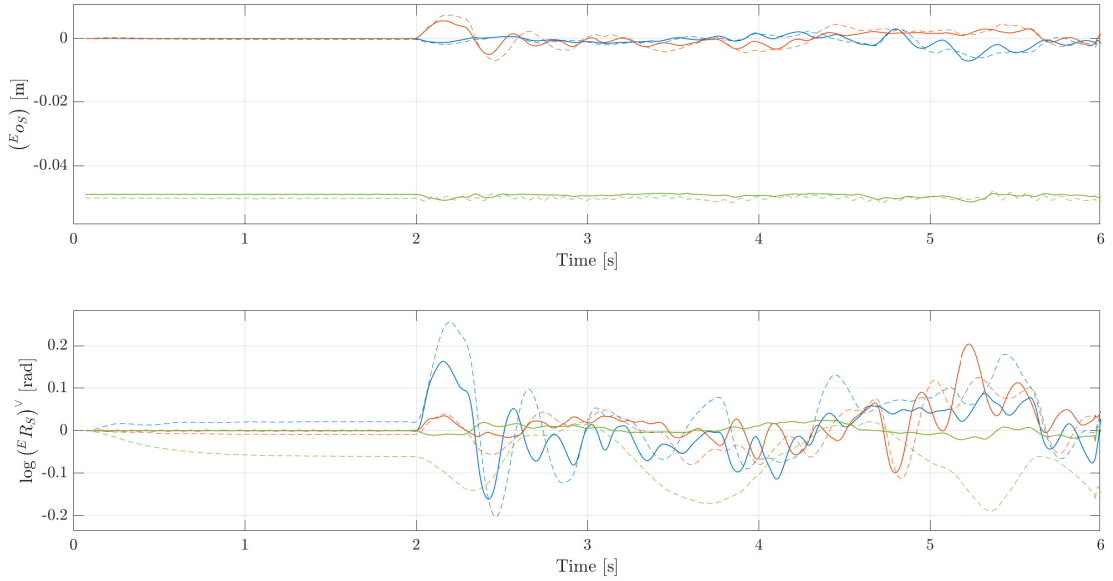


Figure 4.16: Simulation results for using stiffness matrix (4.76) and damping matrix (4.77).

To obtain this stiffness matrix and damping matrix, also a diagonal weighting matrix is used because we now consider the estimated forces and torques (by using inverse dynamics) as linearly independent. The weighting matrix \mathbf{W} is again obtained by taking the inverse of matrix \mathbf{Q} . However, this time \mathbf{Q} is not the covariance matrix, but a diagonal matrix with the variances of the forces or torques on the diagonal:

$$\mathbf{Q} = \begin{bmatrix} \text{var}([\beta_1, \beta_2]) & 0 & 0 & 0 & 0 & 0 \\ 0 & \text{var}([\beta_1, \beta_2]) & 0 & 0 & 0 & 0 \\ 0 & 0 & \text{var}(\beta_3) & 0 & 0 & 0 \\ 0 & 0 & 0 & \text{var}([\beta_4, \beta_5]) & 0 & 0 \\ 0 & 0 & 0 & 0 & \text{var}([\beta_4, \beta_5]) & 0 \\ 0 & 0 & 0 & 0 & 0 & \text{var}(\beta_6) \end{bmatrix}, \quad (4.80)$$

where ‘var’ indicates the variance and

$$\boldsymbol{\beta} = [\mathbf{c}(t_1), \mathbf{c}(t_2), \dots, \mathbf{c}(t_N)] \in \mathbb{R}^{6 \times N}. \quad (4.81)$$

Note that the data of both lateral directions are used together to calculate the variance. This is done because the estimated forces in both lateral directions are used to estimate just one lateral stiffness. In a similar way, this also holds for the rotations around the axes of the lateral directions. The resulting weighting matrix is given by (I.83). Note that by choosing the option to fit such diagonal matrices with imposed axial symmetry, we also choose that the output of the validating simulation (for which the fitted stiffness and damping matrices are used) is more important than the larger residual error of (4.66).

When analyzing (4.78) and (4.79), one can see that most of the diagonal elements of (4.78) and (4.79) are a bit higher than the diagonal elements of the full matrices (4.76) and (4.77), but are still in the same order of magnitude. This is a logic result since there are no coupling terms contributing to the stiffness and damping.

The result of a simulation, where (4.78) and (4.79) are used to describe the stiffness and damping, is shown in Figure 4.17. Herein, it can be seen that the problem of the drift in orientation is solved. Furthermore, it can be seen that the simulation results show some similarity to the measured pose data, except for the rotation around the \mathbf{z}_E -axis. This is because of an inaccurate fit of the stiffness in the torsional direction(, i.e., the rotation around the \mathbf{z}_E -axis). A possible reason for this could be that the parameter identification procedure is not optimal for identifying the torsional stiffness. Choosing a different weighting matrix for the weighted least-squares procedure could open up some possibilities. A better option is to change the parameter identification to the prediction-error method, which will be elaborated upon in the recommendations. Another problem could be that the excitation of the bellows suction cup in the torsional direction is too minimal in the currently used identification measurement data set. This could be the case since that the bellows suction cup is really stiff in the torsional direction and that the torsional excitation of the bellows suction cup during the measurements is limited by the UR10. The UR10 can only achieve rather low angular velocities and angular accelerations of the tooling arm around its center axis. A last possible explanation for the rather low fitted torsional stiffness would be the black foam at the lip of the suction cup (see Figure 1.4). It might be that the plastic plate is not (always) pressed against the dark green lip during the dynamic measurements. Since that the data describing the pose of the suction cup lip is obtained from the markers fixed to the plastic plate, we track the pose of the end of the black foam, instead of the pose of the suction cup lip. Since that the black foam is really soft, it deforms easily. As a result of this, the fitted torsional stiffness might be inaccurate.

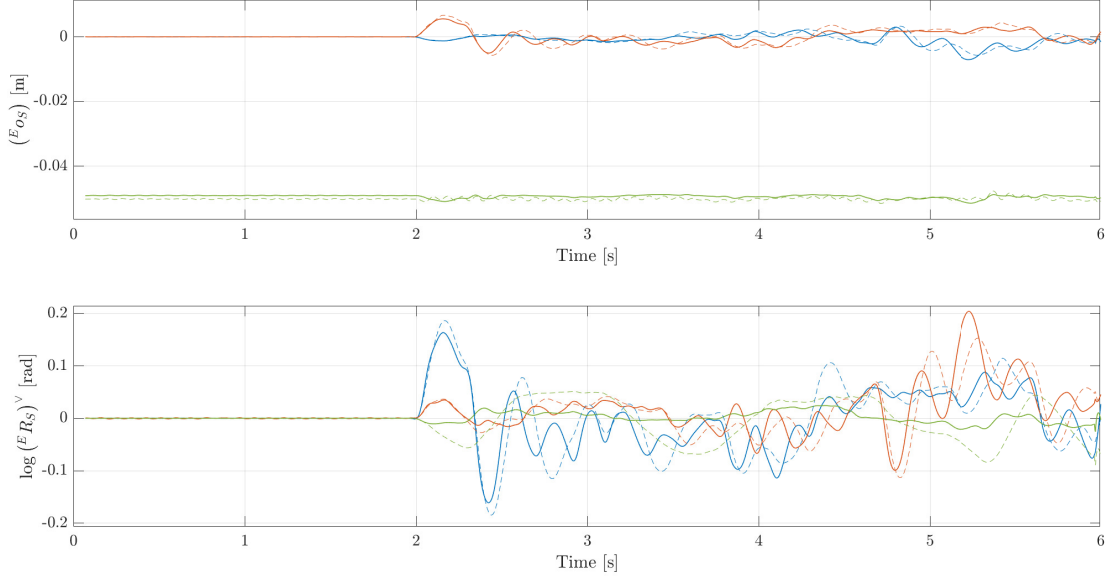


Figure 4.17: Simulation results for using stiffness matrix (4.78) and damping matrix (4.79).

For comparison, the stiffness and damping identification is also carried out on the validation measurement data set. The resulting stiffness and damping matrices are (4.82) and (4.83), respectively. Leaving out the torsional direction, the maximum difference in fitted stiffness is 5.1%. The maximum difference in the damping is 12.7%. The difference could be the result of the data sets being not rich enough. Another option would be that the weighted least-squares procedure is not accurate enough for the identification of the stiffness and damping.

$$\mathbf{K}_{diag,val} = \begin{bmatrix} 6164 & 0 & 0 & 0 & 0 & 0 \\ 0 & 6164 & 0 & 0 & 0 & 0 \\ 0 & 0 & 1.216 \cdot 10^4 & 0 & 0 & 0 \\ 0 & 0 & 0 & 3.921 & 0 & 0 \\ 0 & 0 & 0 & 0 & 3.921 & 0 \\ 0 & 0 & 0 & 0 & 0 & 0.6 \end{bmatrix} \quad (4.82)$$

and

$$\mathbf{P}_{diag,val} = \begin{bmatrix} 62.77 & 0 & 0 & 0 & 0 & 0 \\ 0 & 62.77 & 0 & 0 & 0 & 0 \\ 0 & 0 & 25.21 & 0 & 0 & 0 \\ 0 & 0 & 0 & 0.04975 & 0 & 0 \\ 0 & 0 & 0 & 0 & 0.04975 & 0 \\ 0 & 0 & 0 & 0 & 0 & 0.2036 \end{bmatrix}. \quad (4.83)$$

In the next chapter, some recommendations are presented. These could be used for further research to improve the estimation of the stiffness and damping of the bellows suction cup during the holding phase.

Chapter 5

Conclusion and Recommendations

In Section 5.1, the conclusions of the report are presented. Thereafter, in Section 5.2, several recommendations for further research are suggested.

5.1 Conclusion

In this report, first approaches for the modeling and identification of the bellows suction cup dynamics during the holding phase are presented. By having a model which describes the bellows suction cup dynamics during the holding phase, we should be able to predict the state (pose and velocity) of a package for a given tool-arm trajectory and given package properties. To this end, there is a clear need to identify and model the stiffness and damping of the bellows suction cup. As elaborated upon in Chapter 3, the stiffness of the bellows suction cup (during the holding phase) is modeled, based on the previous work of Fasse and Breedveld. Furthermore, we came up with a velocity depending damping model. To identify the nominal length, the stiffness, and the damping of the bellows suction cup during holding phase, several measurements are performed, as presented in Chapter 4. The measurement data (the OptiTrack data, the Intel RealSense camera data, the UR10 data, and a YAML-file containing the measurements specifications) is saved such that it is reusable and publicly available for further research, something which is not discussed further in this report. From static measurements, we identified the nominal length of the bellows during the holding phase as 0.0481m. The stiffness and damping matrices are identified from dynamic measurements by using inverse dynamics in combination with a weighted least-squares approach. Hereby, the stiffness and damping matrices are obtained by minimizing a cost based on the difference between the inertial forces plus the external forces (gravity) and the internal forces (forces as the result of the stiffness and damping). From the validation can be seen that this gives promising results, however, there is still a large error between simulated and measured dynamic behavior. Because of the too large error between the simulated and measured dynamic behavior, it is no use to quantify the error. In the next section, some recommendations are presented for the continuation of the research on this topic.

5.2 Recommendations

For continuation of the research on the modeling and identification of bellows suction cup dynamics during the holding phase, the following recommendations are made:

- The first recommendation is to change the parameter identification procedure. In this project, the stiffness and damping matrices are identified by using inverse dynamics in combination with a weighted linear least-squares approach. As mentioned in Section 4.3.2, another way would be prediction-error-based parameter identification [59–61]. This method uses forward dynamics to simulate the model for initial guesses of the stiffness and damping

matrices. By comparing the simulation data to the measured data, the best estimations for the stiffness and damping matrices are obtained by using a maximum likelihood estimation or least-squares fitting. Next, the initial guess for the stiffness and damping can be updated. This way the procedure can be repeated until the estimated stiffness and damping converged to a certain value. This approach of identifying the stiffness and damping has multiple advantages compared to the approach as taken in this report:

1. The usage of prediction-error-based parameter identification enables the use of different cost criteria that are used to fit the stiffness and damping matrices. The used cost function for the parameter identification (in this report) is based on wrenches, (4.66)-(4.68). This means that the error we are minimizing is also expressed in forces and torques, or equivalently, linear and angular accelerations. However, since we aim to build a model which can predict the pose and velocity of a package, this is possibly not the best cost criteria to use. By using a prediction-error method, the cost criteria can be expressed such that we minimize the error in position and/or velocity between simulated and measured data. This could result in more accurate identification results.
 2. Only the velocity needs to be estimated from the measured pose data when using a prediction-error method. This is because the forward dynamics simulated pose and velocity data will be compared to the measured pose data and its estimated velocity. This would make the task of finding the optimal Savitzky-Golay settings much easier because it is hard to determine whether the estimated acceleration is a good estimation. Furthermore, a source of error would be eliminated from the stiffness and damping identification. Since that the acceleration is possibly not accurately estimated, the parameter identification as performed in this report (by using inverse dynamics and thus using the estimated acceleration) is possibly not very accurate. So, changing the parameter identification to a prediction-error approach could result in more accurately estimated stiffness and damping matrices.
 3. Prediction-error methods are iterating procedures. This makes it more accessible to check the convergence of the estimated parameters. The convergence of the estimated parameters could indicate if the identification measurement set is rich enough.
- Check if the performed experiments contain enough information for reliable parameter identification results. As explained in Section 4.1.1, the measurements are performed by programming the UR10 to move along a set of arbitrarily chosen waypoints (i.e., poses defined for the robot arm end-effector). This is not the best way of performing identification measurements. An improvement would be to create a trajectory, which ensures that the measured identification data set is rich enough.
 - The validation of the model could be expanded by evaluating some static measurements for which the tool-arm is kept in a fixed pose. When keeping the tool-arm in a fixed pose, there will be no damping of the bellows suction cup. So, by evaluating the pose of the package with respect to the tool-arm, the spring model can be validated separately from the damping model. This can be done for several static measurements where the package mass can be varied and the tool-arm is kept in different orientations.
 - To improve the results from the stiffness and damping identification, as performed in this report, static measurement data could be added to the identification data set. Furthermore, the identification data set can be extended with measurement data of dynamic measurements with different weights.
 - Perform dynamic measurements with different masses attached to the plastic plate and carry out the stiffness and damping identification for the different dynamic measurements. If this would result in big differences in the estimated stiffness and damping matrices, it should be considered to change the stiffness and damping model.

- In this report, we applied the Savitzky-Golay filtering on the measured tool-arm and package pose data, ${}^A\mathbf{H}_E$ and ${}^A\mathbf{H}_B$, respectively. From this, we obtained the velocity and acceleration of the tool-arm (${}^E\mathbf{v}_{A,E}$ and ${}^E\dot{\mathbf{v}}_{A,E}$) and the package (${}^B\mathbf{v}_{A,B}$ and ${}^B\dot{\mathbf{v}}_{A,B}$). These velocity terms (${}^E\mathbf{v}_{A,E}$ and ${}^B\mathbf{v}_{A,B}$) can be rewritten to the velocity of the suction cup lip with respect to the tool-arm, ${}^S\mathbf{v}_{E,S}$, which is necessary to calculate the damping wrench, (3.35), during the parameter identification. However, it is possible to rewrite the package body fixed velocity and acceleration in terms of ${}^S\mathbf{v}_{E,S}$, ${}^S\dot{\mathbf{v}}_{E,S}$, ${}^E\mathbf{v}_{A,E}$, and ${}^E\dot{\mathbf{v}}_{A,E}$, as presented in Appendix J. Doing so, it would be possible to apply the Savitzky-Golay filtering on ${}^A\mathbf{H}_E$ and ${}^E\mathbf{H}_S$ data, instead of ${}^A\mathbf{H}_E$ and ${}^A\mathbf{H}_B$. Because the goal is to identify the bellows suction cup dynamics (i.e., the dynamic behavior of frame S with respect to frame E), it could be that directly obtaining the velocity and acceleration of the suction cup lip with respect to the tool-arm gives a more accurate result for the parameter identification.

The identification and modeling of the bellows suction cup dynamics are performed to predict the release state (pose and velocity) of a package. To make these predictions, not only the holding phase needs to be modeled, but also the release phase. Therefore, the model should be expanded with a release phase to be useful for the robotic tossing of packages.

Bibliography

- [1] M. Meeker, ‘Internet Trends 2019,’ Bond, San Francisco, Tech. Rep., 2019.
- [2] S. Lone, I. Fàvero, L. Quagliari and S. Packiaraja, ‘European Ecommerce Report,’ Ecommerce Foundation, Brussels, Tech. Rep., 2019. [Online]. Available: www.ecommerce-europe.eu.
- [3] J. Clement, *E-commerce worldwide - Statistics & Facts — Statista*. [Online]. Available: <https://www.statista.com/topics/871/online-shopping/> (visited on 27/05/2020).
- [4] D. Sparkman, *Labor Shortage Hurts Logistics Industry*, 2018. [Online]. Available: <https://www.mhlnews.com/warehousing/article/22055211/labor-shortage-hurts-logistics-industry> (visited on 21/05/2020).
- [5] I.A.M., *Home*. [Online]. Available: <https://i-am-project.eu/index.php> (visited on 05/11/2020).
- [6] A. Saccon, *Eindhoven University of Technology: Future Packing robots exploit collision, instead of fearing them*, 2020. [Online]. Available: <https://www.tue.nl/en/news/news-overview/27-02-2020-future-packing-robots-exploit-collisions-instead-of-fearing-them/> (visited on 23/05/2020).
- [7] L. Poort, *Predictive performance of nonsmooth rigid-body collision models for carton box impacts*, MSc thesis, D&C, TU/e, Eindhoven, 2020.
- [8] Piab, *Home*. [Online]. Available: <https://www.piab.com/> (visited on 18/06/2020).
- [9] R. A Letourneau, *What Are the Best Types of Cups for Your Workpiece?* 2019. [Online]. Available: <https://blog.robotiq.com/what-are-the-best-types-of-cups-for-your-workpiece> (visited on 19/05/2020).
- [10] A. Zeng, S. Song, J. Lee, A. Rodriguez and T. Funkhouser, ‘TossingBot: Learning to Throw Arbitrary Objects with Residual Physics,’ *IEEE Transactions on Robotics*, vol. 36, no. 4, pp. 1307–1319, 2020. DOI: 10.1109/TR0.2020.2988642.
- [11] L. Custodio and R. Machado, ‘Flexible automated warehouse: a literature review and an innovative framework,’ *International Journal of Advanced Manufacturing Technology*, vol. 106, no. 1-2, pp. 533–558, 2020. DOI: 10.1007/s00170-019-04588-z.
- [12] R. Syed, S. Suriadi, M. Adams, W. Bandara, S. J. J. Leemans, C. Ouyang, A. H. M. Ter Hofstede, I. Van De Weerd, M. T. Wynn and H. A. Reijers, ‘Robotic Process Automation: Contemporary themes and challenges,’ *Computers in Industry*, vol. 115, p. 103162, 2020. DOI: 10.1016/j.compind.2019.103162.
- [13] Y. Li, T. Huang and D. G. Chetwynd, ‘An approach for smooth trajectory planning of high-speed pick-and-place parallel robots using quintic B-splines,’ *Mechanism and Machine Theory*, vol. 126, pp. 479–490, 2018. DOI: 10.1016/j.mechmachtheory.2018.04.026.
- [14] Smart Robotics, *Home*. [Online]. Available: <https://www.smart-robotics.nl/>.
- [15] Vanderlande, *Home*. [Online]. Available: <https://www.vanderlande.com/>.
- [16] Universal Robotics, *UR10 Industrial Robot*. [Online]. Available: <http://www.universal-robots.com/products/ur10-robot/> (visited on 19/05/2020).

- [17] RS Media Solutions, *Vanderlande auf der LogiMat 2017 - YouTube*, 2017. [Online]. Available: https://www.youtube.com/watch?v=AR_WcSyVzsc&t=85s (visited on 23/05/2020).
- [18] Plenamediatv, *LogiMAT 2019 - Vanderlande Messefilm - YouTube*, 2019. [Online]. Available: https://www.youtube.com/watch?v=k02gbl_CYgw (visited on 23/05/2020).
- [19] Vanderlande, *Warehousing Innovative systems: SIR*. [Online]. Available: <https://www.vanderlande.com/warehousing/innovative-systems/picking/smart-item-robotics/> (visited on 19/05/2020).
- [20] —, *Vanderlande to showcase Smart Item Robotics at LogiMAT 2017*. [Online]. Available: <https://www.vanderlande.com/news/vanderlande-to-showcase-smart-item-robotics-at-logimat-2017/> (visited on 23/05/2020).
- [21] Schmalz, *Vacuum Ejectors*. [Online]. Available: <https://www.schmalz.com/en/vacuum-knowledge/the-vacuum-system-and-its-components/vacuum-generators/vacuum-ejectors/> (visited on 25/05/2020).
- [22] J. Tanaka, A. Ogawa, H. Nakamoto, T. Sonoura and H. Eto, ‘Suction pad unit using a bellows pneumatic actuator as a support mechanism for an end effector of depalletizing robots,’ *Robomech Journal*, vol. 7, no. 2, 2020. DOI: 10.1186/s40648-019-0151-0.
- [23] S. Hasegawa, K. Wada, K. Okada and M. Inaba, ‘A three-fingered hand with a suction gripping system for warehouse automation,’ *Journal of Robotics and Mechatronics*, vol. 31, no. 2, pp. 289–304, 2019. DOI: 10.20965/jrm.2019.p0289.
- [24] E. D. Fasse and P. C. Breedveld, ‘Modeling of elastically coupled bodies: Part I—general theory and geometric potential function method,’ *Journal of Dynamic Systems, Measurement and Control, Transactions of the ASME*, vol. 120, no. 4, pp. 496–500, 1998. DOI: 10.1115/1.2801491.
- [25] S. Zhang and E. D. Fasse, ‘Spatial Compliance Modeling Using a Quaternion-Based Potential Function Method,’ *Multibody System Dynamics*, vol. 4, no. 1, pp. 75–101, 2000. DOI: 10.1023/A:1009895915332.
- [26] E. D. Fasse and P. C. Breedveld, ‘Modeling of elastically coupled bodies: Part II—exponential and generalized coordinate methods,’ *Journal of Dynamic Systems, Measurement and Control, Transactions of the ASME*, vol. 120, no. 4, pp. 501–506, 1998. DOI: 10.1115/1.2801492.
- [27] M. W. Spong, S. Hutchinson and M. Vidyasagar, *Robot modeling and control*, 1st ed. Hoboken: John Wiley & Sons Inc, 2006, ISBN: 9780471765790.
- [28] S Zhang, ‘Lumped-parameter modelling of elastically coupled bodies: Derivation of constitutive equations and determination of stiffness matrices,’ Ph.D. dissertation, The University of Arizona, Tucson, 1999.
- [29] C. Qiu, ‘Screw Theory Based Stiffness Analysis of Compliant Parallel Mechanisms,’ Ph.D. dissertation, Nanyang Technological University, Singapore, 2016.
- [30] C. Qiu, P. Qi, H. Liu, K. Althoefer and J. S. Dai, ‘Six-Dimensional Compliance Analysis and Validation of Orthoplanar Springs,’ *Journal of Mechanical Design, Transactions of the ASME*, vol. 138, no. 4, 2016. DOI: 10.1115/1.4032580.
- [31] M. Žefran and V. Kumar, ‘A geometrical approach to the study of the Cartesian stiffness matrix,’ *Journal of Mechanical Design, Transactions of the ASME*, vol. 124, no. 1, pp. 30–38, 2002. DOI: 10.1115/1.1423638.
- [32] S. Stramigioli and V. Duindam, *Variable Spatial Springs for Robot Control Applications*, Proceedings IROS2001: 2001 IEEE/RSJ International Conference on Intelligent Robots and Systems, 2001. DOI: 10.1109/IR0S.2001.976352.
- [33] S. Rangel, H. Navarro and L. Cabezas-Gómez, ‘Dynamics analysis of a single cylinder hermetic reciprocating compressor,’ *The Academic Society Journal*, vol. 2, no. 3, pp. 139–155, 2018. DOI: 10.32640/tasj.2018.3.139.

-
- [34] B. Deutschmann, T. Liu, A. Dietrich, C. Ott and D. Lee, ‘A Method to Identify the Non-linear Stiffness Characteristics of an Elastic Continuum Mechanism,’ *IEEE Robotics and Automation Letters*, vol. 3, no. 3, pp. 1450–1457, 2018. DOI: 10.1109/LRA.2018.2800098.
- [35] G. Mantriota and A. Messina, ‘Theoretical and experimental study of the performance of flat suction cups in the presence of tangential loads,’ *Mechanism and Machine Theory*, vol. 46, no. 5, pp. 607–617, 2011. DOI: 10.1016/j.mechmachtheory.2011.01.003.
- [36] H. Pham and Q. C. Pham, ‘Critically fast pick-and-place with suction cups,’ in *IEEE International Conference on Robotics and Automation. Proceedings, Montreal*, Nanyang Technological University, Singapore, Nanyang, 2019, pp. 3045–3051. DOI: 10.1109/ICRA.2019.8794081.
- [37] M. J. Jongeneel, *Model-Based Visual Object Tracking with Collision Models*, MSc thesis, D&C, TU/e, Eindhoven, 2020.
- [38] Y. Ma, S. Soatto, J. Košecá and S Shankar Sastry, *An Invitation To 3-D Vision*. New York: Springer-Verlag, 2004, vol. 26, ISBN: 9781441918468. DOI: 10.1007/978-0-387-21779-6.
- [39] V Varadarajan, *Lie Groups, Lie Algebras, and Their Representations*. New York: Springer-Verlag, 1984, vol. 102, ISBN: 978-1-4612-7016-4. DOI: 10.1007/978-1-4612-1126-6.
- [40] S. Traversaro and A. Saccon, ‘Multibody dynamics notation (version 2),’ *Dynamics and Control, Eindhoven University of Technology*, 2019.
- [41] R. M. Murray, Z. Li and S Shankar Sastry, *A mathematical introduction to robotic manipulation*. CRC Press, 1994, ISBN: 9781351469791. DOI: 10.1201/9781315136370.
- [42] Y. Wang and G. S. Chirikjian, ‘Nonparametric second-order theory of error propagation on motion groups,’ *International Journal of Robotics Research*, vol. 27, no. 11-12, pp. 1258–1273, 2008. DOI: 10.1177/0278364908097583.
- [43] A. Müller, ‘Coordinate Mappings for Rigid Body Motions,’ *Journal of Computational and Nonlinear Dynamics*, vol. 12, no. 2, 2017. DOI: 10.1115/1.4034730.
- [44] M. J. A. Zeestraten, ‘Programming by Demonstration on Riemannian Manifolds,’ Ph.D. dissertation, University of Genova, 2017.
- [45] K. M. Lynch and F. Park, *Modern Robotics -Mechanics, Planning, and Control*, 1st ed. Cambridge University Press, 2017, ISBN: 9781107156302.
- [46] J Gallier and D Xu, ‘COMPUTING EXPONENTIALS OF SKEW-SYMMETRIC MATRICES AND LOGARITHMS OF ORTHOGONAL MATRICES,’ *International Journal of Robotics and Automation*, vol. 17, no. 4, 2003. DOI: <https://doi.org/10.1016/j.cam.2009.11.032>.
- [47] J. R. Cardoso and F. S. Leite, ‘Exponentials of skew-symmetric matrices and logarithms of orthogonal matrices,’ *Journal of Computational and Applied Mathematics*, vol. 233, no. 11, pp. 2867–2875, 2010. DOI: 10.1016/j.cam.2009.11.032.
- [48] G. Gallego and A. Yezzi, ‘A Compact Formula for the Derivative of a 3-D Rotation in Exponential Coordinates,’ *Journal of Mathematical Imaging and Vision*, vol. 51, no. 3, pp. 378–384, 2015. DOI: 10.1007/s10851-014-0528-x. arXiv: 1312.0788.
- [49] *Motive Software Setup and Usage - Stanford Flight Room*. [Online]. Available: https://stanfordflightroom.github.io/motion_capture_motive (visited on 25/06/2021).
- [50] E. Otten, ‘Inverse and forward dynamics: Models of multi-body systems,’ *Philosophical Transactions of the Royal Society B: Biological Sciences*, vol. 358, no. 1437, pp. 1493–1500, 2003. DOI: 10.1098/rstb.2003.1354.
- [51] A. D. Kuo, ‘A least-squares estimation approach to improving the precision of inverse dynamics computations.,’ eng, *Journal of biomechanical engineering*, vol. 120, no. 1, pp. 148–159, 1998. DOI: 10.1115/1.2834295.

- [52] A. J. Van Den Bogert and A. Su, 'A weighted least squares method for inverse dynamic analysis A weighted least squares method for inverse dynamic analysis,' *Computer Methods in Biomechanics and Biomedical Engineering*, vol. 11, no. 1, 2008. DOI: 10.1080/10255840701550865.
- [53] A. Savitzky and M. J. E. Golay, 'Smoothing and Differentiation of Data by Simplified Least Squares Procedures.,' *Analytical Chemistry*, vol. 36, no. 8, pp. 1627–1639, 1964. DOI: 10.1021/ac60214a047.
- [54] M. A. Vargas, J. P. Fernández, J. M. Velasco García, J. A. Cabrera Carrillo and J. J. Castillo Aguilar, 'A novel method for determining angular speed and acceleration using sin-cos encoders,' *Sensors*, vol. 21, no. 2, pp. 1–21, 2021. DOI: 10.3390/s21020577.
- [55] D. Bugrov, A. Lebedev and V. Chertopolokhov, 'Estimation of Angular Rotation Velocity of a Body Using a Traching System,' *Allerton Press, Inc.*, vol. 69, no. 1, pp. 25–27, 2014. DOI: 10.3103/S0027133014010051.
- [56] J. Qi, Z. Miao, Z. Wang and S. Zhang, 'Several methods of smoothing motion capture data,' *Proceeding of SPIE - The International Society for Optical Engineering*, vol. 8009, 2011. DOI: 10.1117/12.896512.
- [57] P. A. Gorry, 'General Least-Squares Smoothing and Differentiation by the Convolution (Savitzky-Golay) Method,' *Analytical Chemistry*, vol. 62, no. 2, pp. 35–42, 1990. DOI: 10.1021/ac00205a007.
- [58] A. R. Amiri-Simkooei, 'Least-Squares Variance Component Estimation: Theory and GPS Applications,' Ph.D. dissertation, TU Delft, 2007, pp. 1–220.
- [59] L. Ljung and T. Glad, *Modeling of Dynamic Systems*. New Jersey: Prentice-Hall, Inc., 1994, ISBN: 0135970970.
- [60] L. Ljung, *System Identification: theory for the user*, 2nd ed., A. Procházka, J. Uhlír, P. W. J. Rayner and N. G. Kingsbury, Eds. Upper saddle river, NJ: Prentice Hall PTR, 1999, ISBN: 0-13-656695-2.
- [61] J. L. Crassidis and J. L. Junkins, *OPTIMAL ESTIMATION of DYNAMIC SYSTEMS*. Boca Raton: CRC Press LLC, 2004, ISBN: 158488391X.
- [62] R. A. Adams and C Essex, *Calculus: A Complete Course*. Toronto: Pearson, 2013, ISBN: 9780321781079.
- [63] R. Mickens, *Difference Equations and Advanced Topics Difference Equations*, 3rd ed. New York: Chapman and Hall/CRC, 2015, p. 555, ISBN: 9781482230796. DOI: <https://doi.org/10.1201/b18186>.
- [64] J. Park and W.-K. Chung, 'Geometric integration on Euclidean group with application to articulated multibody systems,' *IEEE Transactions on Robotics*, vol. 21, no. 5, pp. 850–863, 2005. DOI: 10.1109/TR0.2005.852253.

Appendices

A Generalized inertia tensor

The generalized inertia tensor, as used in (3.5), is explicitly given by

$${}^B\mathbb{M}_B = \begin{bmatrix} m \mathbf{I}_3 & \mathbf{0}_{3 \times 3} \\ \mathbf{0}_{3 \times 3} & {}^B\mathbb{I}_B \end{bmatrix}, \quad (\text{A.1})$$

where $\mathbf{I}_3 \in \mathbb{R}^{3 \times 3}$ is the identity matrix, m is the mass of the package, and ${}^B\mathbb{I}_B \in \mathbb{R}^{3 \times 3}$ is the inertia tensor expressed in frame B . The inertia tensor for a box shaped package with homogeneous distributed mass can be computed by

$${}^B\mathbb{I}_B = \begin{bmatrix} \frac{1}{12}m(h^2 + w^2) & 0 & 0 \\ 0 & \frac{1}{12}m(h^2 + d^2) & 0 \\ 0 & 0 & \frac{1}{12}m(d^2 + w^2) \end{bmatrix}, \quad (\text{A.2})$$

where h , w , and d are the dimensions as shown in Figure 5.1a.

When holding the plastic plate in combination with some cylindrical weights, as pictured in Figure 5.2, the total generalized inertia tensor can be obtained by

$${}^B\mathbb{M}_B^{(\text{total})} = \sum_{i=1}^{N_o} {}^B\mathbf{X}_{F_i} {}^{F_i}\mathbb{M}_{F_i}^{(\text{part } i) F_i} \mathbf{X}_B, \quad (\text{A.3})$$

where ${}^B\mathbb{M}_B^{(\text{total})}$ is the generalized inertia tensor with respect to the center of mass of the combined plastic plate and attached weights, and N_o is the number of parts/objects (plastic plate and

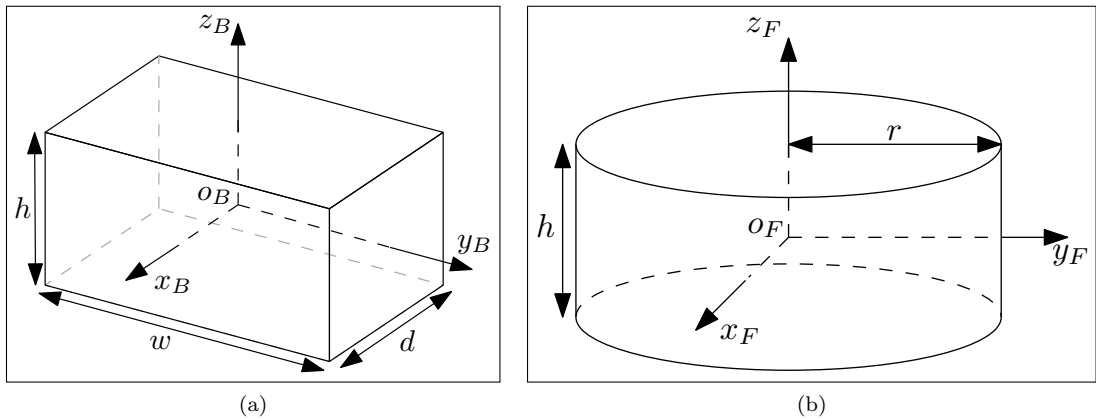


Figure 5.1: Figure (a) shows the height h , width w , and depth d of a box shaped package. Frame B is fixed to the center of mass of the box. Figure (b) indicates the height h and the radius r of the cylindrical weight. Frame F_1 is fixed to the center of mass of the cylindrical weight.

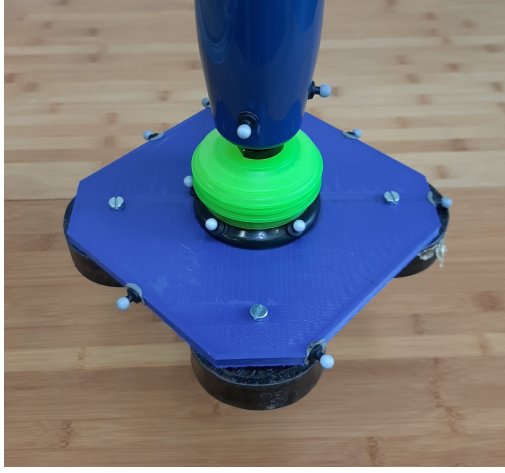


Figure 5.2: Plastic plate in combination with the rigidly attached cylindrical shaped weights.

weights). Furthermore, F indicates the frame fixed to the center of mass of a certain part (plastic plate or one of the attached weights). In the case of the plastic plate, the inertia tensor can be approximated by using (A.2). The inertia tensors of the cylindrical shaped weights can be obtained by

$${}_{F_i}\mathbb{I}_{F_i} = \begin{bmatrix} \frac{1}{12}m_i(3r^2 + h^2) & 0 & 0 \\ 0 & \frac{1}{12}m_i(3r^2 + h^2) & 0 \\ 0 & 0 & \frac{1}{2}m_i r^2 \end{bmatrix}, \quad (\text{A.4})$$

where m_i is the mass of the cylindrical shaped weight and r and h are as indicated in Figure 5.1b.

B Approximations

The matrix logarithm of a rotation matrix can be written to the following form

$$\log(\mathbf{R}) = \frac{\theta}{2\sin(\theta)} (\mathbf{R} - \mathbf{R}^T). \quad (\text{B.5})$$

This formula is the inverse of the Rodrigues' rotation formula [41] [46]. Note that θ is the rotation angle around the axis unit vector of the axis-angle representation (thus not an Euler angle). For θ approaching zero, we can write

$$\lim_{\theta \rightarrow 0} \frac{\theta}{\sin(\theta)} = 1. \quad (\text{B.6})$$

Figures 5.3a and 5.3b show the value of $\frac{\theta}{\sin(\theta)}$ and the relative error of the approximation, respectively. The relative error is calculated by $\frac{1 - \frac{\theta}{\sin(\theta)}}{\frac{\theta}{\sin(\theta)}} \cdot 100\%$.

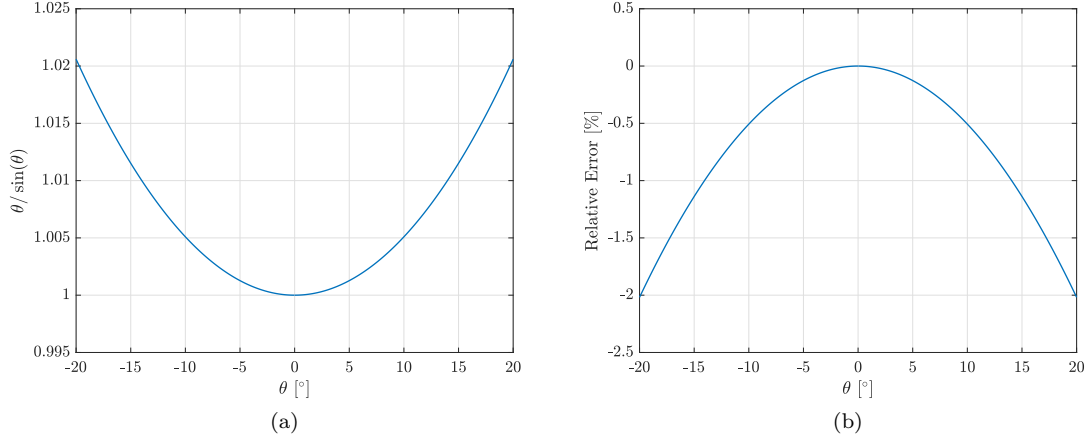


Figure 5.3: Figure (a) shows the true value of $\frac{\theta}{\sin(\theta)}$ as a function of θ . Figure (b) shows the relative error of the approximation as a function of axis-angle θ .

By using (B.6), $\log(\mathbf{R})$ can be approximated by

$$\log(\mathbf{R}) \approx \frac{\mathbf{R} - \mathbf{R}^T}{2}. \quad (\text{B.7})$$

Using (B.7), we can also obtain an approximation for the derivative of the logarithmic mapping of the rotation matrix

$$D \log(\mathbf{R}) \delta \mathbf{R} \approx D \left(\frac{\mathbf{R} - \mathbf{R}^T}{2} \right) \delta \mathbf{R} = \frac{\delta \mathbf{R} - \delta \mathbf{R}^T}{2} = \frac{\mathbf{R} \Delta^{\mathbf{R}^\wedge} - (\Delta^{\mathbf{R}^\wedge})^T \mathbf{R}^T}{2}. \quad (\text{B.8})$$

C Derivation of the spring wrench acting on frame S

This appendix provides the derivation of how we go from (3.23) to an expression in which we have a spring wrench acting on the package at frame S . Therefore, we want to derive an expression for ${}^{S_1} \Delta_{S_2, S_1}$, such that we have a mapping

$$\mathbf{F}: {}^S \Delta_{E, S} \mapsto {}^{S_1} \Delta_{S_2, S_1}. \quad (\text{C.9})$$

Therefore, we have

$${}^{S_2} \mathbf{H}_{S_1} {}^{S_1} \Delta_{S_2, S_1}^\wedge = D {}^{S_2} \mathbf{H}_{S_1} \left({}^E \mathbf{H}_S \right) {}^E \mathbf{H}_S {}^S \Delta_{E, S}^\wedge, \quad (\text{C.10})$$

where ${}^{S_2} \mathbf{H}_{S_1} \left({}^E \mathbf{H}_S \right)$ is as in (3.13). To compute (C.10), we have

$${}^{S_2} \delta \mathbf{H}_{S_1} \left({}^E \mathbf{H}_S \right) = \left[\begin{array}{c|c} {}^E \delta \mathbf{R}_S & {}^E \delta \mathbf{R}_S (l_1 {}^S \mathbf{z}_S) + {}^E \delta \mathbf{o}_S \\ \hline \mathbf{0}_{1 \times 3} & 0 \end{array} \right], \quad (\text{C.11})$$

which we can write as

$${}^{S_2} \delta \mathbf{H}_{S_1} \left({}^E \mathbf{H}_S \right) = \left[\begin{array}{c|c} {}^E \mathbf{R}_S {}^S \Delta_{E, S}^{\mathbf{R}^\wedge} & {}^E \mathbf{R}_S {}^S \Delta_{E, S}^{\mathbf{R}^\wedge} (l_1 {}^S \mathbf{z}_S) + {}^E \mathbf{R}_S {}^S \Delta_{E, S}^{\mathbf{o}} \\ \hline \mathbf{0}_{1 \times 3} & 0 \end{array} \right], \quad (\text{C.12})$$

by using the notation as in Section 2.2.5. Furthermore, we have

$${}^{S_2}\delta\mathbf{H}_{S_1} = \left[\begin{array}{c|c} {}^{S_2}\delta\mathbf{R}_{S_1} & {}^{S_2}\delta\mathbf{o}_{S_1} \\ \mathbf{0}_{1\times 3} & 0 \end{array} \right], \quad (\text{C.13})$$

which we can write as

$${}^{S_2}\delta\mathbf{H}_{S_1} = \left[\begin{array}{c|c} {}^{S_2}\mathbf{R}_{S_1} {}^{S_1}\Delta_{S_2,S_1}^{\mathbf{R}\wedge} & {}^{S_2}\mathbf{R}_{S_1} {}^{S_1}\Delta_{S_2,S_1}^{\mathbf{o}} \\ \mathbf{0}_{1\times 3} & 0 \end{array} \right]. \quad (\text{C.14})$$

Now we use that the perturbation of ${}^{S_2}\mathbf{H}_{S_1}$, (C.12), and the perturbation of ${}^{S_2}\mathbf{H}_{S_1}$ (${}^E\mathbf{H}_S$), (C.14), should be equal such that we have

$$\left[\begin{array}{c|c} {}^E\mathbf{R}_S {}^S\Delta_{E,S}^{\mathbf{R}\wedge} & {}^E\mathbf{R}_S {}^S\Delta_{E,S}^{\mathbf{R}\wedge} (l_1 {}^S\mathbf{z}_S) + {}^E\mathbf{R}_S {}^S\Delta_{E,S}^{\mathbf{o}} \\ \mathbf{0}_{1\times 3} & 0 \end{array} \right] = \left[\begin{array}{c|c} {}^{S_2}\mathbf{R}_{S_1} {}^{S_1}\Delta_{S_2,S_1}^{\mathbf{R}\wedge} & {}^{S_2}\mathbf{R}_{S_1} {}^{S_1}\Delta_{S_2,S_1}^{\mathbf{o}} \\ \mathbf{0}_{1\times 3} & 0 \end{array} \right]. \quad (\text{C.15})$$

First, we consider the rotational parts of (C.15). Because we defined S_1 such that $[S_1] = [S]$ and S_2 such that $[S_2] = [E]$, it holds that ${}^{S_2}\mathbf{R}_{S_1} = {}^E\mathbf{R}_S$. Therefore, it must be that

$${}^{S_1}\Delta_{S_2,S_1}^{\mathbf{R}\wedge} = {}^S\Delta_{E,S}^{\mathbf{R}\wedge}. \quad (\text{C.16})$$

Next, we rewrite the translation term on the left hand side of (C.15) by using ${}^{S_2}\mathbf{R}_{S_1} = {}^E\mathbf{R}_S$ and using the properties of a cross product [62], such that we obtain

$${}^E\mathbf{R}_S {}^S\Delta_{E,S}^{\mathbf{R}\wedge} (l_1 {}^S\mathbf{z}_S) + {}^E\mathbf{R}_S {}^S\Delta_{E,S}^{\mathbf{o}} = {}^{S_2}\mathbf{R}_{S_1} \left(-l_1 {}^S\mathbf{z}_S \wedge {}^S\Delta_{E,S}^{\mathbf{R}} + {}^S\Delta_{E,S}^{\mathbf{o}} \right). \quad (\text{C.17})$$

Substitution of (C.17) in (C.15) gives

$$\left[\begin{array}{c|c} {}^E\mathbf{R}_S {}^S\Delta_{E,S}^{\mathbf{R}\wedge} & {}^{S_2}\mathbf{R}_{S_1} \left(-l_1 {}^S\mathbf{z}_S \wedge {}^S\Delta_{E,S}^{\mathbf{R}} + {}^S\Delta_{E,S}^{\mathbf{o}} \right) \\ \mathbf{0}_{1\times 3} & 0 \end{array} \right] = \left[\begin{array}{c|c} {}^{S_2}\mathbf{R}_{S_1} {}^{S_1}\Delta_{S_2,S_1}^{\mathbf{R}\wedge} & {}^{S_2}\mathbf{R}_{S_1} {}^{S_1}\Delta_{S_2,S_1}^{\mathbf{o}} \\ \mathbf{0}_{1\times 3} & 0 \end{array} \right]. \quad (\text{C.18})$$

Considering that the translation parts of (C.18) should be equal, we get

$${}^{S_1}\Delta_{S_2,S_1}^{\mathbf{o}} = -l_1 {}^S\mathbf{z}_S \wedge {}^S\Delta_{E,S}^{\mathbf{R}} + {}^S\Delta_{E,S}^{\mathbf{o}}. \quad (\text{C.19})$$

Combining (C.16) and (C.19) gives us

$${}^{S_1}\Delta_{S_2,S_1} = \begin{bmatrix} \mathbf{I}_3 & -l_1 {}^S\mathbf{z}_S \wedge \\ \mathbf{0}_{3\times 3} & \mathbf{I}_3 \end{bmatrix} {}^S\Delta_{E,S} \quad (\text{C.20})$$

which corresponds to the desired mapping as in (C.9), such that $\mathbf{F} = {}^{S_1}\mathbf{X}_S$. Substitution of (C.20) into (3.23) results in

$$\begin{aligned} DP_0(\mathbf{H})\mathbf{H}\Delta^\wedge &= s\mathbf{f}_{Pa \rightarrow SC, spring}^T {}^S\Delta_{E,S} \\ &= \frac{1}{4} \begin{bmatrix} (\mathbf{I} + \mathbf{R}^T)\mathbf{o} \\ (\mathbf{R} - \mathbf{R}^T)^\vee \end{bmatrix}^T \mathbf{K} \begin{bmatrix} \mathbf{R} + \mathbf{I} & (\mathbf{R}^T\mathbf{o})^\wedge \\ \mathbf{0}_{3\times 3} & (\text{tr}(\mathbf{R})\mathbf{I}_3 - \mathbf{R}^T) \end{bmatrix} \begin{bmatrix} \mathbf{I}_3 & -l_1 {}^S\mathbf{z}_S \wedge \\ \mathbf{0}_{3\times 3} & \mathbf{I}_3 \end{bmatrix} {}^S\Delta_{E,S}. \end{aligned} \quad (\text{C.21})$$

Having this expression, we can write the spring wrench working on the package as

$$s\mathbf{f}_{SC \rightarrow Pa, spring} = -\frac{1}{4} \begin{bmatrix} \mathbf{I}_3 & \mathbf{0}_{3\times 3} \\ l_1 {}^S\mathbf{z}_S \wedge & \mathbf{I}_3 \end{bmatrix} \begin{bmatrix} \mathbf{R}^T + \mathbf{I}_3 & \mathbf{0}_{3\times 3} \\ -(\mathbf{R}^T\mathbf{o})^\wedge & (\text{tr}(\mathbf{R})\mathbf{I}_3 - \mathbf{R}) \end{bmatrix} \mathbf{K} \begin{bmatrix} (\mathbf{I}_3 + \mathbf{R}^T)\mathbf{o} \\ (\mathbf{R} - \mathbf{R}^T)^\vee \end{bmatrix}, \quad (\text{C.22})$$

which is the same expression as (3.27).

D Coupled translational-angular damping on SE(3)

For the modeling of the damping, we take the Newton-Euler equations of two rigid bodies coupled via velocity-dependent wrenches that exhibit a linear relationship with respect to the velocity as

$${}^1\mathbb{M}_1{}^1\dot{\mathbf{v}}_{0,1} + {}^1\mathbf{v}_{0,1}\bar{\times}^*{}^1\mathbb{M}_1{}^1\mathbf{v}_{0,1} = -{}^1\mathbf{D}_1{}^1\mathbf{v}_{0,1} + {}^1\mathbf{D}_2{}^2\mathbf{v}_{0,2} \quad (\text{D.23})$$

$${}^2\mathbb{M}_2{}^2\dot{\mathbf{v}}_{0,2} + {}^2\mathbf{v}_{0,2}\bar{\times}^*{}^2\mathbb{M}_2{}^2\mathbf{v}_{0,2} = {}^2\mathbf{D}_1{}^1\mathbf{v}_{0,1} - {}^2\mathbf{D}_2{}^2\mathbf{v}_{0,2}. \quad (\text{D.24})$$

In order for the wrenches to provide dissipation at every instant of time, we need to assume that the matrix

$$\begin{bmatrix} {}^1\mathbf{D}_1 & -{}^1\mathbf{D}_2 \\ -{}^2\mathbf{D}_1 & {}^2\mathbf{D}_2 \end{bmatrix} \quad (\text{D.25})$$

is symmetric and positive (semi)definite. Assuming (D.25) to be symmetric implies, in particular, that ${}^2\mathbf{D}_1^T = {}^1\mathbf{D}_2$. The model (D.23)-(D.24) does not describe yet a damper whose wrench depends solely on the relative velocity of one body with respect to the other and that satisfy the action-and-reaction principle of Newtonian mechanics. To this end, we need to impose further conditions on the matrix (D.25).

To find these additional conditions, we rewrite the interaction wrenches (i.e., the right-hand-side of (D.23)-(D.24)) in terms of the relative velocity $\mathbf{v}_{1,2} = -\mathbf{v}_{2,1}$. The additional conditions emerge as necessary conditions to remove any term in the expressions that cannot be written in terms of the relative velocity. Namely, from the known identities

$${}^1\mathbf{v}_{1,2} = {}^1\mathbf{v}_{1,0} + {}^1\mathbf{v}_{0,2}, \quad (\text{D.26})$$

$${}^2\mathbf{v}_{1,2} = {}^2\mathbf{v}_{1,0} + {}^2\mathbf{v}_{0,2}, \quad (\text{D.27})$$

and the right-hand-side of (D.23)-(D.24), we get

$$-{}^1\mathbf{D}_1({}^1\mathbf{v}_{2,1} + {}^1\mathbf{v}_{0,2}) + {}^1\mathbf{D}_2{}^2\mathbf{v}_{0,2} = -{}^1\mathbf{D}_1{}^1\mathbf{v}_{2,1} - {}^1\mathbf{D}_1{}^1\mathbf{v}_{0,2} + {}^1\mathbf{D}_2{}^2\mathbf{v}_{0,2}, \quad (\text{D.28})$$

$${}^2\mathbf{D}_1{}^1\mathbf{v}_{0,1} - {}^2\mathbf{D}_2({}^2\mathbf{v}_{1,2} + {}^2\mathbf{v}_{0,1}) = -{}^2\mathbf{D}_2{}^2\mathbf{v}_{1,2} + {}^2\mathbf{D}_1{}^1\mathbf{v}_{0,1} - {}^2\mathbf{D}_2{}^2\mathbf{v}_{0,1}. \quad (\text{D.29})$$

In order for the expressions above to depend only on the relative velocity, we then need to impose the conditions

$${}^1\mathbf{D}_1 = {}^1\mathbf{D}_2{}^2\mathbf{X}_1, \quad (\text{D.30})$$

$${}^2\mathbf{D}_1{}^1\mathbf{X}_2 = {}^2\mathbf{D}_2. \quad (\text{D.31})$$

Recalling that we also have ${}^2\mathbf{D}_1^T = {}^1\mathbf{D}_2$, we obtain also

$${}^2\mathbf{D}_2{}^2\mathbf{X}_1 = {}^2\mathbf{X}_1{}^1\mathbf{D}_1, \quad (\text{D.32})$$

$${}^2\mathbf{D}_1{}^1\mathbf{X}_2 = {}^2\mathbf{X}_1{}^1\mathbf{D}_2. \quad (\text{D.33})$$

None of the matrices ${}^1\mathbf{D}_1$, ${}^1\mathbf{D}_2$, ${}^2\mathbf{D}_1$, and ${}^2\mathbf{D}_2$ can be taken as constant. It is however possible to write the equations of motion with the additional conditions in the symmetric form

$${}^1\mathbb{M}_1{}^1\dot{\mathbf{v}}_{0,1} + {}^1\mathbf{v}_{0,1}\bar{\times}^*{}^1\mathbb{M}_1{}^1\mathbf{v}_{0,1} = -{}^1\mathbf{D}_1{}^1\mathbf{v}_{2,1} = -{}^1\mathbf{D}_2{}^2\mathbf{v}_{2,1} \quad (\text{D.34})$$

$${}^2\mathbb{M}_2{}^2\dot{\mathbf{v}}_{0,2} + {}^2\mathbf{v}_{0,2}\bar{\times}^*{}^2\mathbb{M}_2{}^2\mathbf{v}_{0,2} = -{}^2\mathbf{D}_2{}^2\mathbf{v}_{1,2} = -{}^2\mathbf{D}_1{}^1\mathbf{v}_{1,2}. \quad (\text{D.35})$$

Note that the wrenches applied to the rigid bodies satisfy action-reaction principle (when expressed with respect to the same frame), i.e., the external wrenches are one the opposite of the other.

We can now take

$${}^1\mathbf{D}_1 := \frac{1}{2}(\mathbf{P} + {}^1\mathbf{X}^2\mathbf{P}^2\mathbf{X}_1), \quad (\text{D.36})$$

or equivalently

$${}^2\mathbf{D}_2 := \frac{1}{2}(\mathbf{P} + {}^2\mathbf{X}^1 \mathbf{P}^1 \mathbf{X}_2), \quad (\text{D.37})$$

with $\mathbf{P} = \mathbf{P}^T \geq 0$, obtaining also the mixed damping coefficient

$${}^1\mathbf{D}_2 = \frac{1}{2}(\mathbf{P}^1 \mathbf{X}_2 + {}^1\mathbf{X}^2 \mathbf{P}), \quad (\text{D.38})$$

$${}^2\mathbf{D}_1 = \frac{1}{2}(\mathbf{P}^2 \mathbf{X}_1 + {}^2\mathbf{X}^1 \mathbf{P}), \quad (\text{D.39})$$

which shows how the damping model can be parametrized by a constant positive definite matrix \mathbf{P} . The way of writing each damping matrix part of \mathbf{D} as a small alteration of a matrix \mathbf{P} is basically the same trick as done by Fasse and Breedveld in [26], where they used this trick to make their compliance function port-indifferent.

D.1 Passivity of the damping wrench

The power injected by the relative-velocity-dependent damping model is

$$-\langle {}^1\mathbf{D}_2 {}^2\mathbf{v}_{2,1}, {}^1\mathbf{v}_{0,1} \rangle - \langle {}^2\mathbf{D}_1 {}^1\mathbf{v}_{1,2}, {}^2\mathbf{v}_{0,2} \rangle. \quad (\text{D.40})$$

Such an expression can be equivalently rewritten in frame 2 coordinates as

$$-\langle {}^2\mathbf{X}^1 {}^1\mathbf{D}_2 {}^2\mathbf{v}_{2,1}, {}^2\mathbf{v}_{0,1} \rangle - \langle {}^2\mathbf{D}_1 {}^1\mathbf{X}_2 {}^2\mathbf{v}_{1,2}, {}^2\mathbf{v}_{0,2} \rangle, \quad (\text{D.41})$$

and then, by virtue of (D.33), as

$$-\langle {}^2\mathbf{D}_2 {}^2\mathbf{v}_{1,2}, {}^2\mathbf{v}_{1,2} \rangle. \quad (\text{D.42})$$

Such an expression, which in frame 1 coordinates equivalently reads

$$-\langle {}^1\mathbf{D}_1 {}^1\mathbf{v}_{1,2}, {}^1\mathbf{v}_{1,2} \rangle, \quad (\text{D.43})$$

is always negative as long as (D.37) (equivalently, (D.36)) is positive (semi-)definite, which is trivially true for $\mathbf{P} \geq 0$.

E Velocity transformation

To express ${}^{S_1}\mathbf{v}_{S_2, S_1}$ in terms of ${}^S\mathbf{v}_{E, S}$ one needs to remember that

$${}^E\mathbf{H}_S = {}^E\mathbf{H}_{S_2} {}^{S_2}\mathbf{H}_{S_1} {}^{S_1}\mathbf{H}_S, \quad (\text{E.44})$$

and know its time derivative

$${}^E\dot{\mathbf{H}}_S = {}^E\mathbf{H}_{S_2} {}^{S_2}\dot{\mathbf{H}}_{S_1} {}^{S_1}\mathbf{H}_S. \quad (\text{E.45})$$

Using (E.44) and (E.45), the left trivialized velocity can be obtained by

$$\begin{aligned}
 {}^S\mathbf{v}_{E,S}^\wedge &= {}^E\mathbf{H}_S^{-1E}\dot{\mathbf{H}}_S \\
 &= {}^S\mathbf{H}_{S_1}{}^{S_1}\mathbf{H}_{S_2}{}^{S_2}\mathbf{H}_E{}^E\mathbf{H}_{S_2}{}^{S_2}\dot{\mathbf{H}}_{S_1}{}^{S_1}\mathbf{H}_S \\
 &= {}^S\mathbf{H}_{S_1}{}^{S_1}\mathbf{v}_{S_2,S_1}^\wedge{}^{S_1}\mathbf{H}_S \\
 &= \left({}^S\mathbf{X}_{S_1}{}^{S_1}\mathbf{v}_{S_2,S_1} \right)^\wedge.
 \end{aligned} \tag{E.47}$$

From this last expression, (E.47), it can be seen that

$${}^{S_1}\mathbf{v}_{S_2,S_1} = {}^S\mathbf{X}_{S_1}^{-1S}\mathbf{v}_{E,S} = {}^{S_1}\mathbf{X}_S{}^S\mathbf{v}_{E,S}. \tag{E.48}$$

F Central difference method

One way of calculating body velocities and accelerations from $\text{SO}(3) \times \mathbb{R}^3$ data is by using a finite difference method. The three basic types are: backward, forward, and central finite difference [63]. In this project has been made use of the central-difference method as this one is of higher accuracy (second-order) compared to forward and backward finite difference (first-order). The central-difference method on $\text{SO}(3) \times \mathbb{R}^3$ data is illustrated for the package pose with respect to the absolute frame. Of course, the same procedure can be executed for pose data of different frames.

The right trivialized angular velocity is computed by applying the central-difference method on the Lie algebra of the orientation data, $\mathfrak{so}(3)$, such that

$${}^A\bar{\omega}_{A,B}(t_k) = \frac{1}{t_{k+1} - t_{k-1}} \left(\log \left(\mathbf{R}(t_{k+1})\mathbf{R}^T(t_k) \right) - \log \left(\mathbf{R}(t_{k-1})\mathbf{R}^T(t_k) \right) \right)^\vee, \tag{F.49}$$

where $\mathbf{R} = {}^A\mathbf{R}_B$, t_k is the time instant, t_{k+1} is the next instant of time, and t_{k-1} is the previous instant of time. The bar in ${}^A\bar{\omega}_{A,B}$ indicates ‘estimated via the central-difference method’. Now we can calculate the left trivialized angular velocity by

$${}^B\bar{\omega}_{A,B}(t_k) = \mathbf{R}^T{}^A\bar{\omega}_{A,B}(t_k). \tag{F.50}$$

Having this, we can use the central-difference method to calculate the left trivialized angular acceleration

$${}^B\bar{\ddot{\omega}}_{A,B}(t_k) = \frac{1}{t_{k+1} - t_{k-1}} \left({}^B\bar{\omega}_{A,B}(t_{k+1}) - {}^B\bar{\omega}_{A,B}(t_{k-1}) \right). \tag{F.51}$$

For the position data, we can simply do

$$\bar{\mathbf{o}} = \frac{1}{t_{k+1} - t_{k-1}} \left(\mathbf{o}(k+1) - \mathbf{o}(k-1) \right), \tag{F.52}$$

where $\mathbf{o} = {}^A\mathbf{o}_B$ and $\bar{\mathbf{o}} = {}^A\bar{\mathbf{o}}_B$. Subsequently, the left trivialized linear velocity can be obtained by

$${}^B\bar{\mathbf{v}}_{A,B}(t_k) = \mathbf{R}^T\bar{\mathbf{o}}(t_k) \tag{F.53}$$

Similar to the angular acceleration, F.51, the left trivialized linear acceleration is obtained by

$${}^B\bar{\ddot{\mathbf{v}}}_{A,B}(t_k) = \frac{1}{t_{k+1} - t_{k-1}} \left({}^B\bar{\mathbf{v}}_{A,B}(t_{k+1}) - {}^B\bar{\mathbf{v}}_{A,B}(t_{k-1}) \right). \tag{F.54}$$

The last step, to have a complete description of the body velocity and acceleration is obtaining the right trivialized velocity and acceleration. These are obtained by

$${}^A\bar{\mathbf{v}}_{A,B}(t_k) = {}^A\mathbf{X}_B {}^B\bar{\mathbf{v}}_{A,B}(t_k) = {}^A\mathbf{X}_B \begin{bmatrix} {}^B\bar{\mathbf{v}}_{A,B}(t_k) \\ {}^B\bar{\boldsymbol{\omega}}_{A,B}(t_k) \end{bmatrix}, \quad (\text{F.55})$$

$${}^A\bar{\mathbf{v}}_{A,B}(t_k) = {}^A\mathbf{X}_B {}^B\bar{\mathbf{v}}_{A,B}(t_k) = {}^A\mathbf{X}_B \begin{bmatrix} {}^B\bar{\mathbf{v}}_{A,B}(t_k) \\ {}^B\bar{\boldsymbol{\omega}}_{A,B}(t_k) \end{bmatrix}. \quad (\text{F.56})$$

G Definition exponential mapping on SO(3) and its derivatives

The estimated rotation matrix and its time derivatives can be obtained by

$$\widehat{\mathbf{R}}(t_k) = \exp(\boldsymbol{\eta}_0)\mathbf{R}(t_k), \quad (\text{G.57})$$

$$\widehat{\dot{\mathbf{R}}}(t_k) = (D \exp(\boldsymbol{\eta}_0) \cdot \boldsymbol{\eta}_1)\mathbf{R}(t_k) \quad (\text{G.58})$$

$$= (d \exp(\boldsymbol{\eta}_0) \cdot \boldsymbol{\eta}_1) \exp(\boldsymbol{\eta}_0)\mathbf{R}(t_k) \quad (\text{G.59})$$

$$= \widehat{\boldsymbol{\omega}}(t_k)\widehat{\mathbf{R}}(t_k), \quad (\text{G.60})$$

$$\widehat{\frac{D\dot{\mathbf{R}}}{dt}}(t_k) = \left(\mathbb{D}^{2(+)} \exp(\boldsymbol{\eta}_0) \cdot (\boldsymbol{\eta}_1, \boldsymbol{\eta}_1) + D \exp(\boldsymbol{\eta}_0) \cdot \boldsymbol{\eta}_2 \right) \mathbf{R}(t_k) \quad (\text{G.61})$$

$$= \left(\mathfrak{d}^{2(+)} \exp(\boldsymbol{\eta}_0) \cdot (\boldsymbol{\eta}_1, \boldsymbol{\eta}_1) + d \exp(\boldsymbol{\eta}_0) \cdot \boldsymbol{\eta}_2 \right) \exp(\boldsymbol{\eta}_0)\mathbf{R}(t_k) \quad (\text{G.62})$$

$$= \widehat{\boldsymbol{\omega}}(t_k)\widehat{\mathbf{R}}(t_k). \quad (\text{G.63})$$

The step from (G.58) to (G.59) is given by the fact that we can write

$$D \exp(\boldsymbol{\eta}_0) \cdot \boldsymbol{\eta}_1 = (d \exp(\boldsymbol{\eta}_0) \cdot \boldsymbol{\eta}_1) \exp(\boldsymbol{\eta}_0), \quad (\text{G.64})$$

where $d \exp$ is the right trivialized tangent of the exponential mapping which is explicitly given as

$$d \exp(\boldsymbol{\eta}) = \mathbf{I}_3 + \frac{1}{2}\beta(\boldsymbol{\eta})\boldsymbol{\eta}^\wedge + \frac{1}{\|\boldsymbol{\eta}\|}(1 - \alpha(\boldsymbol{\eta}))(\boldsymbol{\eta}^\wedge)^2, \quad (\text{G.65})$$

as in [64]. Furthermore, $\mathfrak{d}^{2(+)} \exp$ is the right trivialized geometric Hessian of the exponential mapping with respect to the (+) Cartan-Schouten connection. The step from (G.61) to (G.62) is given by the fact that we can write

$$\begin{aligned} \mathbb{D}^{2(+)} \exp(\boldsymbol{\xi}) \cdot (\boldsymbol{\eta}_1, \boldsymbol{\eta}_2) &= \\ \lim_{\epsilon \rightarrow 0} \frac{(D \exp(\boldsymbol{\xi} + \epsilon \boldsymbol{\eta}_2) \cdot \boldsymbol{\eta}_1) \exp^{-1}(\boldsymbol{\xi} + \epsilon \boldsymbol{\eta}_2) \exp(\boldsymbol{\xi}) - D \exp(\boldsymbol{\xi}) \cdot \boldsymbol{\eta}_1}{\epsilon} & \quad (\text{G.66}) \end{aligned}$$

where

$$D \exp(\boldsymbol{\xi} + \epsilon \boldsymbol{\eta}_2) \cdot \boldsymbol{\eta}_1 = (d \exp(\boldsymbol{\xi} + \epsilon \boldsymbol{\eta}_2) \boldsymbol{\eta}_1)^\wedge \exp(\boldsymbol{\xi} + \epsilon \boldsymbol{\eta}_2) \quad (\text{G.67})$$

such that

$$\mathbb{D}^{2(+)} \exp(\boldsymbol{\xi}) \cdot (\boldsymbol{\eta}_1, \boldsymbol{\eta}_2) \quad (\text{G.68})$$

$$= \lim_{\epsilon \rightarrow 0} \frac{1}{\epsilon} \left[(d \exp(\boldsymbol{\xi} + \epsilon \boldsymbol{\eta}_2) \boldsymbol{\eta}_1)^\wedge \exp(\boldsymbol{\xi}) - (d \exp(\boldsymbol{\xi}) \boldsymbol{\eta}_1)^\wedge \exp(\boldsymbol{\xi}) \right] \quad (\text{G.69})$$

$$= \left[\left\{ \lim_{\epsilon \rightarrow 0} \frac{1}{\epsilon} (d \exp(\boldsymbol{\xi} + \epsilon \boldsymbol{\eta}_2) - d \exp(\boldsymbol{\xi})) \right\} \boldsymbol{\eta}_1 \right]^\wedge \exp(\boldsymbol{\xi}) \quad (\text{G.70})$$

$$= \left[(D d \exp(\boldsymbol{\xi}) \boldsymbol{\eta}_2) \boldsymbol{\eta}_1 \right]^\wedge \exp(\boldsymbol{\xi}) \quad (\text{G.71})$$

$$= \left[\mathfrak{d}^{2(+)} \exp(\boldsymbol{\xi}) \cdot (\boldsymbol{\eta}_1, \boldsymbol{\eta}_2) \right]^\wedge \exp(\boldsymbol{\xi}), \quad (\text{G.72})$$

where the expressions for $d^{2(+)} \exp(\boldsymbol{\xi}) \cdot (\boldsymbol{\eta}_1, \boldsymbol{\eta}_2)$ and $\exp(\boldsymbol{\xi})$ are explicitly given as

$$\begin{aligned} & d^{2(+)} \exp(\boldsymbol{\xi}) \cdot (\boldsymbol{\eta}_1, \boldsymbol{\eta}_2) \\ &= \left(\frac{1}{2} \beta(\boldsymbol{\xi}) \boldsymbol{\eta}_2^\wedge + \frac{1 - \alpha(\boldsymbol{\xi})}{\|\boldsymbol{\xi}\|} (\boldsymbol{\eta}_2^\wedge \boldsymbol{\xi}^\wedge + \boldsymbol{\xi}^\wedge \boldsymbol{\eta}_2^\wedge) + \frac{\alpha(\boldsymbol{\xi}) - \beta(\boldsymbol{\xi})}{\|\boldsymbol{\xi}\|} (\boldsymbol{\xi}^T \boldsymbol{\eta}_2) \boldsymbol{\xi}^\wedge + \right. \\ & \left. \frac{1}{\|\boldsymbol{\xi}\|} \left(\frac{1}{2} \beta(\boldsymbol{\xi}) - \frac{3}{\|\boldsymbol{\xi}\|} (1 - \alpha(\boldsymbol{\xi})) \right) (\boldsymbol{\xi}^T \boldsymbol{\eta}_2) (\boldsymbol{\xi}^\wedge)^2 \right) \cdot \boldsymbol{\eta}_1 \end{aligned} \quad (\text{G.73})$$

and

$$\exp(\boldsymbol{\xi}) = \mathbf{I}_3 + \alpha(\boldsymbol{\xi}) \boldsymbol{\xi}^\wedge + \frac{1}{2} \beta(\boldsymbol{\xi}) (\boldsymbol{\xi}^\wedge)^2 \in \text{SO}(3). \quad (\text{G.74})$$

As obtained from [64], where, for $\boldsymbol{\xi}, \boldsymbol{\eta}_1, \boldsymbol{\eta}_2 \in \mathbb{R}^3$, we used

$$\alpha(\boldsymbol{\eta}) = \frac{\sin(\|\boldsymbol{\eta}\|)}{\|\boldsymbol{\eta}\|}, \quad (\text{G.75})$$

$$\beta(\boldsymbol{\eta}) = \frac{\sin^2(\|\boldsymbol{\eta}\|/2)}{(\|\boldsymbol{\eta}\|/2)^2}. \quad (\text{G.76})$$

Regarding (G.75) and (G.76), we have

$$\lim_{\|\boldsymbol{\eta}\| \rightarrow \mathbf{0}_{3 \times 1}} \alpha(\boldsymbol{\eta}) = 1, \quad (\text{G.77})$$

$$\lim_{\|\boldsymbol{\eta}\| \rightarrow \mathbf{0}_{3 \times 1}} \beta(\boldsymbol{\eta}) = 1, \quad (\text{G.78})$$

and therefore have that

$$\lim_{\|\boldsymbol{\eta}\| \rightarrow \mathbf{0}_{3 \times 1}} \exp(\boldsymbol{\eta}) = \mathbf{I}_3, \quad (\text{G.79})$$

$$\lim_{\|\boldsymbol{\eta}\| \rightarrow \mathbf{0}_{3 \times 1}} d \exp(\boldsymbol{\eta}) = \mathbf{I}_3, \quad (\text{G.80})$$

$$\lim_{\|\boldsymbol{\eta}\| \rightarrow \mathbf{0}_{3 \times 1}} d^{2(+)} \exp(\boldsymbol{\eta}) \cdot (\boldsymbol{\eta}_1, \boldsymbol{\eta}_2) = \frac{1}{2} \boldsymbol{\eta}_2^\wedge. \quad (\text{G.81})$$

H Exclusion of outliers in motion capture data

To obtain accurate results from the parameter identification, a data set without outliers is needed. The outliers in the motion capture data are the result of tracking problems when using the OptiTrack system. One of the problems could be that not enough markers are visible for the OptiTrack cameras. For clarity, the outliers in the OptiTrack data are something different than the measurement noise. The measurement noise is dealt with by using the Savitzky-Golay filter, however, these outliers are that large that these could influence the stiffness and damping identification. Examples of such outliers are shown in Figure 5.4. In here, the unfiltered data of the suction cup with respect to the tooling arm is shown, ${}^E \mathbf{H}_S$. This data includes outliers that are the result of tracking problems of as well the tooling arm as the suction cup (which is tracked by using the plastic plate). The red boxes indicate certain peaks in the data that are outliers.

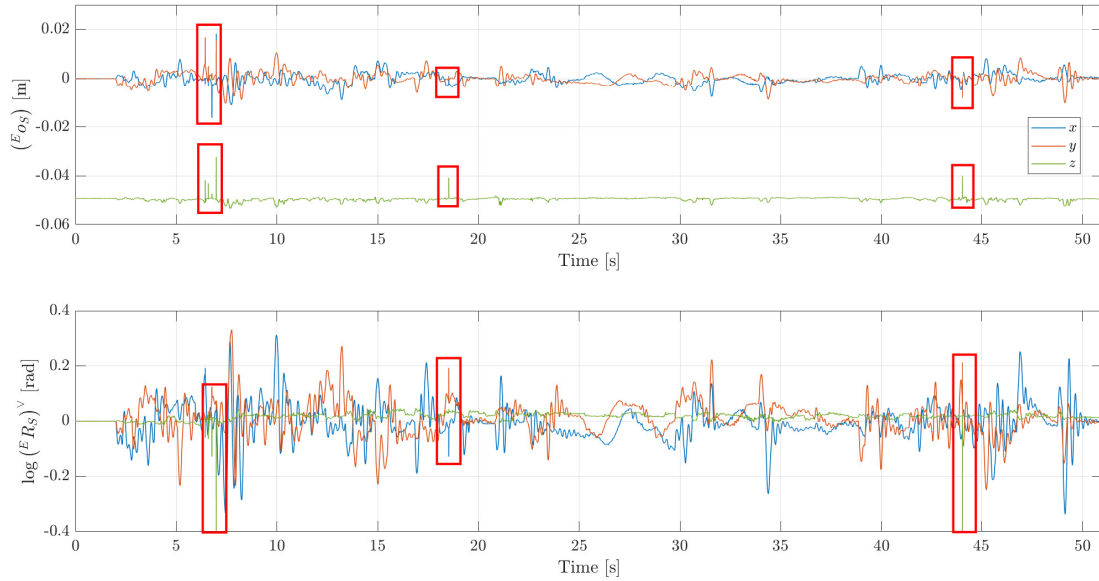


Figure 5.4: Unfiltered pose data of the suction cup lip with respect to the tip of the tooling arm. The red boxes indicate the outliers.

To remove the data which is influenced by these outliers, the raw data from the Comma Separated Value files, as exported by Motive, is inspected. First, it is checked if the number of tracked markers is more or equal to the minimum marker count. The minimal marker count is a setting in Motive which defines the number of markers that need to be visible, for two or more OptiTrack cameras, to reconstruct the pose of a (in Motive define) rigid body. The checking of the minimum

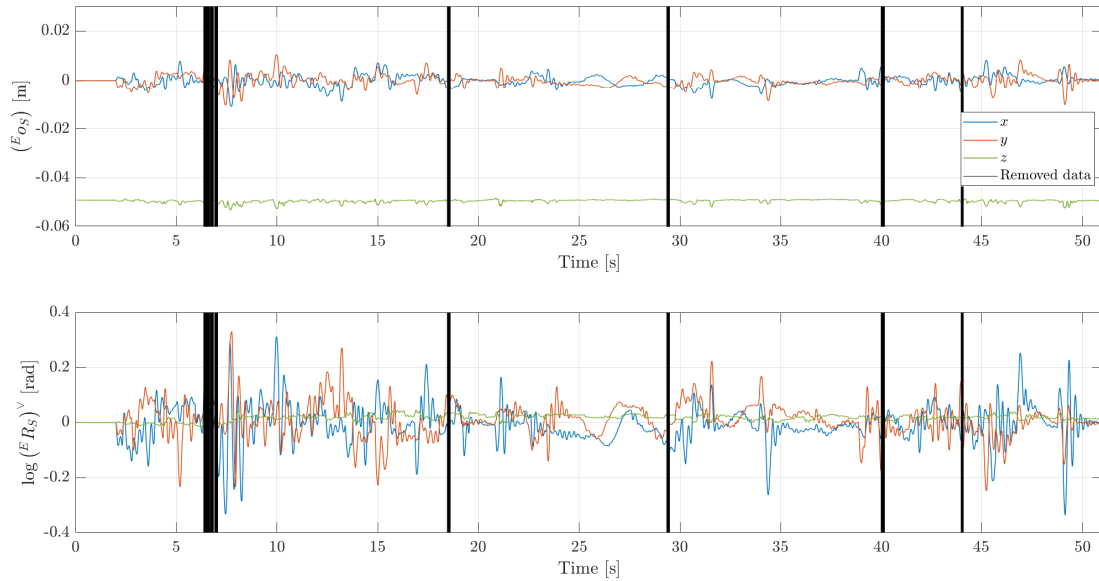


Figure 5.5: Visualization of the pose data ${}^E\mathbf{H}_S$. The black lines indicate the removed data.

marker count is done as well for the tooling arm data as for the plastic plate data. If the minimum marker count for one of the bodies, as defined in Motive, is not achieved at a certain time instant, then this time instant will be labeled as an outlier. A marker is considered as not visible if the marker quality (in the Comma Separated Value file: MQ_RGB) is less than 0.99. A value of 1 means that the marker is tracked properly.

As a second check, to make sure that every outlier is detected, the position and orientation data; PX, PY, PZ and RX, RY, and RZ from the Comma Separated Value file, are also checked. If there is a relatively large jump in this data, the corresponding time instant will also be labeled as an outlier. This is also done for both bodies: the tooling arm and the plastic plate. Note that this identification of the outliers is done when importing the data in MATLAB. The removal of the outliers is carried out after the Savitzky-Golay filtering and before the least-squares fitting of the stiffness and damping matrices. Because the Savitzky-Golay filter fits polynomials to the data within a window, also the filtered data at the time instants near the marked outliers will be influenced by the outliers themselves. Therefore, for every labeled outlier at time instant t_k , the Savitzky-Golay smoothed data ($\widehat{\mathbf{H}}$, $\widehat{\mathbf{v}}$, and $\widehat{\dot{\mathbf{v}}}$) within the time range $[t_{k-n_w} \ t_{k+n_w}]$ will be removed from the data set. This results in Savitzky-Golay smoothed data which is free from outliers. \widetilde{N} will be used to indicate the number of data points left for the parameter identification after the removal of the outliers. Figure 5.5 shows the filtered pose data of the suction cup lip with respect to the tip of the tooling arm, for which the outliers are removed. The black lines indicate the removed data.

I Weighting matrices for least-squares parameter identification

In this appendix, the weighting matrices that are used for the weighted least-squares procedure (performed to identify the stiffness and damping) are presented. The used weighting matrices are:

$$\mathbf{W}_{id,full} = \begin{bmatrix} 0.1702 & 0.01765 & 0.009356 & -0.3622 & 2.685 & 0.6043 \\ 0.01765 & 0.1525 & 0.003543 & -2.201 & 0.3737 & 0.1634 \\ 0.009356 & 0.003543 & 0.1262 & 0.01556 & 0.003813 & -0.5061 \\ -0.3622 & -2.201 & 0.01556 & 45.76 & -8.539 & -2.986 \\ 2.685 & 0.3737 & 0.003813 & -8.539 & 58.09 & 1.630 \\ 0.6043 & 0.1634 & -0.5061 & -2.986 & 1.63 & 157.7 \end{bmatrix}, \quad (\text{I.82})$$

$$\mathbf{W}_{id,diag} = \begin{bmatrix} 0.04475 & 0 & 0 & 0 & 0 & 0 \\ 0 & 0.04475 & 0 & 0 & 0 & 0 \\ 0 & 0 & 0.1216 & 0 & 0 & 0 \\ 0 & 0 & 0 & 14.15 & 0 & 0 \\ 0 & 0 & 0 & 0 & 14.15 & 0 \\ 0 & 0 & 0 & 0 & 0 & 148.4 \end{bmatrix}, \quad (\text{I.83})$$

$$\mathbf{W}_{val,diag} = \begin{bmatrix} 0.04849 & 0 & 0 & 0 & 0 & 0 \\ 0 & 0.04849 & 0 & 0 & 0 & 0 \\ 0 & 0 & 0.1199 & 0 & 0 & 0 \\ 0 & 0 & 0 & 16.23 & 0 & 0 \\ 0 & 0 & 0 & 0 & 16.23 & 0 \\ 0 & 0 & 0 & 0 & 0 & 84.23 \end{bmatrix}. \quad (\text{I.84})$$

Weighting matrix (I.82) is used to fit a full stiffness matrix and a full damping matrix from the identification measurement set. Weighting matrix (I.83) is used to fit a diagonal stiffness matrix and a diagonal damping matrix from the identification measurement set. The last weighting matrix, (I.84), is used to fit a diagonal stiffness matrix and a diagonal damping matrix from the validation measurement set.

J Rewriting package body-fixed velocity and acceleration

By using the relations

$${}^B\mathbf{v}_{E,B} = {}^B\mathbf{X}_S {}^S\mathbf{v}_{E,S}, \quad (\text{J.85})$$

$${}^B\dot{\mathbf{v}}_{E,B} = {}^B\mathbf{X}_S {}^S\dot{\mathbf{v}}_{E,S}, \quad (\text{J.86})$$

we can rewrite the package body-fixed velocity and acceleration as:

$$\begin{aligned} {}^B\mathbf{v}_{A,B} &= {}^B\mathbf{X}_E \left({}^E\mathbf{v}_{A,E} + {}^E\mathbf{v}_{E,B} \right) \\ &= {}^B\mathbf{X}_E \left({}^E\mathbf{v}_{A,E} + {}^E\mathbf{X}_B {}^B\mathbf{v}_{E,B} \right) \\ &= {}^B\mathbf{X}_E \left({}^E\mathbf{v}_{A,E} + {}^E\mathbf{X}_B {}^B\mathbf{X}_S {}^S\mathbf{v}_{E,S} \right) \\ &= {}^B\mathbf{X}_S {}^S\mathbf{X}_E {}^E\mathbf{v}_{A,E} + {}^B\mathbf{X}_S {}^S\mathbf{v}_{E,S}, \end{aligned} \quad (\text{J.87})$$

and

$$\begin{aligned} {}^B\dot{\mathbf{v}}_{A,B} &= {}^B\mathbf{X}_E {}^E\dot{\mathbf{v}}_{A,B} - {}^B\mathbf{v}_{E,B} \times {}^B\mathbf{v}_{A,B} \\ &= {}^B\mathbf{X}_E \left({}^E\dot{\mathbf{v}}_{A,E} + {}^E\dot{\mathbf{v}}_{E,B} \right) - {}^B\mathbf{X}_S {}^S\mathbf{v}_{E,S} \times {}^B\mathbf{v}_{A,B} \\ &= {}^B\mathbf{X}_E \left({}^E\dot{\mathbf{v}}_{A,E} + {}^E\mathbf{X}_B {}^B\dot{\mathbf{v}}_{E,B} \right) - {}^B\mathbf{X}_S {}^S\mathbf{v}_{E,S} \times {}^B\mathbf{v}_{A,B} \\ &= {}^B\mathbf{X}_E {}^E\dot{\mathbf{v}}_{A,E} + {}^B\mathbf{X}_S {}^S\dot{\mathbf{v}}_{E,S} - {}^B\mathbf{X}_S {}^S\mathbf{v}_{E,S} \times {}^B\mathbf{v}_{A,B}. \end{aligned} \quad (\text{J.88})$$

Substitution of (J.87) and (J.88) into our model, (3.5), would mean that we need to estimate ${}^S\mathbf{v}_{E,S}$, ${}^S\dot{\mathbf{v}}_{E,S}$, ${}^E\mathbf{v}_{A,E}$, and ${}^E\dot{\mathbf{v}}_{A,E}$ for the parameter identification. This can be done by applying the Savitzky-Golay filtering on ${}^A\mathbf{H}_E$ and ${}^E\mathbf{H}_S$ measurement data, instead of ${}^A\mathbf{H}_E$ and ${}^A\mathbf{H}_B$ measurement data. This could possibly give more accurate estimations of the velocity and acceleration of the bellows suction cup lip with respect to the tool-arm.

The derivation of (J.85) and (J.86) is as follows. To express ${}^B\mathbf{v}_{E,B}$ in terms of ${}^S\mathbf{v}_{E,S}$ one needs to remember that

$${}^E\mathbf{H}_B = {}^E\mathbf{H}_S {}^S\mathbf{H}_B, \quad (\text{J.89})$$

and the time derivative

$${}^E\dot{\mathbf{H}}_B = {}^E\dot{\mathbf{H}}_S {}^S\mathbf{H}_B. \quad (\text{J.90})$$

Using these, the left trivialized velocity can be obtained by

$$\begin{aligned} {}^B\mathbf{v}_{E,B}^\wedge &= {}^E\mathbf{H}_B^{-1} {}^E\dot{\mathbf{H}}_B \\ &= {}^B\mathbf{H}_S {}^S\mathbf{H}_E {}^E\dot{\mathbf{H}}_S {}^S\mathbf{H}_B \\ &= {}^B\mathbf{H}_S {}^S\mathbf{v}_{E,S}^\wedge {}^S\mathbf{H}_B \\ &= \left({}^B\mathbf{X}_S {}^S\mathbf{v}_{E,S} \right)^\wedge. \end{aligned} \quad (\text{J.91})$$

Rewriting (J.91) gives us

$${}^B\mathbf{v}_{E,B} = {}^B\mathbf{X}_S {}^S\mathbf{v}_{E,S}. \quad (\text{J.92})$$

Taking the time derivative of (J.86) gives the relation

$${}^B\dot{\mathbf{v}}_{E,B} = {}^B\mathbf{X}_S {}^S\dot{\mathbf{v}}_{E,S}. \quad (\text{J.93})$$

Declaration concerning the TU/e Code of Scientific Conduct for the Master's thesis

I have read the TU/e Code of Scientific Conduct¹.

I hereby declare that my Master's thesis has been carried out in accordance with the rules of the TU/e Code of Scientific Conduct

Date

26-08-2021

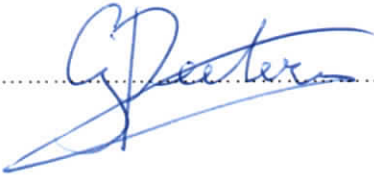
Name

Giel J. H. Peeters

ID-number

0952732

Signature



Submit the signed declaration to the student administration of your department.

¹ See: <http://www.tue.nl/en/university/about-the-university/integrity/scientific-integrity/>
The Netherlands Code of Conduct for Academic Practice of the VSNU can be found here also.
More information about scientific integrity is published on the websites of TU/e and VSNU